

**UNCLASSIFIED**

---

---

**AD 268 366**

*Reproduced  
by the*

**ARMED SERVICES TECHNICAL INFORMATION AGENCY  
ARLINGTON HALL STATION  
ARLINGTON 12, VIRGINIA**



---

---

**UNCLASSIFIED**

NOTICE: When government or other drawings, specifications or other data are used for any purpose other than in connection with a definitely related government procurement operation, the U. S. Government thereby incurs no responsibility, nor any obligation whatsoever; and the fact that the Government may have formulated, furnished, or in any way supplied the said drawings, specifications, or other data is not to be regarded by implication or otherwise as in any manner licensing the holder or any other person or corporation, or conveying any rights or permission to manufacture, use or sell any patented invention that may in any way be related thereto.

**CARNEGIE INSTITUTE OF TECHNOLOGY**

**DEPARTMENT OF PHYSICS**

**PITTSBURGH 13, PENNSYLVANIA**

**FUNDAMENTALS OF SHAPED CHARGES**

**CONTRACT SUPERVISOR**

**EMERSON M. PUGH**

**TWENTY-FOURTH QUARTERLY PROGRESS REPORT**

**COPY No. 49**

**DEPARTMENT OF ARMY PROJECT No. 5B03-04-009**

**ORDNANCE RAD PROJECT No. TB3-OI34**

**CONTRACT NO. DA-36-061-ORD-513**

62-1-5  
XEROX

OCTOBER 31, 1961

October 31, 1961  
Twenty-fourth Quarterly Progress Report  
Contract No. DA-36-061-ORD-513  
Supervisor: Emerson M. Pugh

TABLE OF CONTENTS

	Page
Chapter I - Projector Studies .....	2
Chapter II - Spacial Distribution of Fragments .....	14
Behind Thin Targets	
Chapter III - The Perforation of Thin Plates by .....	63
High Velocity Fragments	
Chapter IV - Oblique Impact Cratering in Lead .....	89
at 3.8 km/sec .	

ABSTRACT CARDS

Advance release  
This information  
is tentative and  
subject to revision

October 31, 1961  
Twenty-fourth Quarterly Progress Report  
Contract No. DA-36-061-ORD-513  
Supervisor: Emerson M. Pugh

Abstract

Various aspects of the perforation of thin targets by high speed fragments have been investigated. A fragment projector yielding compact steel fragments having a velocity of 3.17 km/sec and a mass of .0234 gm was generally used for experimental studies. The design features of this projector along with methods of attaining higher velocities are discussed in Chapter I. The spatial distribution and total mass of the ejecta produced in the perforation of thin targets for both normal and oblique impact are discussed in Chapter II. A simple physical model useful in predicting the velocity of a fragment after having perforated a thin target is discussed in Chapter III along with the dimensional features of the perforations. In Chapter IV the volume and shape of craters produced in lead at  $60^{\circ}$  obliquity by fragments having a velocity of 4 km/sec are compared with the characteristics of craters produced at impact velocities of 3 km/sec and 5 km/sec.

Chapter I - Projector Studies  
- R Vitali

Introduction

In order to facilitate controlled experiments in terminal hyperballistics, two high explosive fragment projectors have been developed. Nominally they yield velocities of 3 km/sec and 4 km/sec. The projectiles at impact have unit aspect ratio and an impact mass of approximately 0.025 grams. The particulars of the charge and charge performance will be discussed in this chapter.

Experimental Procedure

Time of flight measurements were made with a model 7270 Beckman-Berkeley time interval meter. Time measurements were observed to a tenth of a microsecond. The chronograph was initiated with a twisted pair of No. 26 nyclad wire located at the base of the charge. The stop grid consisted of alternate layers of lead foil and paper. A Flexitron flash X-ray system, Type PS-300-1000-0.2 was also employed to measure time of flights, and to observe the projectiles in flight. Instantaneous velocities were then determined from the distance-time data.

Mild steel plates were used as witness targets in order to determine whether or not the projectile remained intact throughout its flight. After each firing these plates were examined for

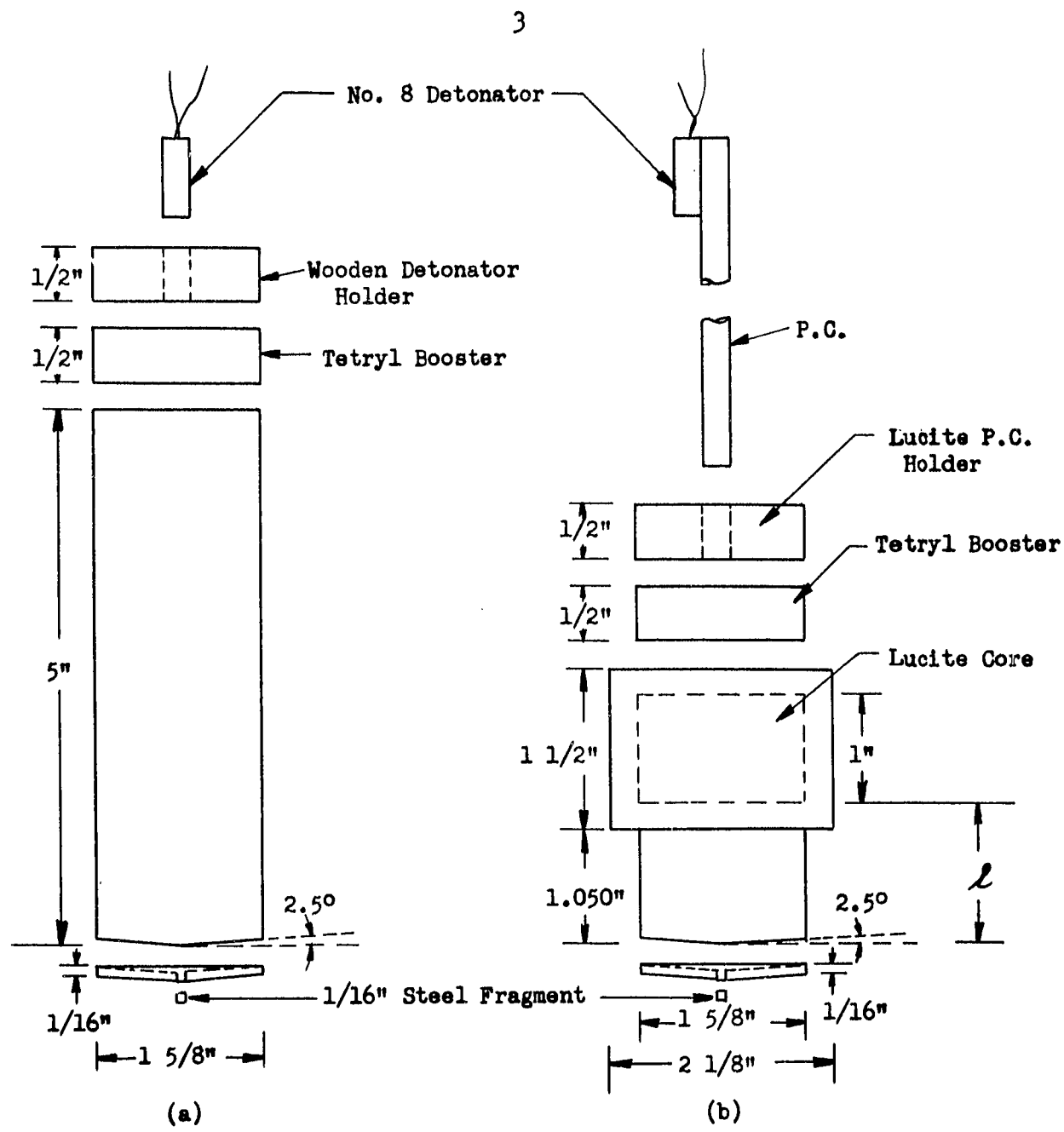


**Fig. I-1** Sketches illustrating the details of two projector designs: (a) 3 km/sec projector; (b) 4 km/sec projector.

extraneous craters or for any unusual crater characteristics. If anything but a single uniform crater was observed, the shot was not used for velocity measurements. A determination of mass lost by the projectiles was obtained by firing them into celotex or styro-foam targets; they were recovered intact from these targets and mass measurements were made with an analytical balance and recorded to 0.0001 grams.

#### 3 km/sec Projector

The geometrical aspects of the nominal 3 km/sec projector are shown in Fig. 1-1(a). It is a right circular cylinder of Comp. B (60RDX/40TNT), 1-5/8 in. in diameter by 5 in. in length. The explosive has been cast onto a steel surround enveloping a 1/16 in. x 1/16 in. cylindrical steel fragment. The charge is initiated with a No. 8 electric detonator in conjunction with a 1-5/8 in. x 1/2 in. tetryl booster.

The projector was originally designed utilizing a flat woods metal surround; this design was inadequate because the woods metal would not disperse and was causing excessive target damage in the vicinity of the crater. At this point the woods metal surround was made conical in shape in the hope that a component of velocity in the radial direction would disperse the surround; this attempt also proved futile. It was subsequently found that a surround made of cold rolled steel produced the desired results. The steel surround was conical in shape with an interior and exterior apex angle of

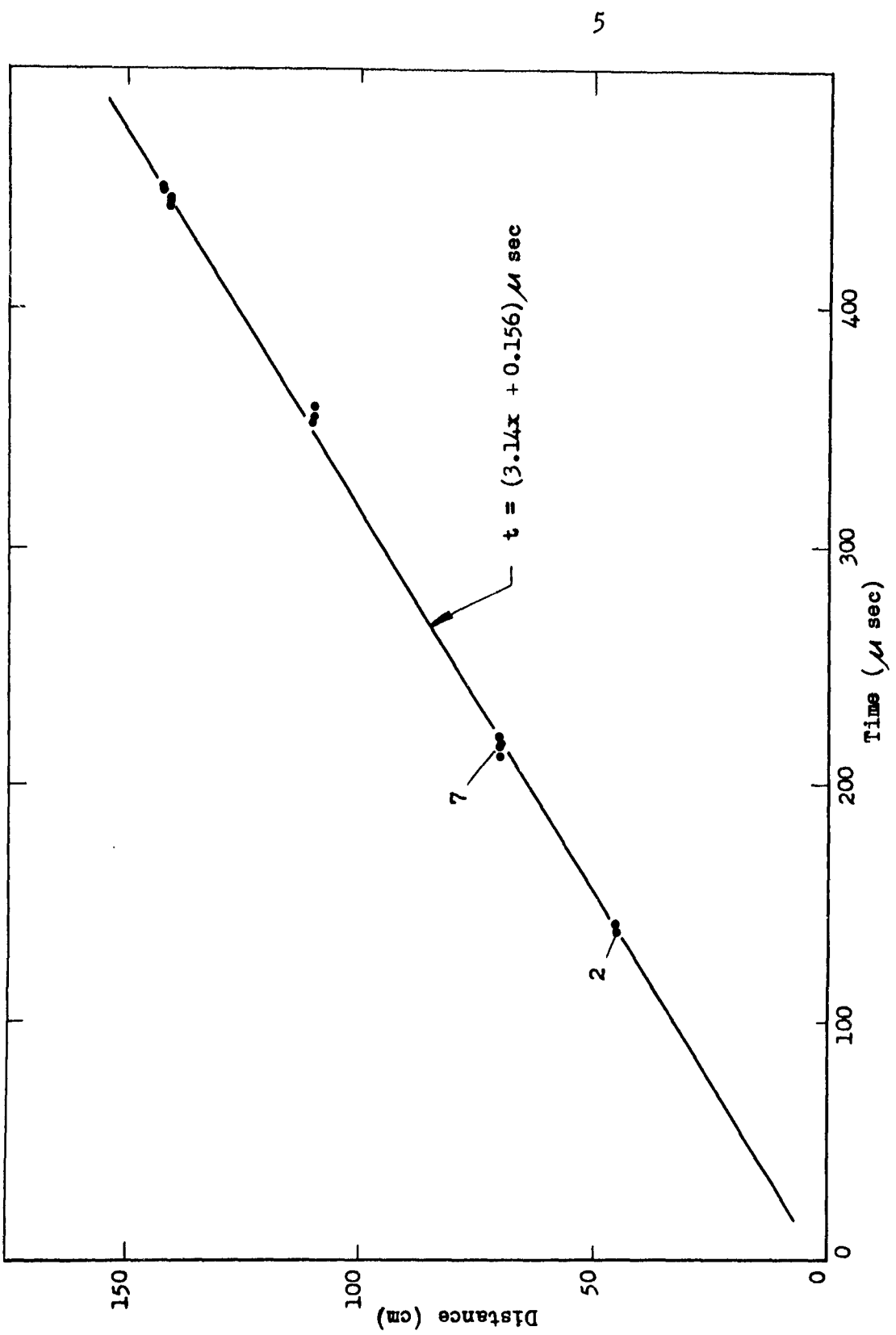
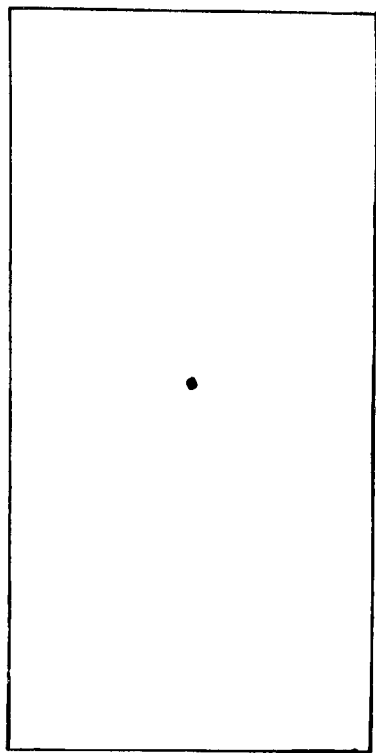
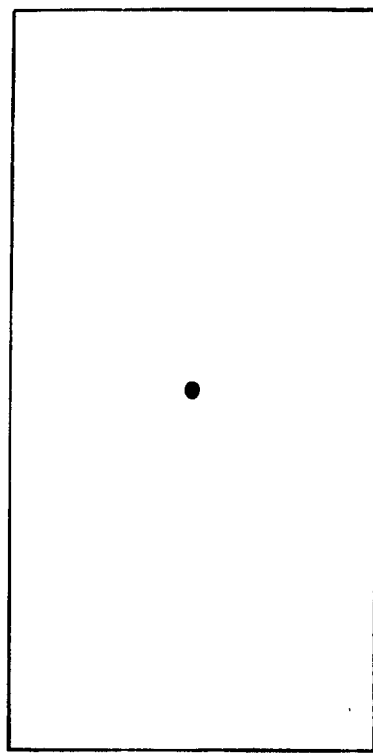


Fig. I-2 Distance vs. time plot for 1 5/8" x 5" Comp. B charge projecting a 1/16" x 1/16" steel projectile.



(a)



(b)

**Fig. I-3 Flash radiographs of hypervelocity projectiles in flight: (a) 3 km/sec projectile ; (b) 4 km/sec projectile.**

175°; the fragment is contained in a hole drilled through the apex of the surround. Dispersal characteristics are quite good; at a standoff of 12 in. the surround disperses outside a 3 in. circle. With dispersal characteristics of this quality, all the secondary fragments produced by the surround can be eliminated by firing the projectile through an orifice.

The distance-time data for the projectile are presented in Table I-1. Figure I-2 is a graphical representation of these data; a linear fit by least square methods produces the equation

$$t = (3.14x + 0.156) \mu \text{ sec}$$

$$v = 3.18 \text{ km/sec} .$$

The recovered mass of the projectile has the value  $0.0234 \pm 0.0010$  grams. A flash radiograph of the projectile in flight, shown in Fig. I-3(a), shows that the projectile is intact.

#### 4 km/sec Projector

Since continued investigations with point initiated solid charges led to the conclusion that the maximum velocity attainable by this method was about 3 km/sec, a different explosive technique was sought for the attainment of higher velocities. Experiments by other investigators in this field have indicated that higher velocities may be attainable through the use of peripheral initiation. It was noted that a critical feature of peripheral initiation is

Table I-1. Tabulation of distance vs time data for the 3 km/sec fragment projector. The projector utilizes a 1-5/8 in. x 5 in. Comp. B charge and 1/16 in. x 1/16 in. steel fragment.

Distance (cm)	Time ( $\mu$ sec)	Distance (cm)	Time ( $\mu$ sec)
46.0	141.4	70.0	214.5
46.0	144.5	70.0	209.6
46.0	141.5	110.0	352.0
70.0	215.9	110.0	354.9
70.0	216.9	110.0	359.3
70.0	216.4	141.0	443.4
70.0	216.9	141.0	446.8
70.0	218.1	141.0	445.8
70.0	214.7	141.8	451.3
70.0	215.0	142.8	450.5

Table I-2. Tabulation of distance vs time data for the 4 km/sec fragment projector. The projector is a peripherally initiated Comp. B charge with an  $\ell/d$  ratio of 0.8.

Chronograph		Flash Radiograph	
Distance (cm)	Time ( $\mu$ sec)	Distance (cm)	Time ( $\mu$ sec)
30.5	71.7	32.0	74.0
30.5	71.0	62.0	150.0
30.5	73.2	61.0	146.0
70.0	168.6	61.3	157.0
70.0	175.2	57.7	141.0
70.0	169.9	58.9	149.1
100.0	248.4	61.1	157.0
100.0	252.1	102.2	257.0
100.0	266.1	104.0	262.0
152.4	396.6	108.9	287.4
152.4	387.6	113.6	286.8
152.4	399.5	112.2	287.1
		110.6	287.3

the charge length to diameter ratio and that maximum projectile velocities are obtained when this ratio has the value  $0.8^{\frac{1}{2}}$ .

Making use of this information, a successful projector in the 4 km/sec region was designed. The pertinent features of this projector are shown in Fig. 1-1(b). It is a  $1\frac{5}{8}$  in x 1.3000 in. Comp. B (60RDX/40TNT) cylinder, cast onto a conical steel surround. A  $1\frac{5}{8}$  in. x 1 in. lucite plug is fixed to the top of this cylinder, around which another  $\frac{1}{4}$  in. of Comp. B has been cast. The latter casting is the peripheral initiator. A tetryl booster is fixed to the top of the charge. The booster is initiated with a length of primacord (PETN) detonated with a No. 8 electric detonator. The primacord is imbedded in a machined lucite holder to ensure co-axiality throughout the projector.

The projectile material is No. 26 music wire machined to a length of  $1\frac{1}{16}$  in. It was found that this type steel remained intact during the high acceleration period more consistently than drill rod or mild steel. Recovered mass data for this projectile has not yet been completed, but flash radiographs show that it is staying

---

<sup>1/</sup> R. J. Eichelberger, W. F. Donaldson, J. A. Dreesen, "The Peripherally Initiated Fragment Gun", Misznay-Schardin Effect, Carnegie Institute of Technology, Contract No. DA-36-061-ORD-122, August 31, 1952.

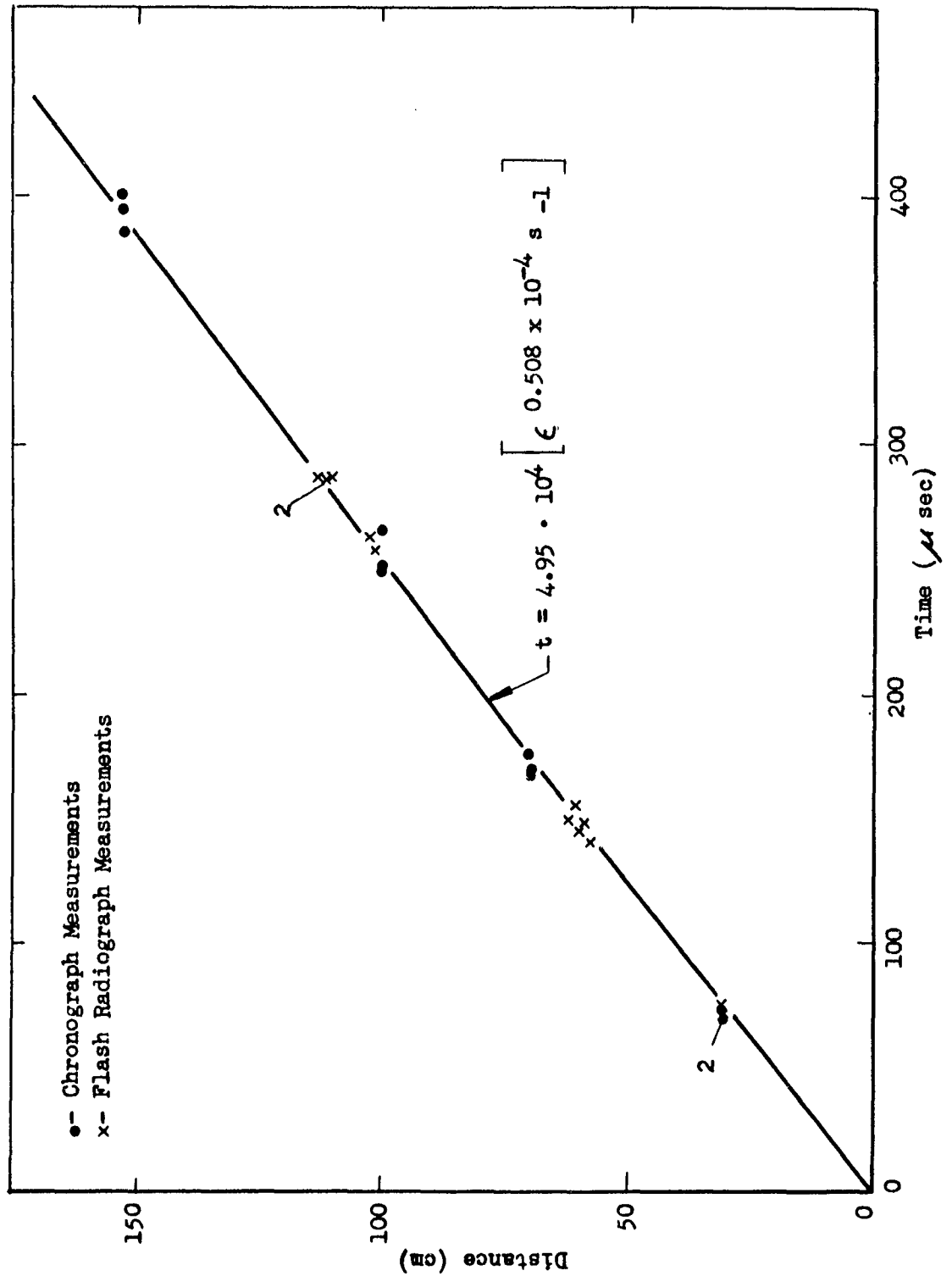


Fig. I-4. Distance vs. time plot for peripherally initiated Comp. B charge with an  $Z/d$  ratio of 0.8.

intact approximately 90% of the time. A typical radiograph of the intact fragment may be seen in Fig. 1-3(b).

The distance-time data is tabulated in Table I-2; and is represented graphically in Fig. 1-4. The equation for the curve has been derived using air drag considerations and has the form

$$t = \frac{2m_f}{\rho_A A_f} \frac{1}{V_0} \left[ (\exp \frac{\rho_A A_f}{2m_f} s) - 1 \right] = 4.95 \cdot 10^4 \left[ (\exp 0.508 \times 10^{-4}) - 1 \right] \mu \text{ sec}$$

$$v = V_0 \exp \left( - \frac{\rho_A A_f}{2m_f} s \right) = 0.398 \exp \left( - 0.508 \cdot 10^{-4} s \right) \text{ cm}/\mu \text{ sec}$$

where  $m_f$  and  $A_f$  are the mass and cross sectional area of the fragment respectively; and  $\rho_A$  is the density of air.

### Conclusion

In the development of the projectors discussed in the foregoing pages various aspects of hypervelocity projecting techniques became apparent and are enumerated below.

- (1) A point initiated, solid, unconfined charge of Comp. B produces a maximum projectile velocity of 3.2 km/sec. This is in good agreement with experimental results from flat plate projection. The possibility still exists however, that other explosives with higher detonation rates, could produce higher velocity projectiles.

- (2) In all projectors tested, one of the most critical features of the charge assembly is co-axiality. Lack of co-axiality results in loss of accuracy, velocity, and consistency. This was particularly noticeable for peripheral initiated charges.
- (3) Associated with increasing the velocity of projectiles is an increase of impulsive load delivered to the projectile. As this load increases, the metallurgical aspects of the projectile material become more important. Increases in both hardness and strength become necessary in order that the projectile remain intact. Treated drill rod projectiles such as those used in the 3 km/sec projector, does not stay intact when used in the 4 km/sec projector, hence, a material of higher strength was used successfully (music wire). In view of this, it is recommended that a thorough investigation be conducted to find suitable materials for the higher velocity projectiles.
- (4) Air drag effects start to become noticeable when working with velocities above 3.5 km/sec and the standoff becomes an important factor.

- A - Steel rod embedded in wall  
 B - Wood charge holder  
 C - 3.16 km/sec fragment projector  
 D - Steel blast plate  
 E - Target, 3" x 5"  
 F - Steel shooting stand  
 G - Witness foil - 1 mil thick  
 2 S-0 Aluminum; 18" x 18"  
 H - Cellotex - 1/2" thick; 18" x 18"

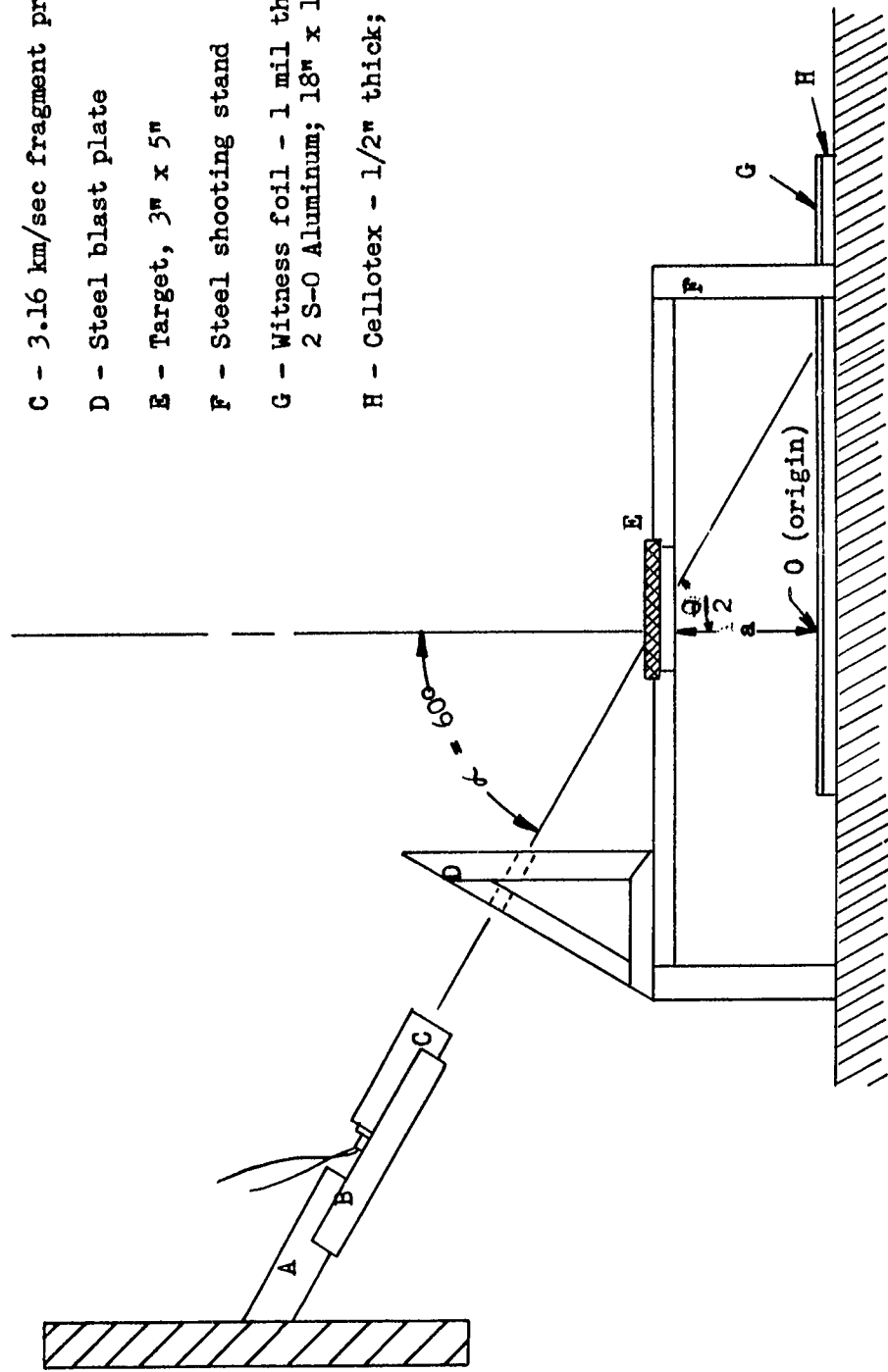


Fig. II-1 Sketch of the apparatus used for obtaining dispersion data at 60 degree obliquity.

Chapter II - Spacial Distribution of Fragments Behind Thin Targets.  
- R. K. Becker and R. Vitali

Introduction

The work covered by this chapter deals with the spacial distribution of material emanating from the rear of thin targets. The material includes projectile particles, ejected target material, and spall. The term "spall fragments" is sometimes used loosely here and is intended to mean any of these materials. The targets were penetrated by a projectile having about 3.2 km/sec velocity and about 23.5 mg mass. The scope of the work involves five target materials, 3 to 5 target thicknesses, and two obliquities ( $0^\circ$  and  $60^\circ$ ). Most of the data obtained are associated with a weighted count of the number of particles ejected into the space behind the target as a function of some spacial coordinate. Also presented, are data associated with the mass and size of the spall fragments. Data relative to the velocity of the material are not sufficient in quality or quantity to warrant discussion at this time.

Experimental Procedure

Figure II-1 illustrates the arrangement of apparatus used for the  $60^\circ$  obliquity shots; the arrangement for  $0^\circ$  obliquity shots was similar except that  $\alpha = 0$ . The figure shows a fragment projector (explosive charge) mounted on a fixed steel shaft. The charge is positioned so that the fragment is projected through a

small hole in a blast plate. The dispersal characteristics of the surround are such that none of the surround fragments are propelled through the hole; they are instead, absorbed by outer areas of the blast plate. The target plate is mounted horizontally in a steel frame behind the blast plate. At a distance a below the target plate is the witness target consisting of 1 mil thick aluminum foil on top of 1/2 in. celotex. The witness target is 18 in. square. For counting purposes, the witness target was divided into from 15 to 25 concentric circles having successively increasing radii of 1/2 in. The origin of the family of circles, for both the 0° and 60° shots, is directly below the hole in the target plate (at point O in Fig. II-1). In practice the origin was determined after the shot to allow for errors in marksmanship and the circles were actually contained on a transparent templet. The templet was centered on the witness target and the number of spall particles was counted in each ring.

It seemed desirable to be able to present the data in some manner that would indicate the relative population densities of spall particles projected into various space elements beyond the target plate. The count by rings would obviously need to be weighted because the count was taken from rings having unequal areas, rings which are unequal distances from the source (bottom of the hole in the target plate) and rings which have different orientations with respect to radius vectors drawn from the source. One method of weighting the original count would be to find the incremental change

in solid angle  $\Omega$  between members of a family of cones defined by a point located at the source and the rings on the witness target. The  $\Delta \Omega$  increments can be found from the relation

$$\Delta \Omega = \frac{-2\pi a}{(r^2 + a^2)^{\frac{1}{2}}} \left| \frac{r^2}{r_1} \right|$$

where  $a$  is the perpendicular distance between the target plate and witness target, and  $r$  is the radial distance on the witness target measured from point 0. The equation given above can be derived by applying the basic definition of the solid angle to the particular geometry of the experimental set-up used here. Weighting is accomplished by using the quantities  $1/\Delta \Omega$  as weighting factors. The resulting weighted quantities may then be thought of as population densities since they represent the number of particles per unit solid angle. The "densities" can then be plotted against coordinates which define the direction in the space behind the target.

#### Dispersion Data at Zero Degrees Obliquity

A representation of these data is accomplished by plotting the population densities against the solid angle  $\Omega$ . The data need to be plotted against only one coordinate because of circular symmetry; the "densities" are independent of a coordinate  $\phi$  which defines angular positions around the rings (this is not so for the  $60^\circ$  obliquity data). The five groups of data corresponding to five target

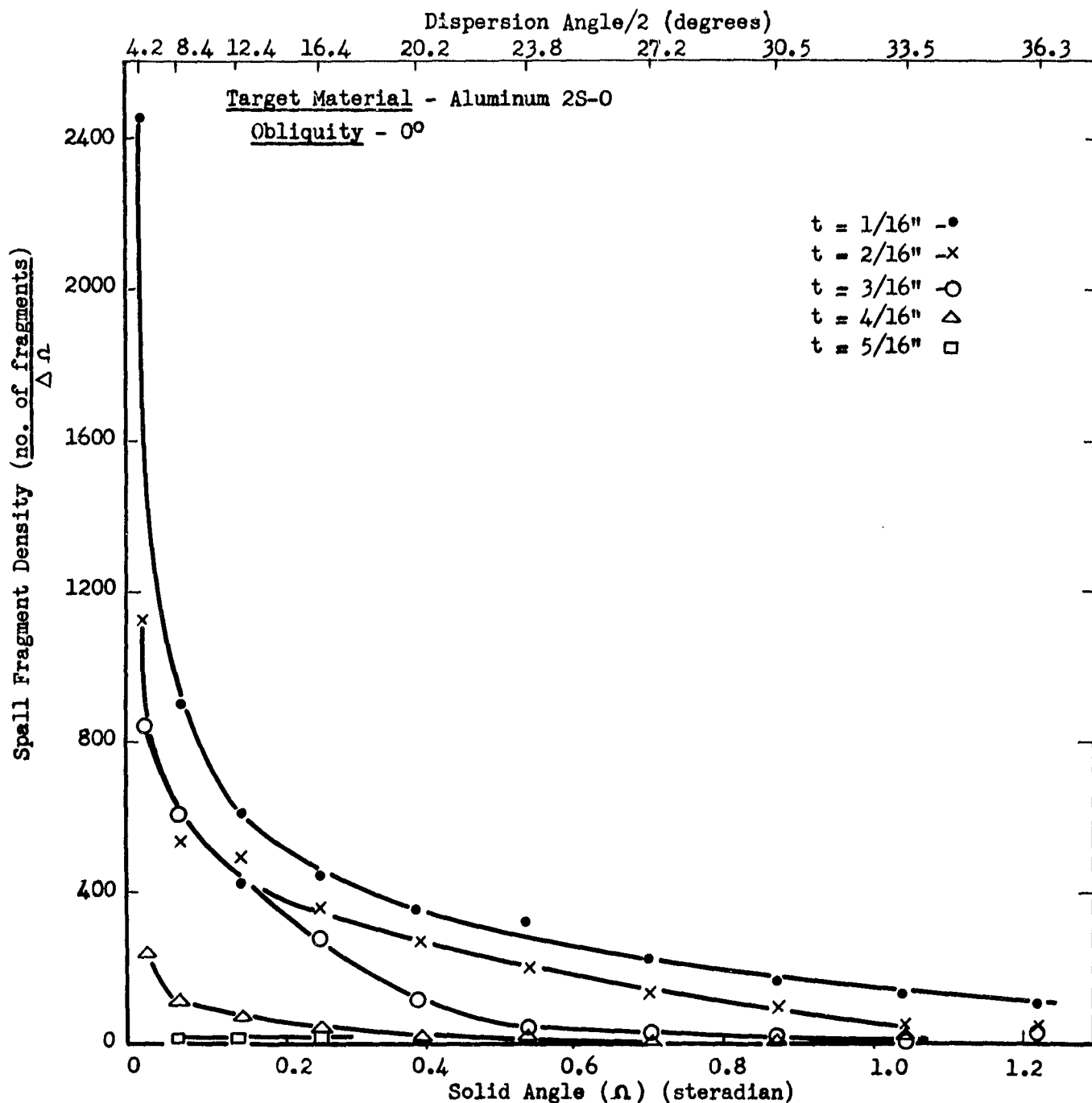


Fig. II-2 Plot of the dispersion data obtained from firing 3.17 km/sec projectiles through various thicknesses of Aluminum 2S-0 thin targets. The spall particles were counted with the aid of a witness target (1 mil aluminum foil on top of cellotex) located 6.8 inches from the thin target plates.

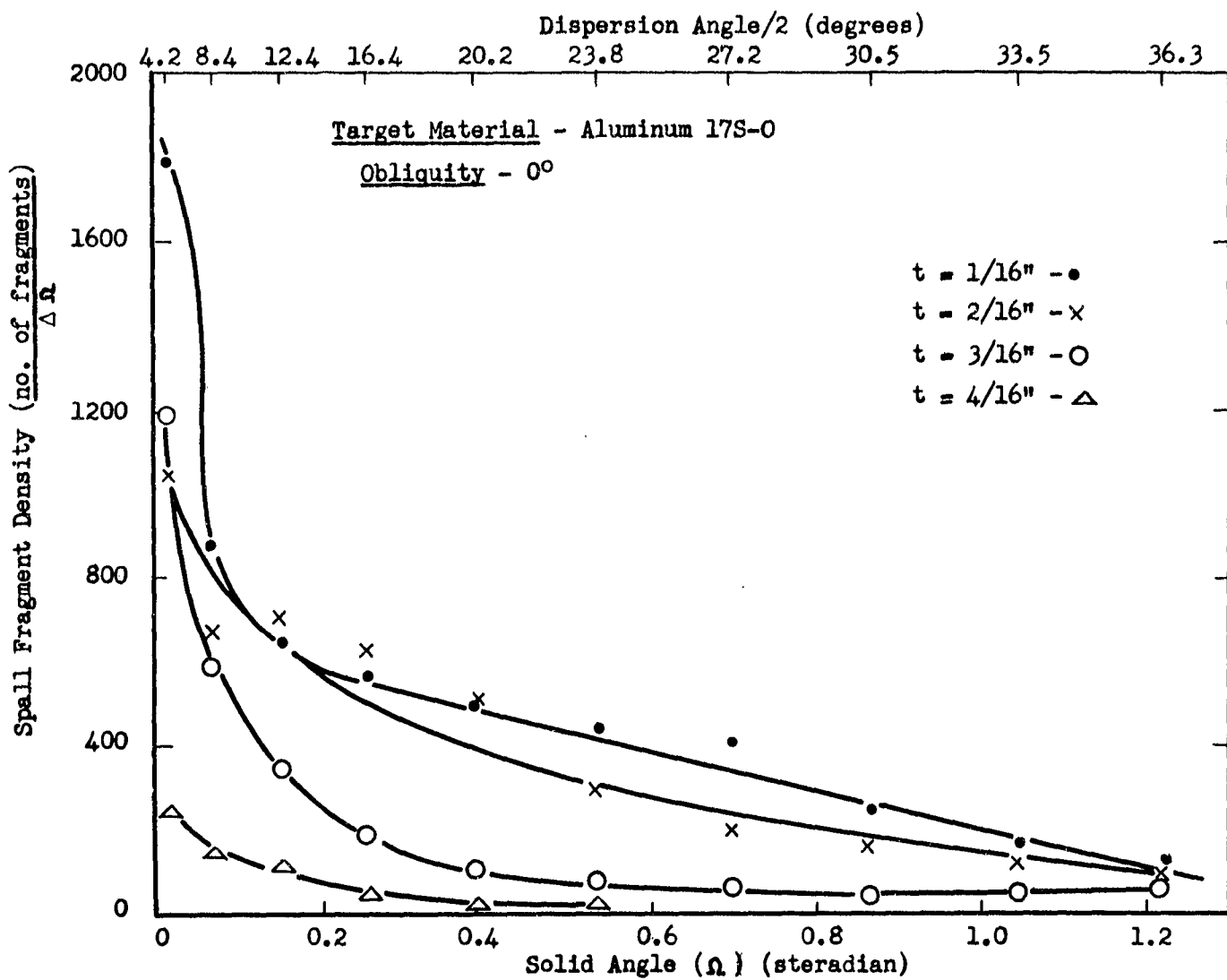


Fig. II-3 Plot of the dispersion data obtained from firing 3.17 km/sec projectiles through various thicknesses of Aluminum 17S-0, thin targets. The spacial distribution of spall fragments was determined with the aid of a witness target (1 mil aluminum foil on top of cellotex) Located 6.8 inches from the thin target plates.

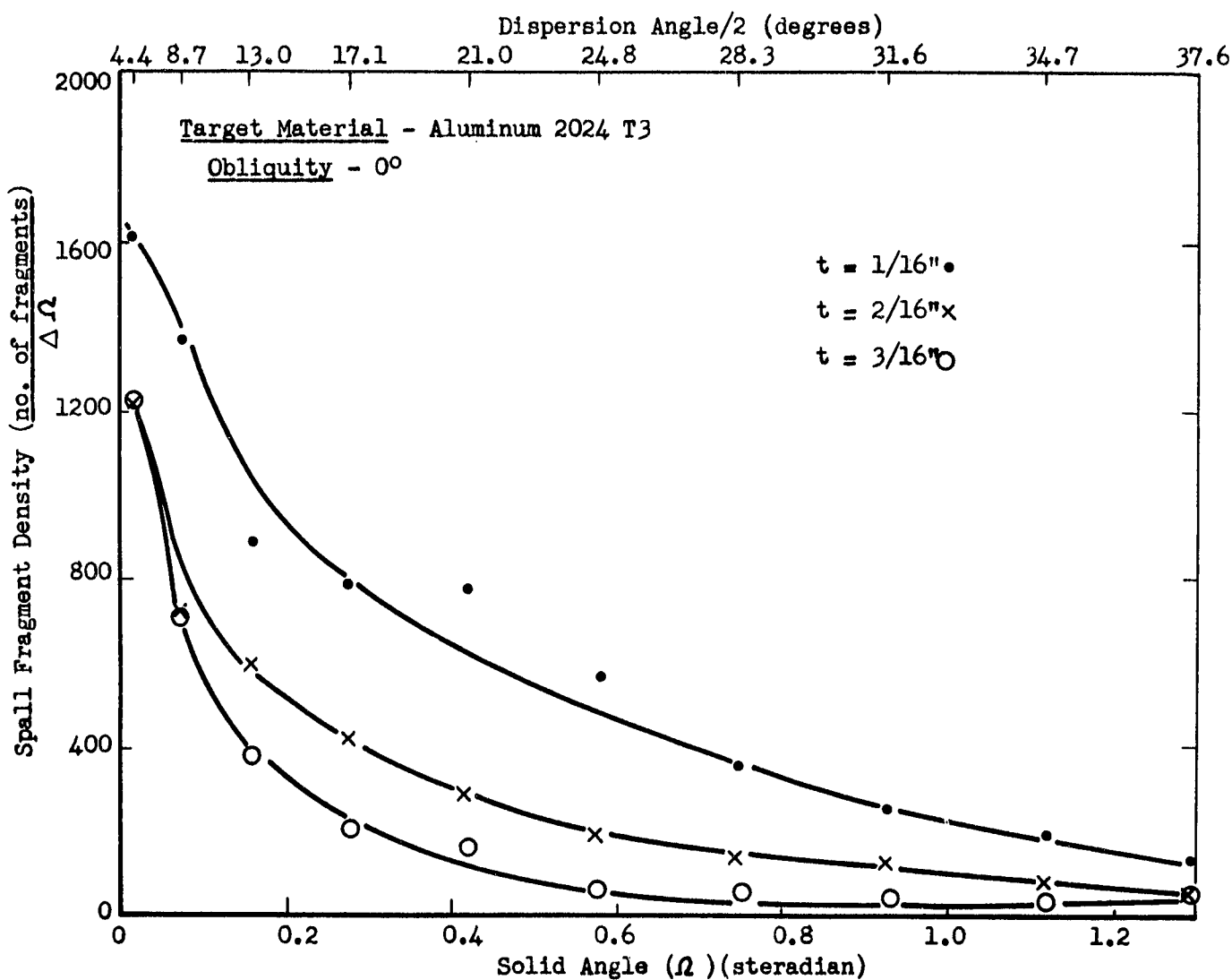


Fig. III-4 Plot of the dispersion data obtained from firing 3.17 km/sec projectiles through various thicknesses of Aluminum 2024 T3. The spacial distribution was determined with the aid of a witness target (1 mil aluminum foil on top of cellotex) located 6.5 inches beyond the aluminum targets.

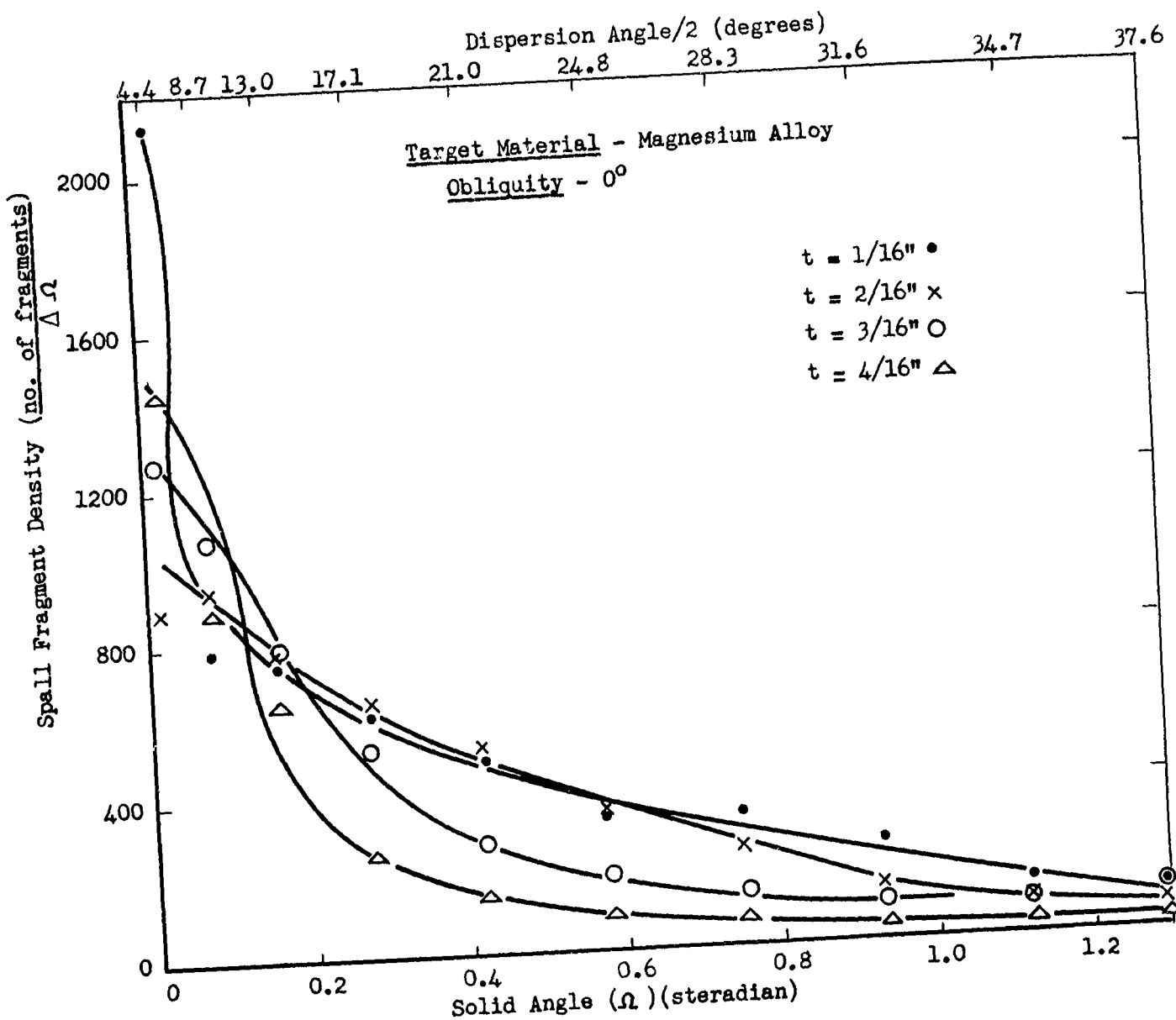


Fig. II-5

Plot of the dispersion data obtained from firing 3.17 km/sec projectiles through various thicknesses of thin, Magnesium alloy targets. The spacial distribution was determined with the aid of a witness target (1 mil aluminum foil on top of cellofex) located 6.5 inches from Magnesium targets.

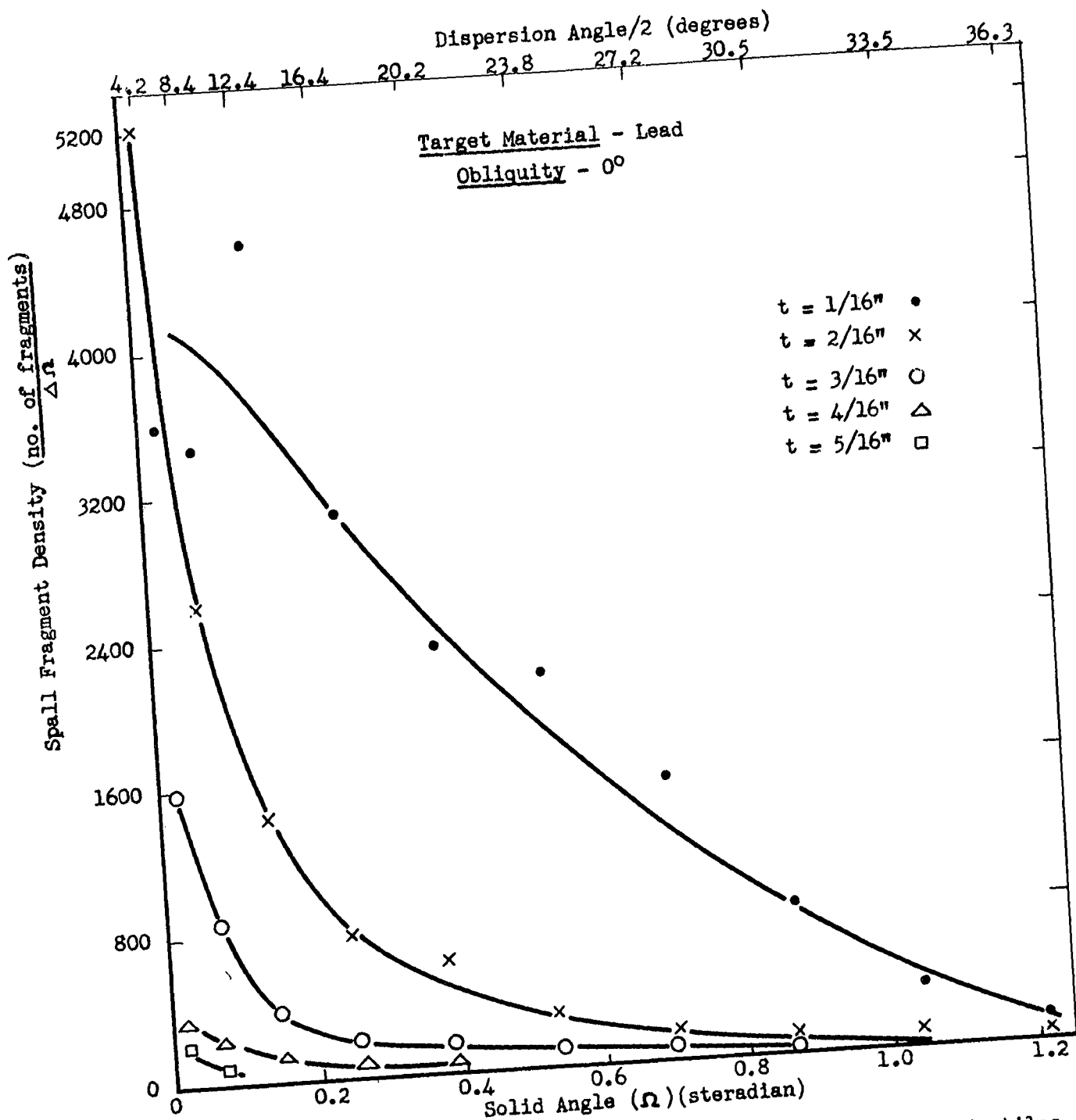


Fig. II-6 Plot of the dispersion data obtained from firing 3.17 km/sec projectiles through various thicknesses of thin lead targets. The spacial distribution of spall fragments was determined with the aid of a witness target (1 mil aluminum foil on top of celotex) located 6.8 inches from the thin target plates.

materials are plotted and tabulated in figures and tables identified below:

Target Material	No. of Thicknesses Tested	No. of Shots per Thickness	Figure No.	Table No.
Al. 2S-0	5	5	II-2	II-2
Al. 17S-0	5	5	II-3	II-3
Al. 2024-T3	3	3	II-4	II-4
Mg. Alloy (AZ51X, B90-46T)	4	3	II-5	II-5
Lead	5	5	II-6	II-6

Note: Table II-1 contains miscellaneous data and information applying to all the target materials, e.g. Barcol hardness number, maximum penetration in thin targets, and total number of particles per thickness of material.

Certain qualitative aspects of the data are similar for all five target materials:

- (1) The preponderance of data shows that the population density of spall particles is maximum in the first element of solid angle determined by the center ring on the witness target.
- (2) The population density is a monotonically decreasing function of the solid angle and/or dispersion angle  $\theta$  (a scale of  $\theta/2$  is included at the top of each plot). The densities decrease to one-half their maximum values at  $\theta/2$  values ranging from about  $5^\circ$  to  $20^\circ$ ; a value of about  $10^\circ$  is perhaps typical. At  $\theta/2 = 45^\circ$ , the densities are essentially negligible.

Table II-1. Tabulation of the total number of ejected particles vs target thickness for various targets impacted at 0° and 60° obliquity. Also tabulated are hardness and maximum penetration data.

Target Material	Total No. of Particles		Hardness Barcol No.	*Maximum Penetration for Thin Targets	
	(0°)	(60°)		(0°)	(60°)
Al. 2S-0	—	—	42.6	$\frac{4}{5}/16$ (100%) $\frac{5}{16}/16$ (20%)	$\frac{3}{5}/32$ (100%) $\frac{3}{16}/16$ (20%)
	1/16	433			
	2/16	284			
	3/16	177			
	4/16	60			
	5/16	38			
	—	—			
	—	—			
Al. 17S-0 (24S-0)	1/16	527	70.7	$\frac{4}{5}/16$ (100%) $\frac{5}{16}/16$ (10%)	2/16 (100%)
	2/16	411			
	3/16	196			
	4/16	63			
	5/16	29			
	—	—			
	—	—			
	—	—			
Al. 2024-T3	1/16	688	84.1	$\frac{3}{4}/16$ (100%) $\frac{4}{16}/16$ (0%)	$\frac{3}{5}/32$ (100%) $\frac{2}{16}/16$ (67%) $\frac{5}{32}/16$ (0%)
	2/16	316			
	3/16	207			
	—	—			
	—	—			
Mg. Alloy (AZ51X,B90-467)	1/16	518	65.4	5/16 (100%)	
	2/16	454			
	3/16	435			
	4/16	272			
	5/16	83			

Table II-1. (Continued)

Target Material	Total No. of Particles	Hardness Barcol No.		*Maximum Penetration for Thin Targets (60°)
		(0°)	(60°)	
Lead	$\bar{N}$	$\sigma$	$\bar{N}$	
	1/16	2087	577	81
	3/32	---	---	43
	2/16	613	39	20
	5/32	---	---	4
	3/16	224	50	--
	4/16	103	63	--
	5/16	65	19	--

Notes:  $\sigma$  is an estimate of the standard deviation per individual observation.

\*This data gives a rough indication of the percentage of times the projectile will penetrate the indicated target thickness.

Table II-2. Tabulation of the dispersion data obtained from 3.17 km/sec projectiles shot through various thicknesses of aluminum 2S-0 targets at  $0^{\circ}$  obliquity. The spacial distribution of the spall products was determined with the aid of a witness target located 6.8 in. from the thin target plates.

Average Number of Spall Fragments Found in $\Delta \Omega$									
Solid Angle	$\Omega$	$\Delta \Omega$	(1/16)	(2/16)	Target Thickness (in.)	(3/16)	(4/16)	(5/16)	$\bar{N}$
0.017	0.017	*	42.0 (2,470)	7.0 (1,130)	19.2 (1,130)	9.6 (847)	14.4 (847)	7.3 (247)	4.2 (247)
0.067	0.050		45.0 (900)	13.5 (540)	27.0 (502)	12.3 (616)	30.8 (616)	12.9 (112)	5.6 (112)
0.148	0.081		50.4 (620)	14.3 (502)	40.8 (502)	9.6 (368)	35.0 (430)	8.9 (280)	6.4 (79)
0.255	0.107		48.0 (448)	10.8 (368)	39.4 (368)	11.0 (368)	30.0 (280)	7.0 (280)	5.2 (49)
0.386	0.131		47.8 (365)	7.7 (266)	34.8 (266)	4.5 (266)	14.2 (108)	3.1 (108)	1.6 (12)
0.534	0.148		47.8 (323)	10.7 (207)	30.6 (207)	5.0 (207)	6.5 (144)	4.1 (144)	3.6 (24)

Table II-2. (Continued)

Solid Angle		Average Number of Spall Fragments Found in $\Delta\Omega$				
$\Omega$	$\Delta\Omega$	(1/16)	(2/16)	(3/16)	(4/16)	(5/16)
		$\bar{N}$	$\sigma$	$\bar{N}$	$\sigma$	$\bar{N}$
0.697	0.163	35.8 (221)	12.4	22.6 (139)	4.5	5.2 (32)
0.867	0.170	30.4 (178)	14.3	16.8 (98)	4.3	3.0 (18)
1.043	0.176	25.0 (142)	8.2	9.8 (56)	5.3	3.6 (20)
1.221	0.178	18.6 (105)	9.1	9.2 (52)	4.7	6.2 (35)

**Notes:**

(1) For counting purposes, the witness target was originally divided into a series of concentric circles with a  $\Delta r$  of  $1/2$  inch. The solid angle increments were calculated from this geometry.

(2) \* Numbers in parentheses are  $\bar{N}/\Delta\Omega$ .

(3)  $\sigma$  is the standard deviation per individual observation.

Table II-3. Tabulation of the dispersion data obtained from 3.17 km/sec projectiles shot through various thicknesses of aluminum 17S-0 targets at 0° obliquity. The spacial distribution of the spall products was determined with the aid of a witness target (1 mil aluminum foil on top of celotex) located 6.8 in. from the thin target plates.

		Average Number of Spall Fragments Found in $\Delta\Omega$														
		(1/16)			(2/16)			Target Thickness (in.)			(4/16)			(5/16)		
$\Omega$	$\Delta\Omega$	$\bar{N}$	$\sigma$	$\bar{N}$	$\sigma$	$\bar{N}$	$\sigma$	$\bar{N}$	$\sigma$	$\bar{N}$	$\sigma$	$\bar{N}$	$\sigma$	$\bar{N}$	$\sigma$	
0.017	0.017 *	30.6 (1,799)	8.0	(1,047)	17.8 5.7	(1,188)	20.2 5.3	(247)	4.2 2.2	(0)	0	(0)	0	0	0	
0.067	0.050	43.8 (876)	11.4	(676)	33.8 4.2	(592)	29.6 9.8	(148)	7.4 4.7	(12)	0.8	27	0.6	0.8	0.6	
0.148	0.081	52.6 (647)	9.7	(711)	57.8 11.8	(344)	28.0 9.6	(116)	9.4 4.8	(5)	0.8	0.4	0.5	0.4	0.5	
0.255	0.107	61.4 (573)	9.4	(628)	67.2 12.7	(189)	20.2 5.7	(43)	4.6 2.6	(6)	0.6	0.4	0.6	0.6	0.4	
0.386	0.131	67.4 (514)	4.1	(500)	65.6 12.6	(102)	13.4 3.9	(27)	3.6 2.2	(2)	0.2	1.4	0.2	0.2	1.4	
0.534	0.148	64.6 (437)	11.6	(295)	43.6 18.6	(85)	12.6 3.3	(28)	4.2 2.4	(8)	1.2	1.2	1.2	1.2	1.2	

Table II-3. (Continued)

Average Number of Spall Fragments Found in  $\Delta\Omega$ 

$\Omega$	$\Delta\Omega$	Solid Angle		(1/16)		(2/16)		Target Thickness (in.)		(4/16)		(5/16)	
		$\bar{N}$	$\sigma$	$\bar{N}$	$\sigma$	$\bar{N}$	$\sigma$	$\bar{N}$	$\sigma$	$\bar{N}$	$\sigma$	$\bar{N}$	$\sigma$
0.697	0.163	67.4 (416)	12.4	31.6 (195)	10.2	9.2 (57)	3.5	3.6 (22)	2.0	1.8 (11)	1.0	1.5	
0.867	0.170	42.8 (250)	8.7	25.8 (151)	4.7	7.4 (43)	2.8	5.2 (30)	4.4	1.4 (8)	2.3		
1.043	0.176	30.0 (170)	3.6	19.6 (111)	3.6	8.2 (47)	2.4	4.4 (25)	1.0	3.0 (17)	2.8	2.8	2.8
1.221	0.178	21.0 (118)	3.8	17.4 (98)	2.6	11.6 (65)	2.2	4.2 (24)	1.2	4.6 (26)	3.3		

**Notes:** (1) For counting purposes, the witness target was originally divided into a series of concentric circles with a  $\Delta r$  of 1/2 inch. The solid angle increments were calculated from this geometry.

(2) Numbers in parentheses are  $\bar{N}/\Delta\Omega$ .

(3)  $\sigma$  is the standard deviation per individual observation.

Table III-4. Tabulation of the dispersion data obtained from 3.17 km/sec projectiles shot through various thicknesses of aluminum 2024-T3 targets at  $0^\circ$  obliquity. The spacial distribution of the spall products was determined with the aid of a witness target (1 mil aluminum foil on top of celotex) located 6.5 in. from the thin target plates.

Solid Angle		Target Thickness (in.)				Average Number of Spall Fragments Found in $\Delta\Omega$			
$\Omega$	$\Delta\Omega$	(1/16)	(2/16)	(3/16)	(4/16)	(5/16)	(6/16)	(7/16)	(8/16)
		$\bar{N}$	$\sigma$	$\bar{N}$	$\sigma$	$\bar{N}$	$\sigma$	$\bar{N}$	$\sigma$
0.018	0.018	* 29 (1,612)	7	22 (1,223)	2	22 (1,223)	2	22 (1,223)	7
0.074	0.056	76 (1,375)	18	39 (706)	5	39 (706)	5	39 (706)	10
0.161	0.087	77 (886)	21	52 (598)	4	52 (598)	4	33 (379)	7
0.278	0.117	92 (787)	16	50 (427)	3	50 (427)	3	23 (197)	3
0.419	0.141	110 (785)	16	41 (293)	6	41 (293)	6	23 (164)	6
0.578	0.159	91 (569)	14	30 (188)	4	30 (188)	4	10 (62)	3
0.751	0.173	62 (358)	15	23 (133)	5	23 (133)	5	9 (52)	2

Table III-4. (Continued)

## Solid Angle

$\Omega$	$\Delta\Omega$	Average Number of Spall Fragments Found in $\Delta\Omega$					
		(1/16)		Target Thickness (in.) (2/16)		(3/16)	
		$\bar{N}$	$\sigma$	$\bar{N}$	$\sigma$	$\bar{N}$	$\sigma$
0.932	0.181	14 (24)	2	21 (17)	3	8 (14)	3
1.117	0.185	36 (19)	4	15 (81)	2	7 (38)	4
1.303	0.186	23 (12)	3	9 (48)	1	9 (48)	5
1.487	0.184	16 (87)	2	5 (27)	1	9 (49)	3
1.666	0.179	14 (78)	5	5 (28)	0	7 (39)	2
1.840	0.174	12 (69)	6	2 (11)	1	5 (29)	3

Notes: (1) For counting purposes, the witness target was originally divided into a series of concentric circles with a  $\Delta r$  of 1/2 in. The solid angle increments were calculated from this geometry.

(2) \* Numbers in parentheses are  $\bar{N}/\Delta\Omega$ .

(3)  $\sigma$  is the standard deviation per individual observation.

Table II-5. Tabulation of the dispersion data obtained from 3.17 km/sec projectiles shot through various thicknesses of magnesium alloy targets at 0° obliquity. The spacial distribution of the spall products was determined with the aid of a witness target (1 mil aluminum foil on top of celotex) located 6.5 in. from the thin target plates.

Average Number of Spall Fragments Found in  $\Delta\Omega$

Solid Angle		(1/16)		(2/16)		Target Thickness (in.)		(3/16)		(4/16)	
$\Omega$	$\Delta\Omega$	$\bar{N}$	$\sigma$	$\bar{N}$	$\sigma$	$\bar{N}$	$\sigma$	$\bar{N}$	$\sigma$	$\bar{N}$	$\sigma$
0.018	0.018	* (2,113)	38	15	(890)	16	2	(1,279)	23	9	(1,446)
0.074	0.056	(778)	43	7	(941)	52	2	(1,068)	59	4	(887)
0.161	0.087	(748)	65	10	(782)	68	6	(782)	68	8	(540)
0.278	0.117	(616)	72	13	(633)	74	7	(522)	61	11	(256)
0.419	0.141	(500)	70	6	(514)	72	4	(278)	39	4	(150)
0.578	0.159	(337)	54	4	(356)	57	5	(187)	30	4	(94)
0.751	0.173	(341)	59	7	(243)	42	2	(127)	22	1	(75)

Table III-5. (Continued)

Solid Angle			Average Number of Spall Fragments Found in $\Delta\Omega$						
$\Omega$	$\Delta\Omega$	(1/16)	Target Thickness (in.)			(4/16)			
		$\bar{N}$	$\sigma$	$\bar{N}$	$\sigma$	$\bar{N}$	$\sigma$	$\bar{N}$	$\sigma$
0.932	0.181	45 (250)	5	25 (139)	5	18 (100)	1	8 (44)	0
1.117	0.185	25 (134)	2	15 (81)	1	17 (91)	4	9 (48)	5
1.303	0.186	21 (113)	2	13 (70)	1	21 (113)	6	12 (65)	6
1.487	0.184	13 (71)	5	10 (54)	1	29 (157)	14	15 (81)	11
1.666	0.179	8 (44)	0	7 (39)	2	21 (117)	20	11 (61)	8
1.840	0.174	4 (23)	2	3 (17)	1	15 (86)	15	9 (52)	3

**Notes:** (1) For counting purposes, the witness target was originally divided into a series of concentric circles with a  $\Delta r$  of 1/2 inch. The solid angle increments were calculated from this geometry.

\* Numbers in parentheses are  $\bar{N}/\Delta\Omega$ .

(2)  $\bar{N}$  is the standard deviation per individual observation.

Table II-6. Tabulation of the dispersion data from 3.17 km/sec projectiles shot through various thicknesses of lead targets at 0° obliquity. The spacial distribution of the spall products was determined with the aid of a witness target (1 mil aluminum foil on top of celotex) located 6.8 in. from the thin target plates.

Average Number of Spall Fragments Found in $\Delta \Omega$											
Solid Angle		(1/16)		(2/16)		Target Thickness (in.)		(4/16)		(5/16)	
$\Omega$	$\Delta \Omega$	$\bar{N}$	$\sigma$	$\bar{N}$	$\sigma$	$\bar{N}$	$\sigma$	$\bar{N}$	$\sigma$	$\bar{N}$	$\sigma$
0.017	0.017 *	60.6 (3,563)	45.6	88.6 (5,210)	35.1	26.8 (1,576)	16.2	5.8 (341)	2.8	3.4 (200)	2.2
0.067	0.050	172.4 (3,448)	129.0	130.2 (2,604)	77.9	43.0 (860)	21.3	11.6 (232)	3.0	4.0 (80)	2.1
0.118	0.081	371.2 (4,566)	91.0	116.2 (1,429)	24.0	28.8 (354)	8.4	12.0 (148)	6.8	3.2 (39)	3.7
0.255	0.107	328.8 (3,071)	93.0	81.4 (760)	18.1	21.8 (204)	5.8	10.0 (93)	2.3	4.2 (39)	3.9
0.386	0.131	308.4 (2,353)	92.0	80.8 (616)	24.0	20.0 (153)	6.0	9.2 (70)	1.9	3.8 (29)	4.3
0.534	0.148	319.6 (2,160)	119.1	42.0 (284)	24.8	13.0 (88)	6.3	5.2 (35)	1.6	3.2 (22)	1.6

Table II-6. (Continued)

Average Number of Spall Fragments Found in  $\Delta\Omega$ 

Solid Angle $\Omega$	$\Delta\Omega$	(1/16)				(2/16)				Target Thickness (in.)				(4/16)				(5/16)			
		$\bar{N}$	$\sigma$	$\bar{N}$	$\sigma$	$\bar{N}$	$\sigma$	$\bar{N}$	$\sigma$	$\bar{N}$	$\sigma$	$\bar{N}$	$\sigma$	$\bar{N}$	$\sigma$	$\bar{N}$	$\sigma$				
0.697	0.163	251.2 (1,550)	86.0	28.8 (178)	8.2	12.4 (77)	2.9	4.8 (30)	2.8	2.8 (15)	2.4	1.0									
0.867	0.170	142.0 (831)	97.0	17.4 (102)	7.7	8.0 (47)	7.1	6.6 (39)	2.6	7.0 (41)	5.2										
1.043	0.176	61.4 (349)	34.2	14.4 (82)	4.5	8.8 (50)	4.4	4.2 (24)	1.6	4.4 (25)	3.9										
1.221	0.178	26.2 (147)	18.3	9.6 (514)	1.9	9.0 (51)	2.8	7.2 (40)	3.6	5.6 (31)	4.7										

Notes: (1) For counting purposes, the witness target was originally divided into a series of concentric circles with a  $\Delta r$  of 1/2 inch. The solid angle increments were calculated from this geometry.

(2) \* $N$  numbers in parentheses are  $\bar{N}/\Delta\Omega$ .

(3)  $\sigma$  is the standard deviation per individual observation.

- (3) Variations in the data are quite large. The tables give estimates of the standard deviation per individual observation associated with repeated counts of particles per ring. For the three different types of aluminum targets and for magnesium the standard deviations average out to be about 20% as large as the mean count per ring. For lead targets a similar value of 40% is obtained.
- (4) A very definite correlation exists between the total number of particles produced and the target thickness - the smallest thickness corresponds to the greatest number of particles. This trend may be observed by inspecting data in Table II-1; for example, the aluminum 2S-0 target plates produced 433, 284, 177, 60, and 38 total fragments for corresponding thicknesses of  $1/16$ ,  $2/16$ ,  $3/16$ ,  $4/16$ , and  $5/16$  in. The same trend is evident when one inspects the five plots except that here the total number of fragments have been weighted and divided among the various elements of solid angle. The plots illustrate the correlation very nicely for relatively large solid angles and/or dispersion angle ( $\theta/2 > 15^\circ$ ). It may be noted, however, that in some cases when  $\theta/2 < 15^\circ$  (or  $\Omega < 0.2$ ) that "crossover" points do occur; these are not believed to be significant and are probably due to the fact that the  $\Delta \Omega$  increments are considerably smaller near the origin resulting in a loss of statistical significance.

It should be pointed out at this time that although the greatest number of particles correspond to the smallest target thickness, the greatest number of particles do not correspond to the greatest mass.

The mass of material going into the space behind the target was determined via water recovery techniques. The particles were filtered out, dried, and weighed. The particles were then given a chemical test for iron (which is presumably the recovered projectile mass). A discussion of the recovered projectile masses is found in Chapter III. The remaining material was assumed to be ejected target material including spall and possibly some debris. These data are tabulated in Table II-7.

The total recovered masses do not decrease monotonically with target thickness as was the case for the total number of particles. A typical example is that of the aluminum 2S-0 data; total recovered masses of 35.6, 73.6, 96.2, 37.7, and 7.4 mg correspond to thicknesses of 1/16 in. through 5/16 in. respectively. A maximum mass of 96.2 mg is recovered from the 3/16 in. targets. Similar data is obtained for aluminum 17S-0, aluminum 2024-T3, magnesium alloy, and lead (see Table II-7). Thus, since the number of particles is maximum for 1/16 in. targets and the masses maximum for 3/16 in. targets, one would suspect that the 1/16 in. targets produced particles of smaller average size; this is apparently the case.

A limited amount of data pertaining to the size of particles has very recently been obtained. These data are for aluminum 2S-0 targets having thicknesses of 1/16 in. and 3/16 in. The material

Table III-7. Tabulation of mass recovery data obtained by water recovery techniques. The thin targets were impacted at  $0^\circ$  obliquity by a 23.5 mg projectile having a velocity of 3.17 km/sec.

	Recovered Masses (mg) $\pm \sigma_m$		
	(1/16)	(2/16)	(3/16)
<u>Al. 2S-0 (5 shot data)</u>			
Total Recovered Mass (mg)	35.6 $\pm$ 1.8	73.6 $\pm$ 12.3	96.2 $\pm$ 10.1
Recovered Projectile Mass (mg)	21.2 $\pm$ 0.5	22.7 $\pm$ 0.4	21.5 $\pm$ 0.7
<u>Al. 17S-0 (5 shot data)</u>			
Total Recovered Mass (mg)	54.3 $\pm$ 3.1	92.9 $\pm$ 3.3	115.7 $\pm$ 6.5
Recovered Projectile Mass (mg)	23.6 $\pm$ 1.3	23.0 $\pm$ 0.6	19.8 $\pm$ 1.1
<u>Al. 2024-T3 (3 shot data)</u>			
Total Recovered Mass (mg)	53.1 $\pm$ 1.0	101.3 $\pm$ 3.7	105.7 $\pm$ 11.6
Recovered Projectile Mass (mg)	23.4 $\pm$ 1.2	24.2 $\pm$ 0.5	19.8 $\pm$ 1.3

Table III-7. (Continued)

	(1/16)	(2/16)	Recovered Masses (mg) $\pm \sigma_m$ Target Thickness (in.) (3/16) (4/16)	Recovered Masses (mg) $\pm \sigma_m$ Target Thickness (in.) (5/16)
<b>Magnesium Alloy-</b>				
<b>AZ51X, B90-46T (3 shot data)</b>				
Total Recovered Mass (mg)	43.6 $\pm$ 1.1	78.6 $\pm$ 9.4	97.3 $\pm$ 2.9	121.7 $\pm$ 20.0
Recovered Projectile Mass (mg)	23.0 $\pm$ 0.7	22.4 $\pm$ 0.3	23.0 $\pm$ 1.5	22.0 $\pm$ 0.5
<b>Lead</b>				
<b>(5 shot data)</b>				
Total Recovered Mass (mg)	197.2 $\pm$ 6.6	828.2 $\pm$ 18.2	1,034.4 $\pm$ 29.0	830.2 $\pm$ 24.0
Recovered Projectile Mass (mg)	18.8 $\pm$ 1.2	18.1 $\pm$ 1.6	17.5 $\pm$ 2.3	16.0 $\pm$ 1.0

38

Note:  $\sigma_m$  is an estimate of the standard deviation of the means.

behind the target was collected in water, filtered and sorted out according to size with the aid of screens. Each screened group of particles was then weighed. The results between the 1/16 in. and 3/16 in. thick targets are compared below:

Screen Size	<u>1/16 in. (10 shots)</u>		<u>3/16 in. (5 shots)</u>	
	Average No. of Particles	Average Mass (mg)	Average No. of Particles	Average Mass (mg)
8	0.0	0	0.4	3.3
18	5.2	8.1	15.0	67.4
26	27.1	12.6	12.4	11.0
60	162.0	14.3	56.2	11.1
100	224.0	5.7	86.0	4.3
200	446.0	3.5	175.0	3.8
Total Average	864.3	44.2	345.0	100.9

The screens had a square mesh with a side dimension of 93.7 mils, 39.4 mils, 22.5 mils, 9.8 mils, 5.9 mils, and 2.9 mils for the No. 8 through No. 200 screens respectively. The table above gives the screen size which would not allow the particle to pass through.

It should be pointed out that when one compares the 1/16 in. and 3/16 in. data in the above table a certain inequity is apparent. For a given screen size, the mass per particle is greater for data obtained for the 3/16 in. targets. This would indicate that the screens do not necessarily screen out particles of equal mass and

that the geometrical shape of the particles has some effect on the screening procedure. Nevertheless, some interesting and useful information is obtained from these data.

- (1) These data are in agreement with the dispersion data in that the smaller target thickness corresponds to the greater number of fragments. It should be mentioned that in each case the water recovery count was about twice the count from witness targets; however, it should also be noted that one-half of the count from water recovery techniques is represented by particles counted on the No. 200 screen. These particles are extremely small and a significant number of them are quite likely dust or debris. If these particles are discounted then the count by the two techniques is the same.
- (2) Despite inequities on a screen size basis, the data from the screened particles do clearly indicate that the size or mass per particle is greater for 3/16 in. thick plates. This accounts for a previous result (from mass recovery data and dispersion data) which showed the 3/16 in. plates yielding fewer particles of greater total mass as compared to the greater number of particles with lesser mass obtained for 1/16 in. targets.

Dispersion Data at 60° Obliquity

Target materials investigated at 60° obliquity included at least 3 thicknesses of 2S-0, 17S-0, 2024-T3 aluminum, and lead. An inspection of the witness targets revealed that the distribution of spall particles was not independent of  $\phi$  (the polar angle associated with the rings on the witness target). The lack of circular symmetry results in a distribution of particles that is a function of both  $\phi$  and  $\Omega$ . Thus the basic data are represented by two plots for each target material. One set of plots shows the actual number of fragments plotted against polar angle intervals. For the three types of aluminum the  $\Delta\phi$  intervals are 10°; for lead they are 20°.  $\phi = 0$  is an azimuth on the witness target corresponding to the direction of the horizontal component of velocity of the projectile. The second set of plots is similar to the ones that were presented for the zero degree obliquity data with two exceptions: (1) In most cases the  $\Delta\Omega$  intervals were calculated from  $\Delta r$  intervals of 3/2 in. rather than 1/2 in. (2) The "density" versus  $\Omega$  representations are restricted to a  $\phi$  interval symmetrically spaced about the regions where the maximum number of spall particles were counted. The reason for different choices in the size of  $\Delta\phi$  and  $\Delta\Omega$  lies in the statistical character of the data. It was felt that the size should be large enough to smooth out the data and at the same time small enough to retain reasonable sensitivity. Information relative to the size of the increments chosen may be found in the tables and plots.

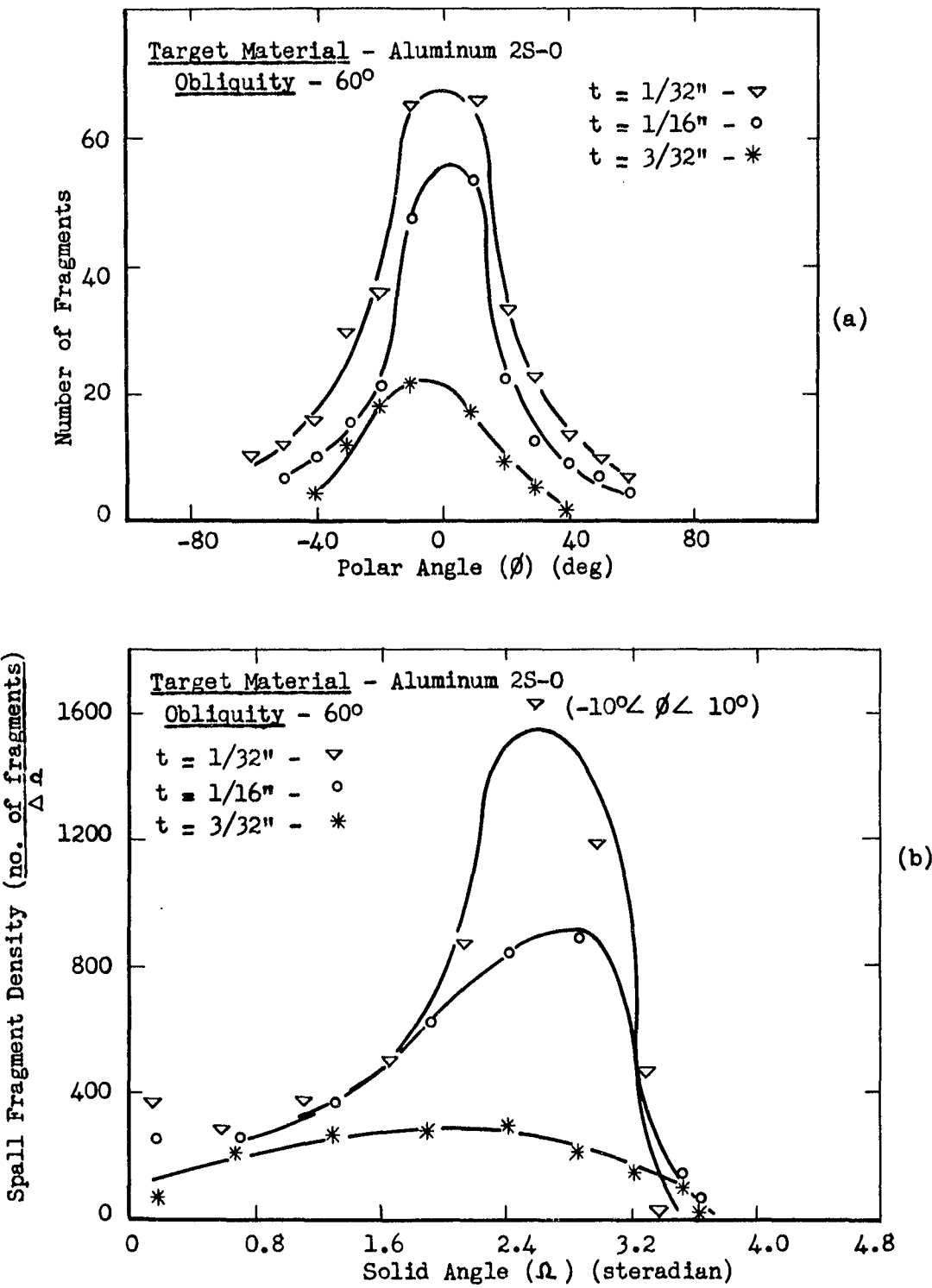


**Fig. II-7** Plot of the dispersion data obtained from tests with Aluminum 2S-0 targets at 60 degrees obliquity. Plots (a) and (b) illustrate, respectively, the directional and radial characteristics of the spall pattern.

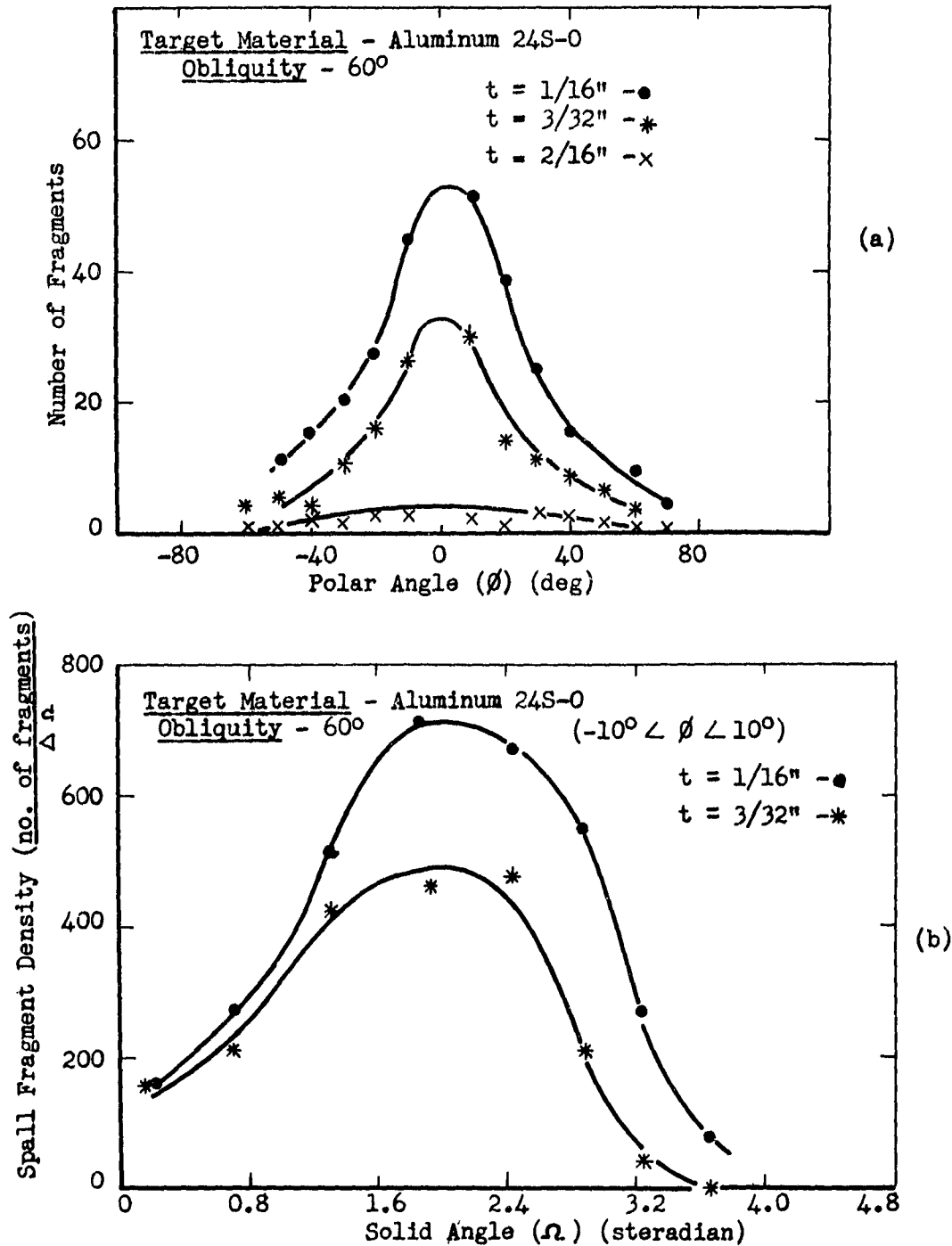


**Fig. II-8** Plot of the dispersion data obtained from tests with Aluminum 24S-0 targets at 60 degree obliquity. Plots (a) and (b) illustrate, respectively, the directional and radial characteristics of the spall pattern.

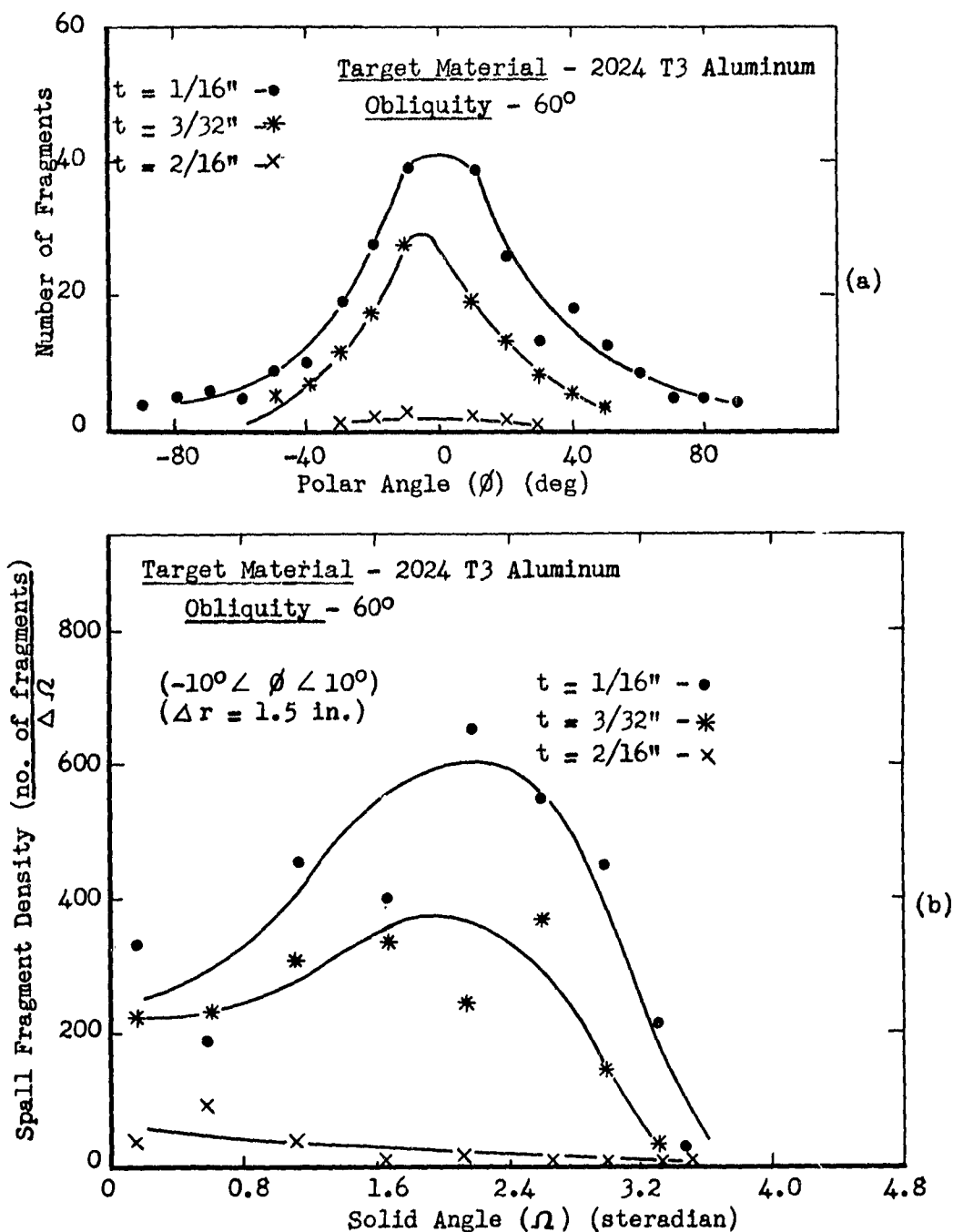


**Fig. II-9** Plot of the dispersion data obtained from tests with Aluminum 2024 T3 at 60 degrees obliquity. Plot (a) and (b) illustrate respectively, the directional and radial characteristics of the spall pattern for various thicknesses of target material.

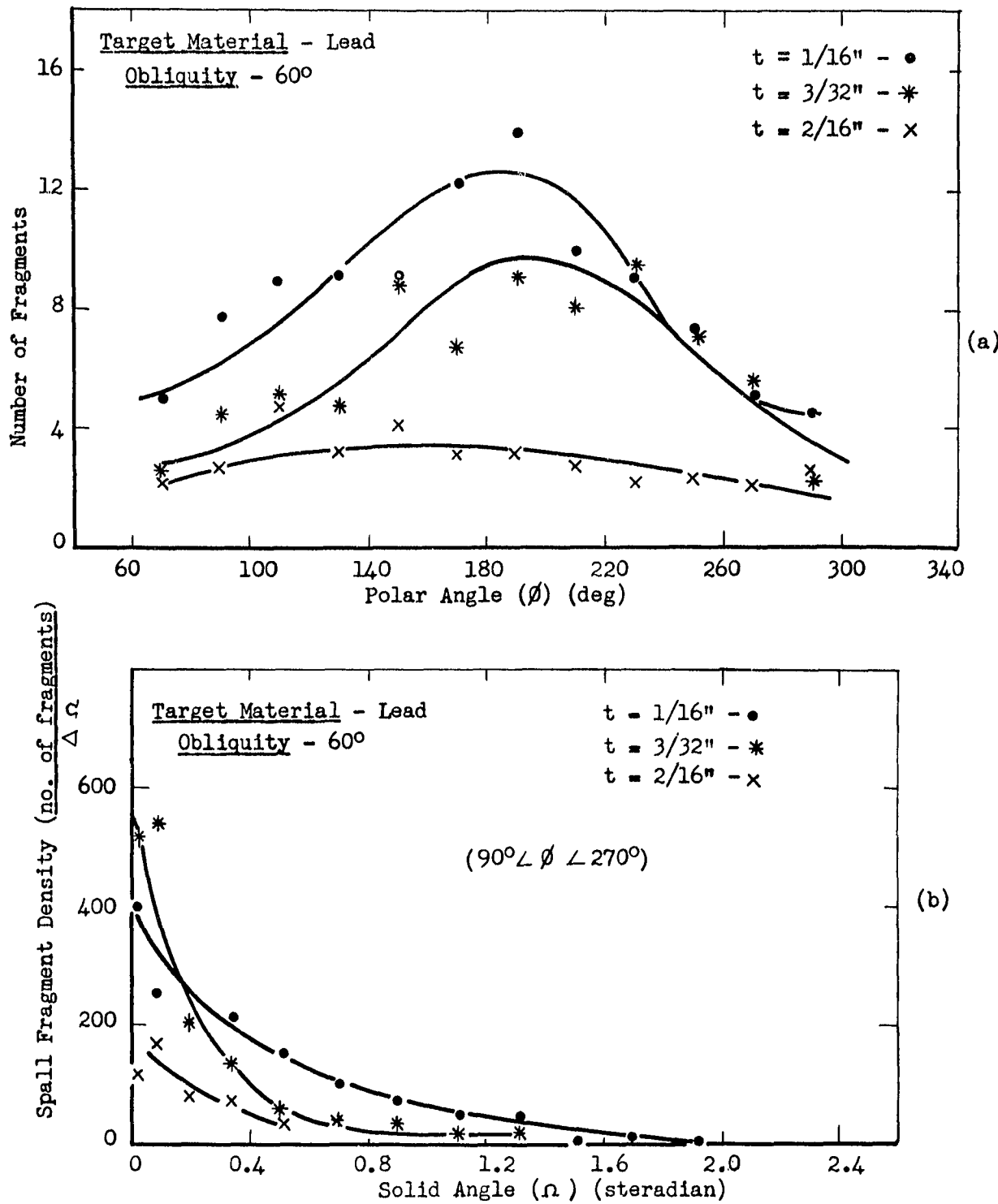


Fig. II-10 Plot of the dispersion data obtained from tests with lead targets at 60 degrees obliquity. Plots (a) and (b) illustrate, respectively, the directional and radial characteristics of the spall pattern.

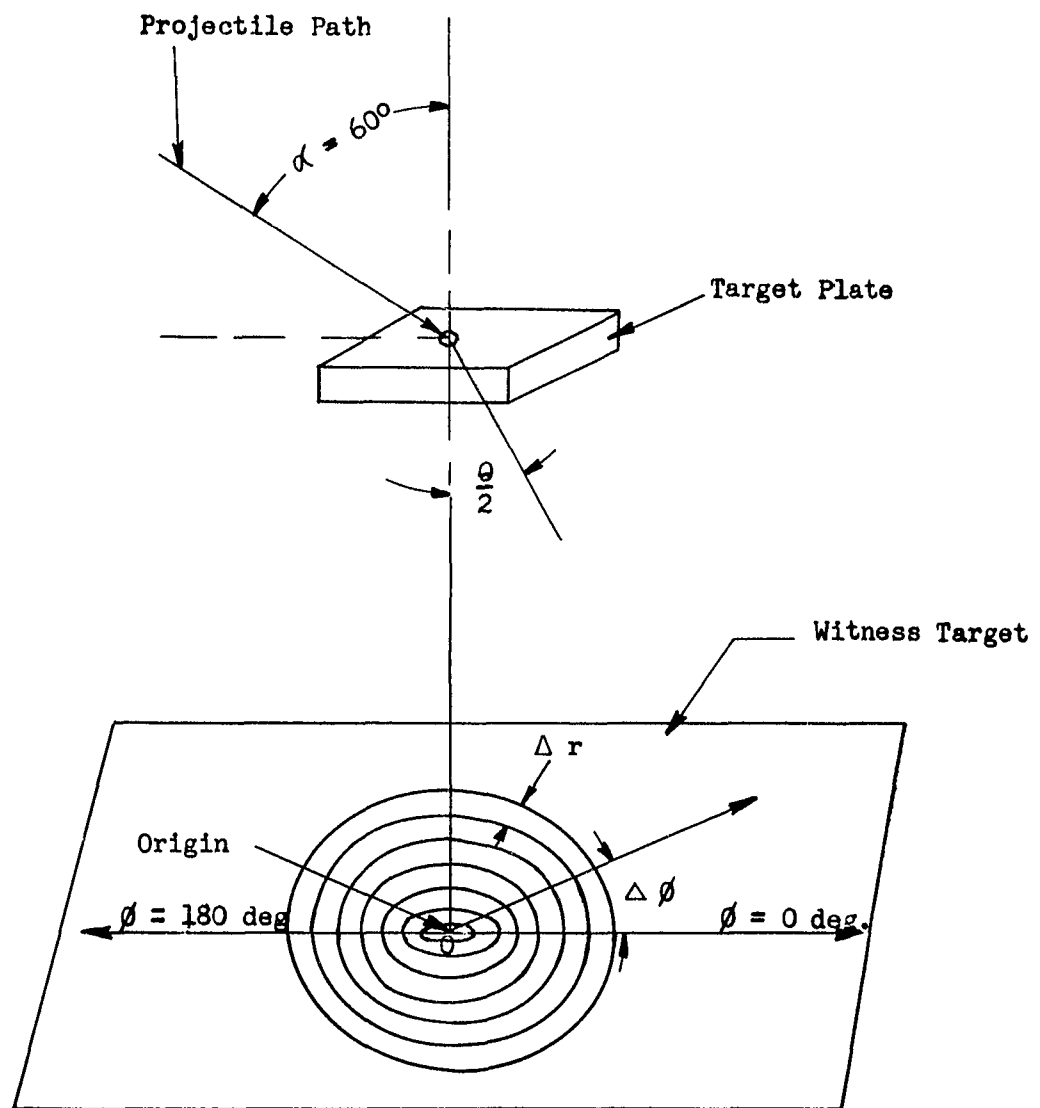


Fig. II-11 Sketch illustrating witness target geometry for 60 degree obliquity shots.

The figure and table numbers pertaining to the data sets plus other relevant information are tabulated below:

Target Material	No. of Thicknesses Tested	No. of Shots per Thickness	Figure No.	Table No.
Al. 2S-0	3	5	II- 7a and 7b	II-8 and II- 9
Al. 24S-0	3	5	II- 8a and 8b	II-10 and II-11
AL. 2024-T3	3	3	II- 9a and 9b	II-12 and II-13
Lead	4	5	II-10a and 10b	II-14 and II-15

The overall character of the data is such that the data appear to belong in two distinct groups: (i) the three aluminum metals, (ii) lead. The separation is due to distinct differences in the distribution of ejected material behind the target. These differences, in addition to other features of the data, are summarized below.

Figure II-11 is presented at this time to aid in the description of certain geometrical quantities used below.

- (1) The distribution of particles ejected into the space behind the target does not exhibit the circular symmetry noted for  $0^\circ$  obliquity data. At  $60^\circ$  obliquity, the angular ( $\phi$ ) distribution for the three aluminum metals exhibits strong directional characteristics in favor of the "forward" direction ( $\phi = 0^\circ$ ). Lead, on the other hand, shows somewhat weaker directional tendencies and the distribution is maximum in the "backward" direction ( $\phi = 180^\circ$ ).

Table II-8. Tabulation of the dispersion data (number of fragments vs polar angle) obtained from tests with aluminum 2S-0 targets at  $60^\circ$  obliquity.

Polar Angle Interval (deg)	Average Number of Fragments Counted in $\Delta \phi$					
	Target Thickness (in.)					
	(1/32)	(1/16)	(3/32)			
0 to 10	64.8	19.2	47.4	17.4	16.6	10.3
10 to 20	32.2	21.0	20.2	16.5	9.0	5.4
20 to 30	21.4	9.8	15.0	12.1	5.0	1.8
30 to 40	12.8	7.2	9.4	6.7	3.2	2.2
40 to 50	8.8	6.3	6.0	3.6	3.4	2.7
50 to 60	6.4	6.3	6.2	3.1	1.8	2.7
60 to 70	7.0	2.7	2.4	1.3	0.6	1.3
70 to 80	5.0	0.9	3.0	2.7	-	-
80 to 90	4.6	2.2	2.6	2.7	-	-
0 to -10	64.4	25.5	52.8	22.8	21.4	13.4
-10 to -20	35.2	20.1	21.8	9.8	18.2	8.1
-20 to -30	29.2	15.2	12.0	2.7	7.2	3.6
-30 to -40	15.4	4.0	8.8	2.7	4.5	4.6
-40 to -50	12.4	7.6	9.4	5.4	4.2	1.8
-50 to -60	10.2	5.8	7.2	1.3	2.8	1.8
-60 to -70	7.4	3.1	4.4	2.2	-	-
-70 to -80	5.8	3.6	5.2	2.2	-	-
-80 to -90	5.2	3.6	3.8	3.1	-	-

- Notes: (1) The polar angle intervals given above are sectors of a circle. The circle lies on the witness target with its center directly beneath the hole in the target plate.
- (2)  $\sigma$  is the standard deviation per individual observation.

Table II-9. Tabulation of the dispersion data (population of fragments vs solid angle in the polar angle interval  $-10^\circ < \theta < 10^\circ$ ) obtained from tests with aluminum 2S-0 targets at  $60^\circ$  obliquity.

Average Number of Spall Fragments Counted in $\Delta \Omega$							
Solid Angle	$t = 1/32$ in.	$\Omega$	$\Delta \Omega \times 10^3$	Solid Angle	$t = 1/16$ in.	$\bar{N}$	$\sigma$
0.161	8.9	(359)	1.3	0.200	11.1	(252)	2.8 1.8 $\sigma$ (54)
0.578	23.1	(277)	5.3	0.702	27.9	(222)	6.2 3.1 $\sigma$ (201)
1.117	29.9	(347)	7.6	1.319	34.2	(362)	12.4 8.9 $\sigma$ (246)
1.666	30.5	(485)	7.1	1.916	33.2	(602)	20.0 5.8 $\sigma$ (265)
2.168	27.9	(853)	13.9	2.439	29.1	(832)	24.2 9.4 $\sigma$ (268)
2.604	24.3	(1,605)	5.8	2.880	24.4	(869)	21.2 3.1 $\sigma$ (205)
2.976	20.6	(1,174)	8.9	3.245	20.3	(502)	10.2 4.5 $\sigma$ (138)

Table II-9. (Continued)

Average Number of Spall Fragments Counted in $\Delta\Omega$					
Solid Angle $\Omega$	$\Delta\Omega \times 10^3$	$t = 1/32$ in.	$t = 1/16$ in.	$t = 1/16$ in.	$t = 3/32$ in.
		$\bar{N}$	$\sigma$	$\bar{N}$	$\sigma$
3.290	17.4	7.8 (148)	7.1	3.549 (142)	16.9 2.4 (142)
3.384	10.1	0.0 (0)	0.0	3.639 (40)	5.0 0.5 (40)

Notes: (1) The numbers in parentheses are  $\bar{N}/\Delta\Omega$  and represent the population of fragments per unit solid angle.

(2) The solid angle given is the end point of the interval.

(3) The  $\Delta\Omega$  elements are associated with circular rings having  $20^\circ$  of arc and a  $\Delta r$  width of 1.5 in. except for the last interval where  $\Delta r = 0.5$  in. The target to witness target distance is 6.5 in. for 1/32 targets and 5.8 in. for other thicknesses.

(4)  $\sigma$  is the standard deviation per individual observation.

Table II-10. Tabulation of the dispersion data (number of fragments vs polar angle) obtained from tests with aluminum 24S-0 targets at  $60^\circ$  obliquity.

Polar Angle Interval (deg)	Average Number of Fragments Counted in $\Delta\phi$					
	Target Thickness (in.)					
	(1/16)	(3/32)	(2/16)			
0 to 10	51.4	5.8	30.2	26.4	2.2	0.9
10 to 20	38.4	5.6	14.8	6.7	1.0	1.3
20 to 30	25.2	4.2	11.8	5.8	3.0	4.0
30 to 40	15.6	1.6	9.0	4.0	3.2	1.8
40 to 50	8.6	1.8	7.0	3.1	2.2	0.9
50 to 60	9.8	1.4	3.6	0.4	0.6	0.4
60 to 70	5.0	1.0	2.8	2.2	0.8	0.4
70 to 80	6.4	0.6	2.6	2.2	-	-
80 to 90	4.2	0.6	5.2	2.7	-	-
0 to -10	45.0	10.4	26.6	11.6	2.8	1.8
-10 to -20	27.4	2.2	16.2	6.7	2.8	1.8
-20 to -30	20.0	0.6	10.6	4.0	1.8	2.2
-30 to -40	15.4	3.6	4.0	3.1	2.8	2.2
-40 to -50	11.0	0.8	5.8	2.2	1.0	0.9
-50 to -60	10.4	2.2	4.6	3.1	1.0	1.3
-60 to -70	9.6	1.8	2.8	3.1	0.2	0.4
-70 to -80	6.0	2.6	5.0	5.4	-	-
-80 to -90	6.4	1.0	3.4	3.1	-	-

Notes: (1) The polar angle is interpreted to mean sectors of a circle.  
The circle lies on the witness target with its center directly beneath the hole in the target.

(2)  $\sigma$  is the standard deviation per individual observation.

Table II-11. Tabulation of the dispersion data (population of fragments vs solid angle in the polar angle interval  $-10^\circ \leq \theta \leq 10^\circ$ ) obtained from tests with aluminum 24S-0 targets at  $60^\circ$  obliquity.

		Average Number of Spall Fragments Counted in $\Delta\Omega$			
		Target Thickness (in.)			
Solid Angle		(1/16)		(3/32)	
$\Omega$	$\Delta\Omega \times 10^3$	$\bar{N}$	$\sigma$	$\bar{N}$	$\sigma$
0.200	11.1	1.8 (162)	1.8	1.8 (162)	1.8
0.702	27.9	7.6 (272)	3.6	5.8 (208)	3.6
1.319	34.2	17.8 (520)	6.3	14.6 (427)	12.9
1.916	33.2	23.6 (711)	9.4	15.2 (458)	12.9
2.439	29.1	19.6 (673)	10.3	13.8 (474)	12.5
2.880	24.4	13.4 (549)	14.3	5.0 (205)	4.5
3.245	20.3	5.4 (266)	7.1	0.8 (39)	1.3
3.549	16.9	2.2 (130)	3.1	0.0 (0)	0.0
3.639	5.0	0.4 (80)	0.5	0.0 (0)	0.0

- Notes:
- (1) The numbers in parentheses are  $\bar{N}/\Delta\Omega$  and represent the population of fragments per unit solid angle.
  - (2) The solid angle given is the end point of the interval.
  - (3) The  $\Delta\Omega$  intervals are associated with  $20^\circ$  of arc and a  $\Delta r$  width of 1.5 in. except for the last interval where  $\Delta r = 0.5$  in. The distance between target plate and witness target is 5.8 in.
  - (4)  $\sigma$  is the standard deviation per individual observation.

Table III-12. Tabulation of the dispersion data (number of fragments vs polar angle) obtained from tests with aluminum 2024-T3 targets at 60° obliquity.

Polar Angle Interval (deg)	Average Number of Fragments Counted in $\Delta\theta$					
			Target Thickness (in.)			
	(1/16)	(3/32)	(2/16)	$\bar{N}$	$\sigma$	$\bar{N}$
0 to 10	39.0	1.7	27.7	12.0	2.3	-
10 to 20	26.0	5.4	17.0	7.4	1.7	-
20 to 30	13.3	1.7	11.7	8.7	1	-
30 to 40	18.0	5.7	6.3	3.5	1	-
40 to 50	12.3	7.4	5.3	5.2	1	-
50 to 60	8.7	5.2	3.7	2.2	0	-
60 to 70	5.0	3.4	3.7	2.2	-	-
70 to 80	5.0	3.4	1.7	0.5	-	-
80 to 90	4.0	1.7	3.7	1.7	-	-
0 to -10	39.0	16.8	18.7	4.7	1.7	-
-10 to -20	27.7	11.6	13.0	4.7	1.3	-
-20 to -30	19.7	6.9	8.0	2.9	0.3	-
-30 to -40	10.7	4.7	4.7	2.9	1.0	-
-40 to -50	9.0	2.9	2.7	1.7	1.7	-
-50 to -60	5.7	2.9	2.0	1.7	0	-
-60 to -70	6.0	1.7	3.7	2.9	-	-
-70 to -80	5.3	4.0	1.0	0	-	-
-80 to -90	4.3	2.2	1.7	0.5	-	-

Notes: (1) The polar angle intervals given above are sectors of a circle. The circle lies on the witness target with its center directly beneath the hole in the target plate.

(2)  $\sigma$  is the standard deviation per individual observation.

Table II-13. Tabulation of the dispersion data (population of fragments vs solid angle in the polar angle interval  $-10^\circ \leq \theta \leq 10^\circ$ ) from tests with aluminum 2024-T3 targets at  $60^\circ$  obliquity.

Solid Angle		Average Number of Spall Fragments Counted in $\Delta\theta$					
		(1/16)		Target Thickness (in.)		(2/16)	
$\Omega$	$\Delta\Omega \times 10^3$	$\bar{N}$	$\sigma$	$\bar{N}$	$\sigma$	$\bar{N}$	$\sigma$
0.161	8.9	3.0 (337)	2.3	2.0 (224)	1.7	0.3 (34)	0.6
0.578	23.1	4.3 (186)	1.2	5.3 (229)	5.8	2.1 (91)	3.5
1.117	29.9	13.6 (455)	11.5	9.3 (311)	2.3	1.3 (43)	2.3
1.666	30.5	12.1 (397)	4.0	10.3 (337)	5.2	0.0 (0)	0.0
2.168	27.9	18.3 (656)	11.0	6.7 (240)	2.9	0.3 (11)	0.6
2.604	24.3	13.4 (551)	9.2	9.0 (370)	1.2	0.0 (0)	0.0
2.976	20.6	9.4 (456)	3.5	3.0 (146)	1.7	0.0 (0)	0.0
3.290	17.4	3.7 (213)	3.5	0.6 (34)	1.2	0.0 (0)	0.0
3.473	10.1	0.3 (30)	0.6	0.0 (0)	0.0	0.0 (0)	0.0

Notes: (1) Numbers in parentheses are  $\bar{N}/\Delta\Omega$  and represent the population of fragments per unit solid angle.

(2) The  $\Delta\Omega$  intervals are associated with circular rings having  $20^\circ$  arc and a  $\Delta r$  width of 1.5 in. except for the last interval where  $\Delta r = 1.0$  in. Distance between target plate and witness target was 6.5 in.

(3) The solid angle given is the end point of the solid angle interval.

(4)  $\sigma$  is the standard deviation per individual observation.

Table II-14. Tabulation of dispersion data obtained from tests with lead targets at  $60^\circ$  obliquity.

Polar Angle Interval (deg)	Average Number of Fragments Counted in $\Delta\phi$ ( $\Delta\phi = 20^\circ$ )							
	(1/16)		Target Thickness (in.)		(2/16)		(5/32)	
	$\bar{N}$	$\sigma$	$\bar{N}$	$\sigma$	$\bar{N}$	$\sigma$	$\bar{N}$	$\sigma$
60 to 80	5.0	3.6	2.6	3.1	2.6	2.2	0.2	0.4
80 to 100	7.8	6.3	4.4	1.8	2.8	1.8	0.2	0.4
100 to 120	9.0	4.0	5.2	2.2	4.8	1.8	0.2	0.4
120 to 140	9.2	4.5	4.8	5.8	3.2	1.8	2.2	2.2
140 to 160	9.2	6.7	9.4	11.2	4.2	3.6	2.0	1.3
160 to 180	12.4	10.3	6.8	4.5	3.2	1.3	2.0	1.8
180 to 200	14.0	17.9	9.2	7.6	3.2	2.2	2.2	2.2
200 to 220	10.0	7.2	8.2	9.4	2.8	3.1	1.2	2.2
220 to 240	9.2	4.9	9.6	7.6	2.2	2.7	1.2	0.9
240 to 260	7.4	3.6	7.4	4.9	2.4	0.9	0.2	0.4
260 to 280	5.2	0.9	5.8	1.8	2.2	1.8	0.4	0.9
280 to 300	4.6	4.0	2.4	1.3	2.6	1.3	0.2	0.4

Notes: (1) The polar angle intervals given above are sectors of a circle. The circle lies in the plane of the witness target with its center directly beneath the hole in the target plate.

(2)  $\sigma$  is the standard deviation per individual observation.

Table II-15. Tabulation of dispersion data obtained from tests with lead targets at  $60^\circ$  obliquity.  
 (Density of spall fragments vs solid angle in the polar angle interval  $90^\circ \leq \phi \leq 270^\circ$ .)

Average Number of Spall Fragments Counted in  $\Delta\Omega$

Solid Angle $\Omega$	$\Delta\Omega$	(1/16)		Target Thickness (in.)		(2/16)	
		$\bar{N}$	$\sigma$	$\bar{N}$	$\sigma$	$\bar{N}$	$\sigma$
0.024	0.012	4.8 (400)	3.1	6.2 (517)	6.7	1.4 (117)	1.8
0.092	0.034	8.6 (253)	3.6	18.6 (547)	25.5	5.8 (171)	3.6
0.200	0.054	10.4 (193)	4.0	11.2 (207)	8.9	4.2 (78)	3.1
0.343	0.071	15.6 (218)	8.9	9.6 (134)	5.8	5.2 (73)	2.7
0.513	0.085	13.4 (157)	12.1	5.0 (59)	2.2	3.2 (38)	2.7
0.702	0.094	9.4 (100)	10.3	4.0 (43)	3.1	1.6 (17)	1.3
0.903	0.100	7.6 (76)	3.6	3.6 (36)	2.7	1.0 (10)	0.9

Table II-15. (Continued)

Average Number of Spall Fragments Counted in  $\Delta\Omega$ 

Solid Angle $\Omega$	$\Delta\Omega$	(1/16)		Target Thickness (in.)		(2/16)	
		$\bar{N}$	$\sigma$	$\bar{N}$	$\sigma$	$\bar{N}$	$\sigma$
1.111	0.104	5.4 (52)	2.7	2.2 (21)	1.3	1.8 (17)	1.8
1.319	0.104	5.2 (50)	5.8	2.2 (21)	2.7	1.4 (13)	1.8
1.524	0.103	0.8 (8)	0.4	1.4 (14)	1.3	1.2 (12)	0.9
1.724	0.100	1.6 (16)	2.2	0.8 (8)	0.9	0.6 (6)	0.9
1.916	0.096	1.0 (10)	1.3	0.4 (4)	0.4	0.0 (0)	0.0
2.097	0.092	0.4 (4)	0.4	0.0 (0)	0.0	0.4 (4)	0.4
2.275	0.087	0.4 (5)	0.4	0.0 (0)	0.0	0.4 (5)	0.4

Notes: (1) Numbers in parentheses are  $\bar{N}/\Delta\Omega$  and represent the population of fragments per unit solid angle.

(2) The  $\Delta\Omega$  intervals associated with  $180^\circ$  rings having a  $\Delta r$  width of 0.5 in. The distance between the target plate and witness target is 5.8 in.

(3) The solid angle given is the end point of the solid angle interval.

(4)  $\sigma$  is the standard deviation per individual observation.

This particular character of the data may be observed by examining the plots which show the number of fragments versus polar angle ( $\phi$ ) - Figs. II-7a, II-8a, II-9a, II-10a. A typical example for the aluminum groups is the data from 1/32 in. aluminum 2S-0 targets (Fig. II-7a, Table II-8); 33% of the total number of particles were found in the  $20^\circ$  interval ( $-10^\circ < \phi < 10^\circ$ ) and about 90% were found in the forward semi-circle ( $-90^\circ < \phi < 90^\circ$ ). Negative angles are measured counterclockwise from  $\phi = 0^\circ$ . Comparing this with 1/16 in. lead target data, one finds that 33% of the total number of particles were found in the  $40^\circ$  interval ( $160^\circ < \phi < 200^\circ$ ) and 66% in the rear semi-circle ( $90^\circ < \phi < 270^\circ$ ).

The marked differences in angular distributions between data for lead and the aluminum metals suggest differences in basic impact phenomena. The results obtained for lead here can be said to be in qualitative agreement with results from <sup>1/</sup> radiographs of impacted lead targets. The radiographs show material coming off the top surface of

---

1/ G. M. Bryan, "Cratering of Lead by Oblique Impacts of Hypervelocity Steel Pellets", Fundamentals of Shaped Charges, Twenty-second Quarterly Progress Report, Contract No. DA-36-061-ORD-513, April 30, 1961

the plate with a greater amount of material ejected in the "forward" direction. Thus one might conclude that, in order to conserve radial momentum, the material coming off the bottom of a thin plate should have a preference for the backward direction.

- (2) Another set of plots illustrate the radial distribution of particles striking the witness target. These plots give the population density as a function of the solid angle; however, the representation is in a restricted  $\phi$  interval. The restricted  $\phi$  interval is indicated on each plot and is an interval symmetrically spaced about the  $\phi$  value that corresponds to the maximum number of fragments. Again the lead data is different in character from the three aluminum data sets.

The lead plot (Fig. II-10b) shows a maximum density at the origin of circles on the witness target (at  $\Omega = 0$ ). The density decreases continuously in the radial direction corresponding to  $\phi = 180^\circ$ .

Plots for the three aluminum metals show maximum population densities occurring at  $\Omega$  values ranging from 2.0 to about 2.6. In terms of  $\theta/2$ , this would correspond to from  $47^\circ$  to about  $57^\circ$  ( $60^\circ$  corresponds to the path of the projectile). Thus, one finds the maximum density of particles slightly "refracted" from the path of the projectile.

- (3) The total number of particles decreases with the target thickness (see Table II-1). This result is noted for all four target materials; a similar result was obtained at normal incidence.

Another available set of data is the mass recovery data; these are tabulated in Table II-16. The table shows a maximum recovered mass obtained for 3/32 in. thick targets for all four materials. Again, this does not correspond to the thickness for which the maximum number of particles is observed since the maximum number is observed for the thinnest targets tested. Although no "size" data are available, it seems reasonable to conclude that 3/32 in. thick targets yielded larger size particles; this was the conclusion arrived at for tests at normal incidence based upon screen tests.

Thus ends the presentation and discussion of data; a brief summary of both normal incidence and 60° obliquity data seems desirable and is given below:

#### Summary

- (1) For all target materials and target thicknesses impacted at normal incidence, the distribution of fragments is symmetrical about, and maximum along, the extended path of the projectile. The population density decreases with

Table II-16. Tabulation of mass recovery data obtained by water recovery techniques. The thin targets were impacted at  $60^{\circ}$  obliquity by 3.17 km/sec projectiles.

	Recovered Masses (mg) $\pm \sigma_m$			
	(1/32)	Target Thickness (in.) (1/16)	(3/32)	(2/16)
<u>Al. 2S-0 (3 shot data)</u>				
Total Recovered Mass (mg)	$38.5 \pm 1.7$	$55.2 \pm 4.2$	$75.6 \pm 3.9$	$65.4 \pm 5.7$
Recovered Projectile Mass (mg)	$16.6 \pm 0.5$	$14.0 \pm 0.9$	$13.2 \pm 1.4$	$8.9 \pm 0.5$
	(1/16)	Target Thickness (in.) (3/32)	(2/16)	(5/32)
<u>Al. 17S-0 (3 shot data)</u>				
Total Recovered Mass (mg)	$77.1 \pm 2.0$	$96.9 \pm 5.1$	$80.5 \pm 6.6$	-
Recovered Projectile Mass (mg)	$13.3 \pm 1.1$	$11.5 \pm 0.9$	$6.7 \pm 0.7$	-
<u>Al. 2024-T3 (3 shot data)</u>				
Total Recovered Mass (mg)	$78.1 \pm 4.5$	$87.5 \pm 7.8$	$63.6 \pm 7.5$	-
Recovered Projectile Mass (mg)	$13.6 \pm 1.6$	$13.8 \pm 1.3$	$6.9 \pm 2.1$	-
<u>Lead (3 shot data)</u>				
Total Recovered Mass (mg)	$224 \pm 5$	$294 \pm 16$	$293 \pm 35$	$232 \pm 9$
Recovered Projectile Mass (mg)	$2.7 \pm 0.4$	$2.3 \pm 0.4$	$1.0 \pm 0.2$	$0.6 \pm 0.0$

Note:  $\sigma_m$  is an estimate of the standard deviation of the mean.

increasing solid angle (or dispersion angle) in a qualitatively similar manner for all target materials tested, including lead.

- (2) At  $60^{\circ}$  obliquity, the distributions for the three aluminum metals are qualitatively similar but differ appreciably from the distribution for lead. Maximum density for lead is observed along a line extending from the hole and perpendicular to the target plate; the particles are not symmetrically dispersed about this line but show a preference for the "backward" direction.

For the three aluminum metals, the maximum population density occurs along a line that may be described as being slightly "refracted" from the path of the projectile (several degrees to  $10^{\circ}$  "refraction angle").

- (3) For tests at both normal incidence and  $60^{\circ}$  obliquity, the maximum total number of fragments is obtained from the thinnest targets and the total number decreases monotonically with increasing thickness. The maximum recovered mass, however, does not correspond to the maximum number of fragments. Maximum recovered masses are observed for about  $3/16$  in. targets at normal incidence and  $3/32$  in. thick targets at  $60^{\circ}$  obliquity. Screen tests show that the size of the particles account for the lack of correlation between number and mass.

Chapter III - The Perforation of Thin Plates by High Velocity Fragments.  
- R. W. Watson

Introduction

Since its inception, the major effort in the hypervelocity research field has been directed toward the solution of the problem of cratering in semi-infinite targets. However, the impact failure of thin targets, particularly the light structural alloys, has become an increasingly urgent problem. For the past year and a half our research group has been engaged in an extensive experimental program to determine the parameters governing the failure of thin plates under the impact of high velocity fragments. A wide variety of experiments have been completed. The results of several of these investigations have led to the formulation of a simple model that adequately describes certain aspects of the perforation phenomena. This model is discussed in Section A of this Chapter. The qualitative features of these perforation studies, including perforation diameters at normal incidence and 60° obliquity are discussed in Section B.

Section A

Recovery Experiments - The 3.2 km/sec projector discussed in the first chapter was first used in an experimental study to determine the composition of the material ejected from the back surface of thin plates during the perforation process. For this purpose

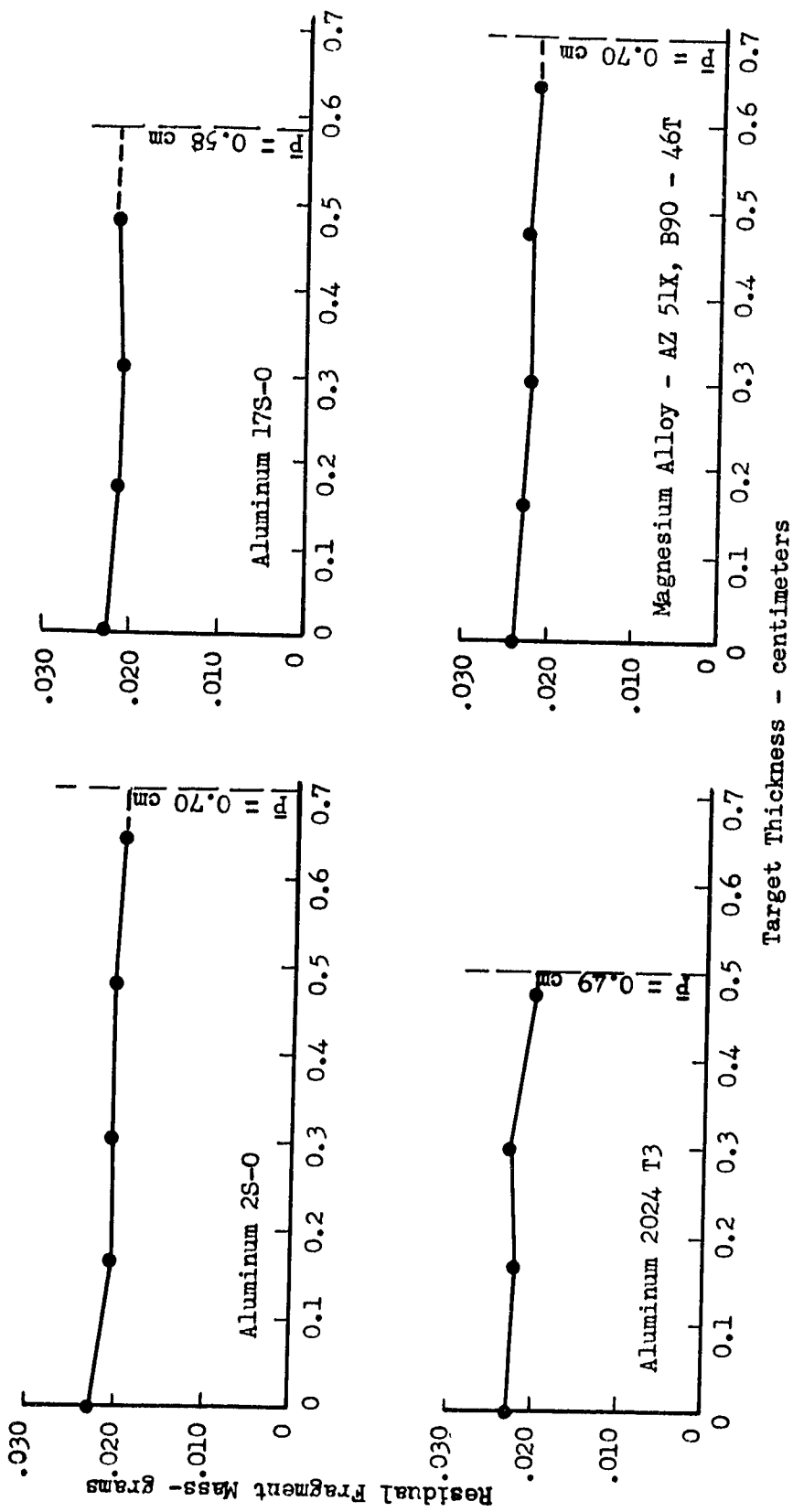


Fig. III-1 Residual fragment mass as a function of target thickness for alloys of aluminum and magnesium.

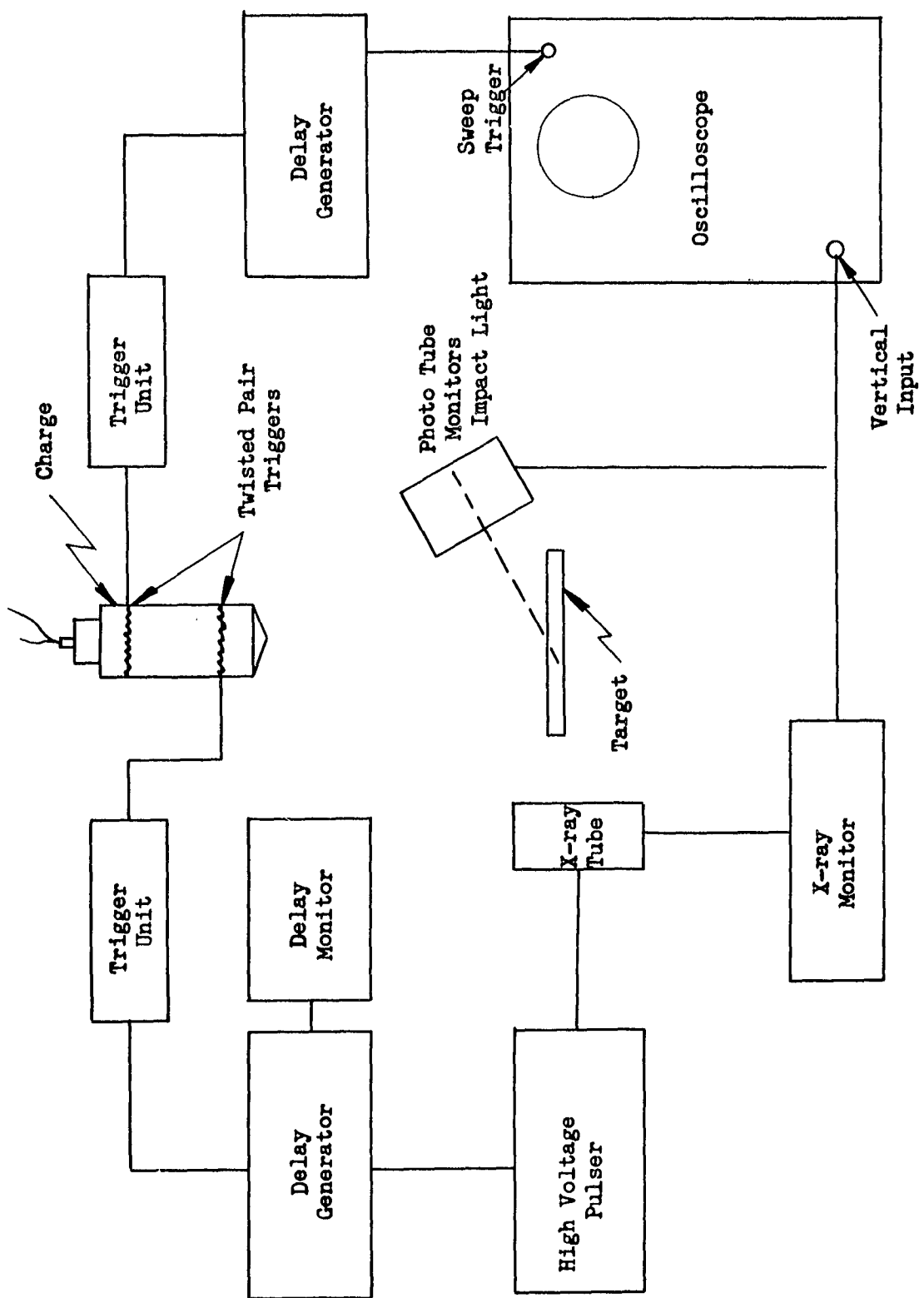


Fig. III-2 Apparatus used in measuring the residual velocity of 3170 m/sec fragments after perforating various thicknesses of lightweight alloys.

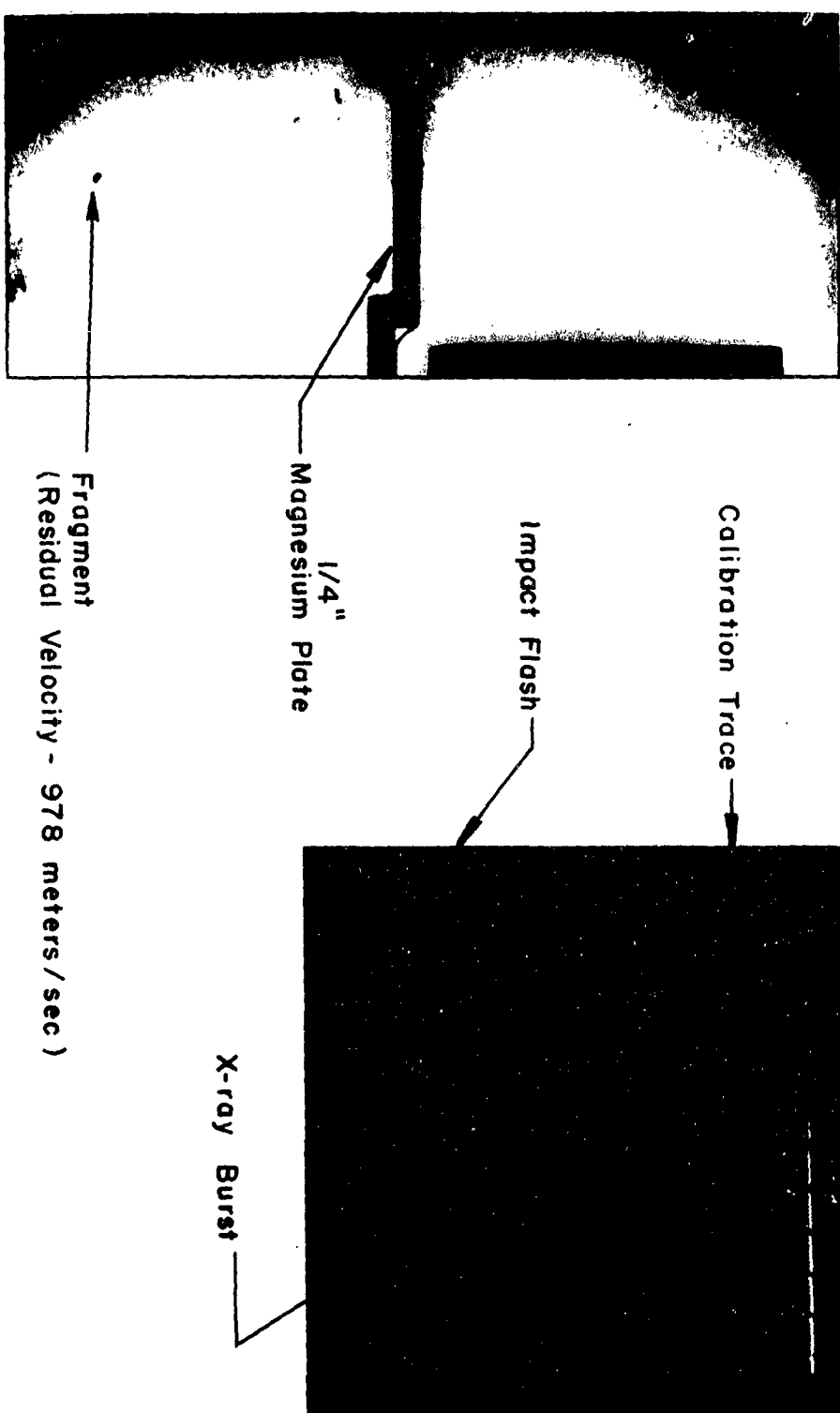


Fig. III-3 Typical radiograph and timing trace used in determining residual fragment velocity.

various thicknesses of aluminum and magnesium alloys were securely attached to a water collection pot and impacted with 3170 m/sec fragments. Care was taken to assure that only the material projected through or spalled from the back surface of the plate was collected. The collected material was then chemically analyzed for steel content. The results of these tests, shown in Fig. III-1, show that within experimental error, all of the impacting fragment mass is projected through the target whenever complete perforation takes place.

Residual Velocity Measurements - Visual inspection of the material collected in the recovery experiments indicated that the fragment perforated the thinner targets (1/16 in.) without undergoing serious deformation. As a result of this observation an extensive flash radiographic program aimed at determining emerging fragment velocity as a function of target thickness was initiated. The experimental arrangement used in this investigation is depicted in Fig. III-2. The two delay networks are adjusted in a manner that allows the fragment to be viewed at a sufficient distance behind the perforated plate to permit accurate distance measurements. Time measurements were accomplished by recording the interval between the luminous flash occurring at impact and the X-ray burst. A typical timing trace is shown in Fig. III-3 along with a radiograph showing a fragment  $110 \mu$  sec after impact. The two vertical strips on either side of the radiograph correspond to aluminum and steel wedges attached to the film cassette; these wedges assist in

identifying the material revealed in the radiographs. The individual results of this series of tests are presented in Table III-1. The spread in the data obtained under a given set of experimental conditions is greater than anticipated on the basis of variation in impacting fragment mass or velocity. This probably can be attributed to either minor variations in fragment orientation at impact or to small differences in the physical properties of the target materials.

Theory and Discussion - At an impact velocity of 3170 m/sec the initial dynamic pressure far exceeds the ordinary yield strength of the target materials used in this study and is, in fact, several times the yield strength of the impacting fragment. However, the impact phenomena described here cannot be entirely ascribed to fluid impact where both the target and impacting body are treated as fluids<sup>1,2/</sup>. The mass recovery experiments and the radiographic investigation support this contention. In addition, the craters produced in semi-infinite targets of the various alloys investigated, unlike the hemispherical craters which are characteristic of pure fluid impact, were deep and narrow and in many instances the fragment

---

1/ H. G. Hopkins and H. Kolsky, "Mechanics of Hypervelocity Impact of Solids", Fourth Symposium on Hypervelocity Impact, April 1960.

2/ A. C. Charters, "High Speed Impact", Scientific American, Vol. 203, No. 4, October 1960.

Table III-1. Residual fragment velocity as a function of target thickness for a 3170 m/sec, 0.023 gm steel fragment perforating various light weight alloys.

Target Thickness (in.)	Residual Velocity (m/sec)			
	2S-0 (Aluminum)	17S-0 (Aluminum)	2024-T3 (Aluminum)	AZ51X,B90-46T (Magnesium)
1/16	2566	2540	2358	2688
	2469	2525	2185	2728
	2566	2568	2545	2725
	2400	2654	2388	2704
	2640	2567	2487	2783
	Average	2528	2569	2725
1/8	1935	1810	1579	2185
	2056	1828	1800	1935
	1558	1570	1794	2150
	1917	1757	1366	2060
	2000	1648	1609	--
	Average	1893	1722	2082
3/16	1220	856	602	1985
	1114	999	795	1541
	1275	1010	723	1672
	981	1433	634	1371
	1070	1102	573	1624
	--	--	-	1660
1/4	Average	1132	1080	1642
	916	--	-	978
	622	--	-	966
	507	--	-	972
	350	--	-	1073
	405	--	-	920
Average	560	--	-	981

remains were found embedded in the crater bottom. If it is assumed that the perforation process is completed before any marked radial expansion of the impacting fragment can take place, then the following simple analysis can be made.

Treating the target as an incompressible fluid, its resistance to penetration can be expressed as

$$p = \frac{1}{2} \rho_t \dot{z}^2 + k \quad (1)$$

where  $\rho_t$  is the target density and  $\dot{z}$  is the instantaneous fragment velocity.

This expression and variations of it have been used in a variety of penetration theories <sup>3,4/</sup>. The term  $\frac{1}{2} \rho_t \dot{z}^2$  is the stagnation pressure and represents the inertial resistance of the target; the factor  $k$  accounts for the strength effects of the target in resisting deformation. The equation of motion of the fragment then becomes

$$m_f \ddot{z} = - (\frac{1}{2} \rho_t A_f \dot{z}^2 + k A_f) \quad (2)$$

3/ R. J. Eichelberger, J. Appl. Phys., Vol. 27, No. 1, January 1956.

4/ Ernst Öpik, "Researches on the Physical Theory of Meteor Phenomena: I. Theory of the Formation of Meteor Craters", Acta et Comm. Univ. Tartuensis, 1936.

where

$m_f$  = fragment mass = .0234 gm

$\rho_t$  = target density = 2.7 gm/cm<sup>3</sup>

$A_f$  = fragment cross section (assumed constant) =  
initial fragment area =  $2.0 \cdot 10^{-2}$  cm<sup>2</sup>

$z$  = instantaneous depth in target measured from  
the surface of the target.

Since the radiographic data give  $\dot{z}$  as a function of  $z$  the substitution  $\ddot{z} = \dot{z} \frac{d\dot{z}}{dz}$  considerably simplifies the treatment of Eq. (2).

On making this substitution the equation of motion is integrated once to give

$$\frac{1}{2} \frac{\rho_t A_f \dot{z}^2}{m_f} + \frac{k A_f}{m_f} = \text{Constant} \cdot e^{-\frac{\rho_t A_f}{m_f} z}. \quad (3)$$

The constant of integration can be evaluated from the condition that when  $z = 0$ ,  $\dot{z} = v_0$ , the initial fragment velocity. Equation (3) then reduces to

$$\dot{z}^2 = v_0^2 e^{-\frac{\rho_t A_f z}{m_f}} + \frac{2k}{\rho_t} \left( e^{-\frac{\rho_t A_f z}{m_f}} - 1 \right). \quad (4)$$

The strength term  $k$  can be evaluated from the final condition that when  $\dot{z} = 0$ ,  $z = P$ , the maximum value of penetration observed in semi-infinite targets of the material under consideration.

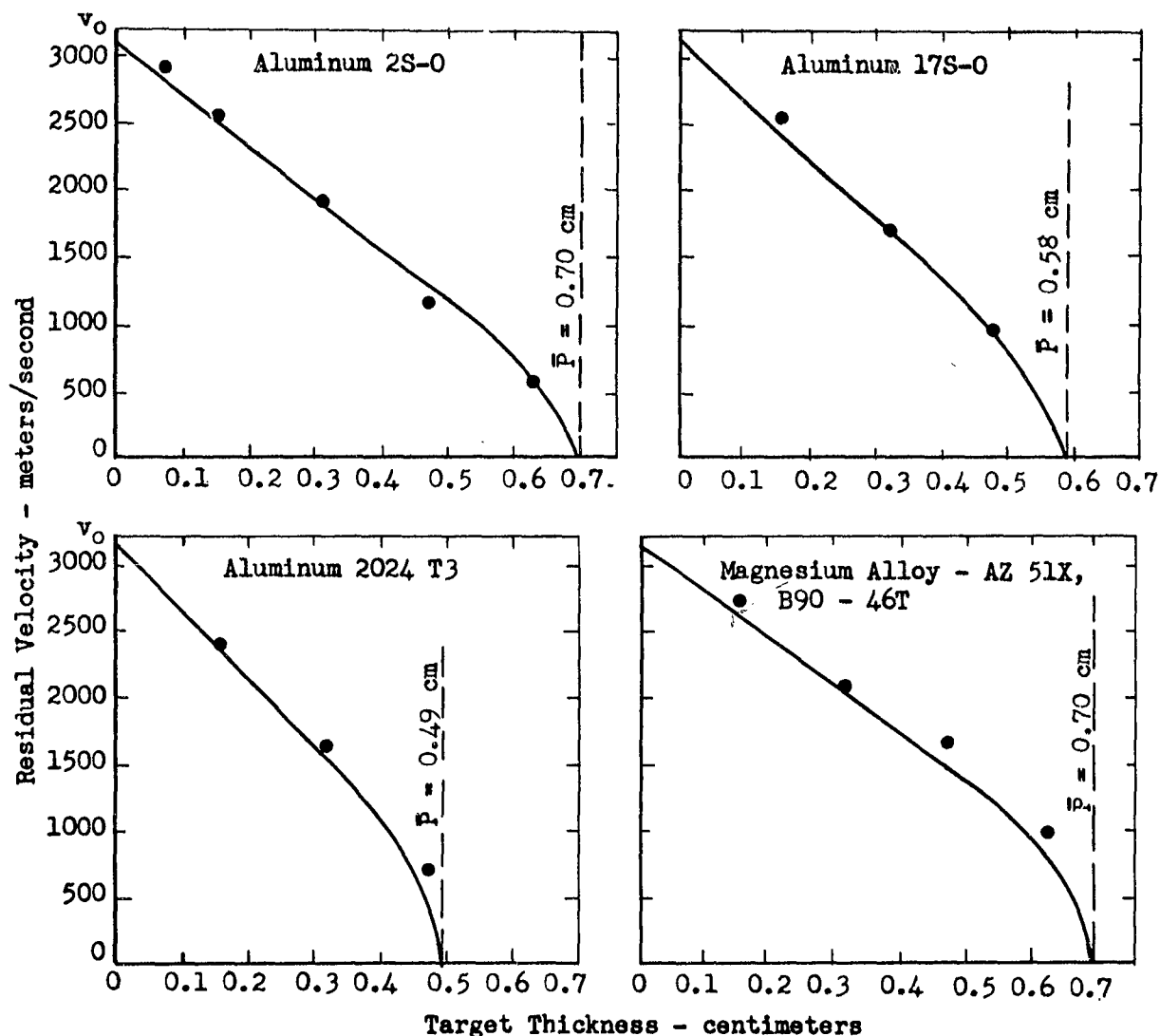


Fig. III-4 Residual fragment velocity as a function of target thickness for a 0.023 gram fragment having an initial velocity of 3170 m/sec. The data points represent the average of five individual measurements. The smooth curves were calculated from theory.

This method was used to calculate residual fragment velocity as a function of target thickness for the various materials tested. The results of the calculations, represented by smooth curves, are shown in Fig. III-4 along with the measured values given in Table III-1. As can be seen, agreement between theory and experiment is quite good. It should be pointed out, however, that the method of evaluating the strength factor, coupled with the form of Eq. (4) assures a reasonably good fit. Nevertheless, the model described here does have some salient features of considerable interest. They can be summarized briefly as follows:

- (i) The values of the strength factor,  $k$ , calculated from Eq. (4) are considerably in excess of the handbook values of static strength for all of the materials tested. The calculated values were 3.37, 4.86, 6.50, and  $4.92 \times 10^{10}$  dynes/cm<sup>2</sup> respectively for the 2S-0, the 17S-0, and the 2024-T3 aluminum alloys, and for the ASTM-AZ51X, B90-46T magnesium alloy. The static yield strength of each of these materials is of the order of  $1 - 2 \times 10^9$  dynes/cm<sup>2</sup>. If the strength factor,  $k$ , has any real physical significance, the high values observed here are probably due to an increase in strength associated with a high strain rate. It is well known that the strength of most material increases markedly with increasing strain rate. Rough estimates indicate that the strain rate involved here is in excess

of  $10^5$  in. per in. per sec. There are no data available in this region for direct comparison purposes but dynamic tests at strain rates of  $10^4$  -  $10^5$  in. per in. per sec show increases in strength of from 2 to 10 times the static strength for a variety of materials.<sup>5,6,7,8/</sup>

- (ii) The appearance of the target density term in Eq. (4) seems to be essentially correct. While the strengths of magnesium and aluminum are comparable, their densities are considerably different, and yet, there is equally good agreement between theory and experiment for both materials.

- 
- 5/ John S. Rinehart and John Pearson, "Behavior of Metals Under Impulsive Loads", The American Society for Metals, 1954.
  - 6/ G. I. Taylor, "Scientific Papers", Vol. 1, Cambridge University Press, 1958.
  - 7/ H. Kolsky, Proceedings of the Physical Society, Vol 62, 1949.
  - 8/ Nelson W. Taylor, J. Appl. Phys., Vol. 18, November 1947.

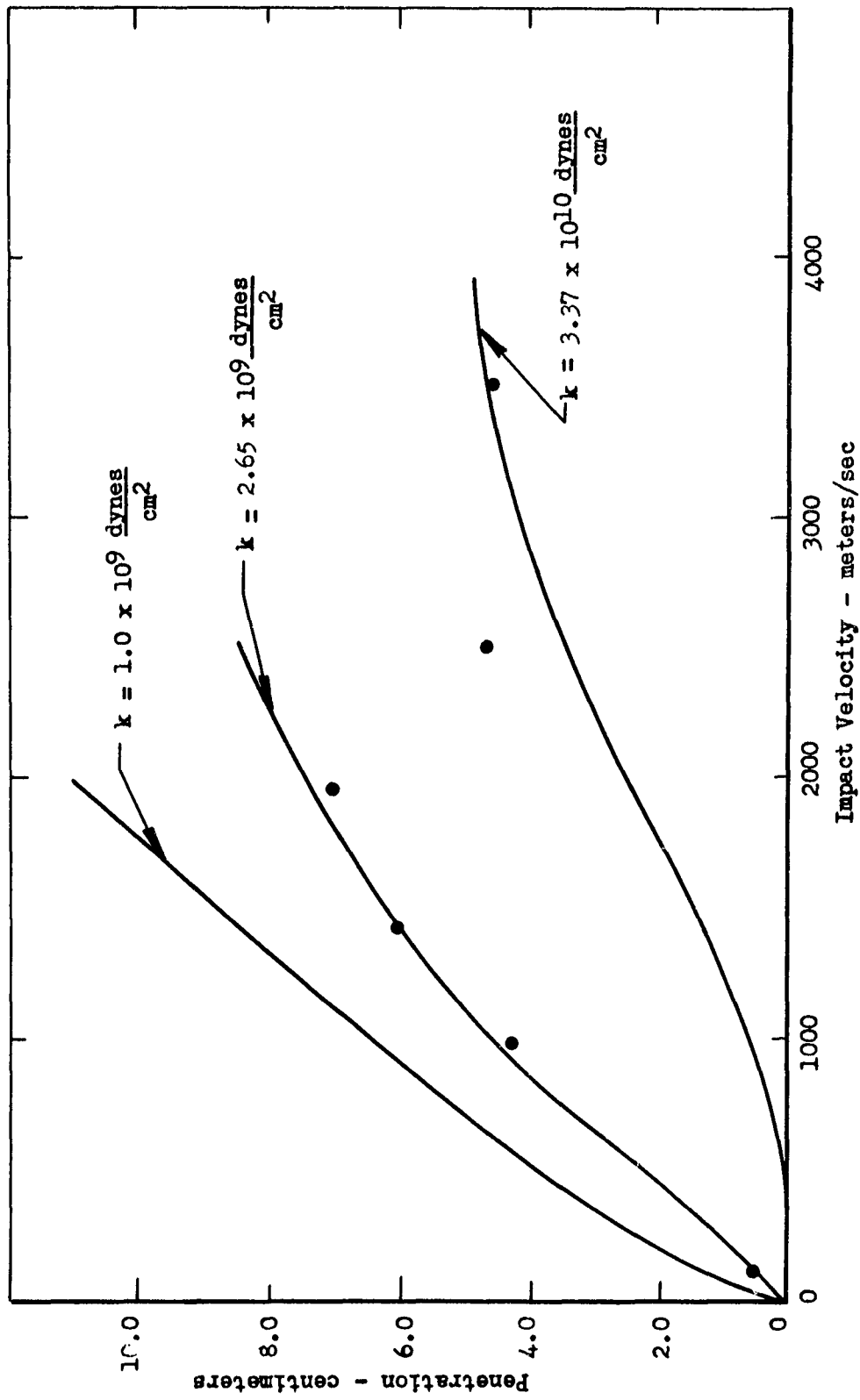


Fig. III-5 Penetration depth as a function of impact velocity for a 1/4 inch diameter tungsten carbide sphere weighing 2.09 grams. The data points represent results obtained at NRL. The smooth curves were calculated from theory using various values of the strength constant.

(iii) Since the fragment used in these studies had a fixed geometry and initial velocity a rigorous test of the general validity of Eq. (4) could not be made. However, this equation can be rearranged to express  $\bar{P}$ , the maximum penetration, in terms of the target and fragment parameters. In this form comparison with the work of other authors can be made. The penetration formula is

$$\bar{P} = \frac{m_f}{\rho_t A_f} \ln \left( 1 + \frac{\rho_t}{2k} v_o^2 \right). \quad (5)$$

A series of experiments described by W. Atkins at the Fourth Symposium on Hypervelocity Impact affords a particularly interesting comparison. In his impact experiments the total depth of penetration in a variety of metals was determined as a function of impact velocity. The projectiles used were 1/4 in. diameter tungsten carbide spheres having a mass of 2.09 grams. Among the target materials investigated was 1100F aluminum, a material having physical properties closely resembling those of 2S-0 aluminum. The results of the penetration tests with this material are reproduced in Fig. III-5 along with a set of theoretical curves computed from Eq. (5) using various values of the strength factor, k, along with the parameter involved in the NRL experiments. The lower curve was computed using the

value of  $k$  determined from our results with 2S-0 aluminum. As can be seen agreement between theory and experiment is very good at the higher impact velocities. The upper curve was computed using the handbook value of the yield strength of aluminum. The central curve was fitted to the data in the low velocity region by using a value of  $k$  computed from the data point at 1500 m/sec. Taken together, the results shown in Fig. III-5 indicate the value of  $k$  is not truly constant for a given material but may represent a strength averaged over the entire penetration velocity spectrum.

- (iv) For historical accuracy, it should be pointed out that Eq. (5) is identical to a penetration formula derived by J. V. Poncelet in 1829<sup>5,9</sup>. His formula, originally tested at impact velocities of the order of 1000 ft/sec, expresses the penetration in a given material as

$$s = \frac{m}{2bA} \ln \left( 1 + \frac{b}{a} v_o^2 \right) \quad (6)$$

where

$m$  = mass of projectile

$A$  = cross-sectional area of the projectile

$v_o$  = initial velocity of the projectile.

2/ H. E. Wessman and W. A. Rose, "Aerial Bombardment Protection", John Wiley and Sons, 1942.

The constants a and b, empirically determined from penetration studies, can be identified with the target strength and density terms appearing in Eq. (5). To date, this formula has been applied with some success to the case of armor penetration.<sup>9/</sup>

### Section B

While the foregoing model does indicate the roles of target strength and density in controlling the depth of penetration in a given impact situation it does not show the interplay of these variables in fixing the diameters of perforations resulting from high speed impacts. This parameter has appeared as a prime variable in recent theoretical studies and since accurate measurements of the perforation diameters were recorded for the majority of the impact tests described in this report, they are presented in this section for further consideration.<sup>10,11/</sup>

- 
- 10/ Pei Chi Chou, "Visco-plastic Flow Theory in Hypervelocity Perforation of Plates", Fifth Symposium on Hypervelocity Impact, November 1961.
  - 11/ G. M. Bryan, "Cratering of Lead by Oblique Impacts of Hypervelocity Steel Pellets", Fundamentals of Shaped Charges, Twenty-second Quarterly Progress Report, Contract No. DA-36-061-ORD-513, April 30, 1961.

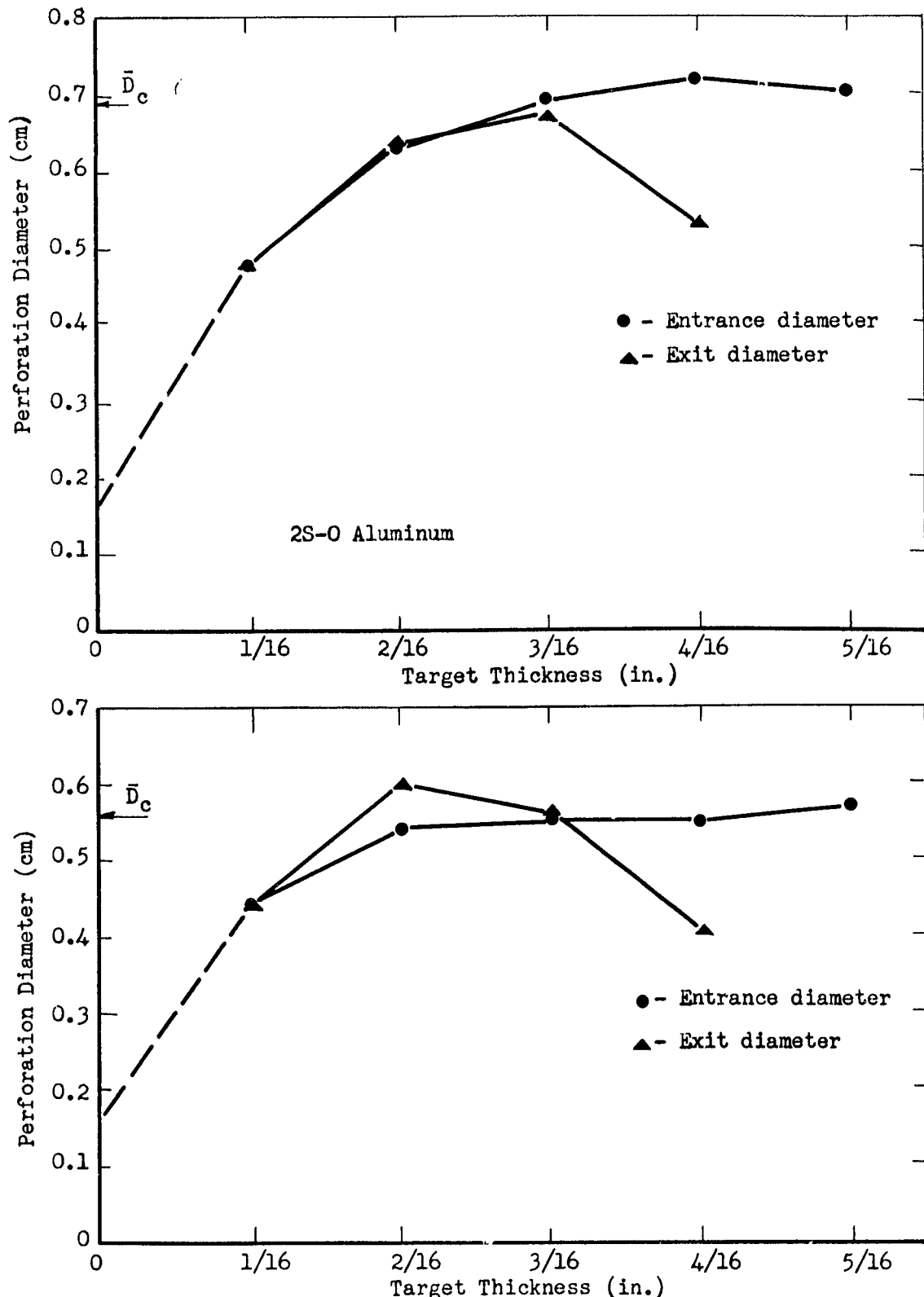


Fig. III-6 Perforation diameter as a function of target thickness for 2S-0 and 17S-0 Aluminum alloys. The tests were carried out at normal incidence.

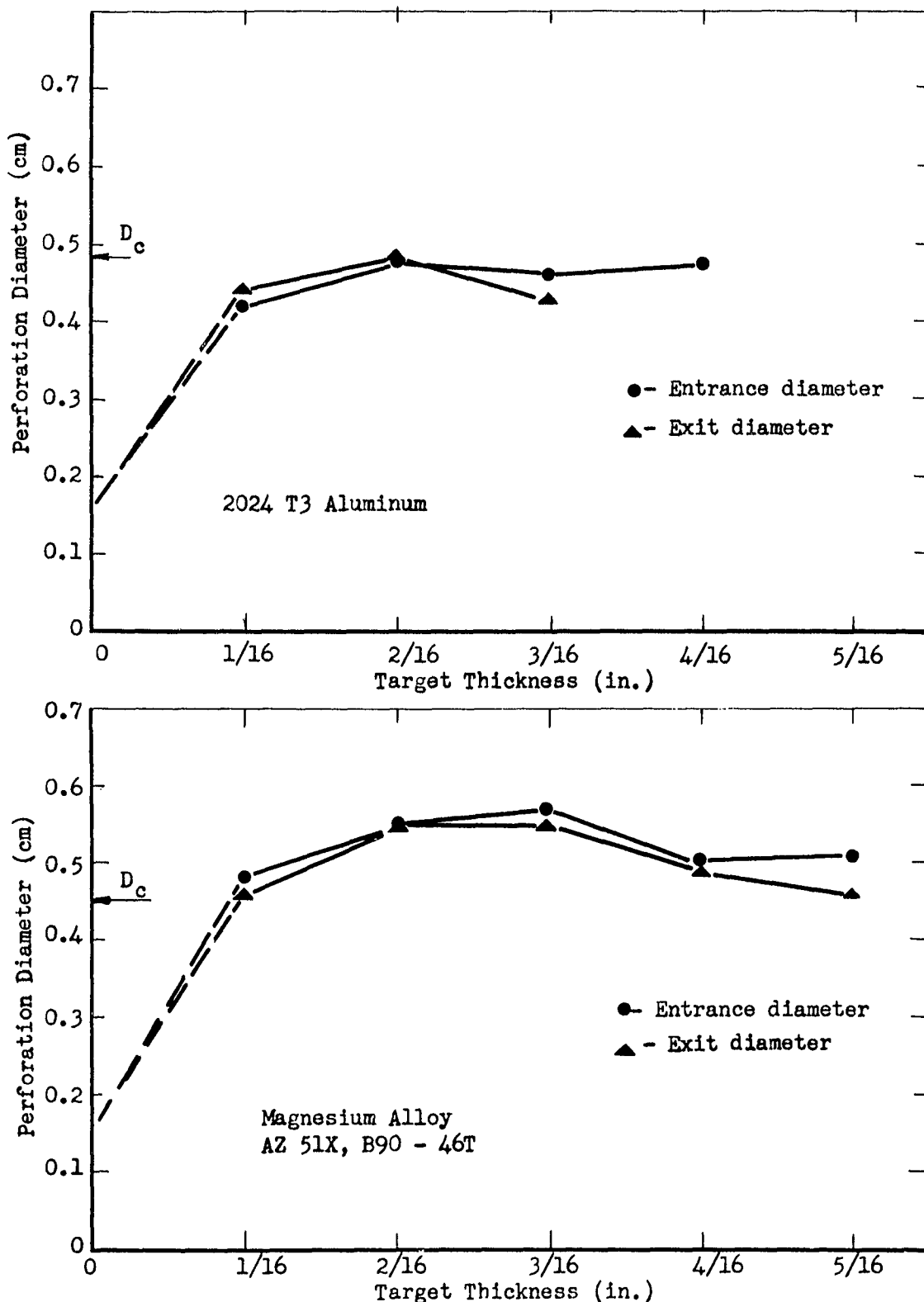


Fig. III-7 Perforation diameter as a function of target thickness for 2024 T3 aluminum and AZ 51X, B 90 - 46T Magnesium. The tests were carried out at normal incidence.

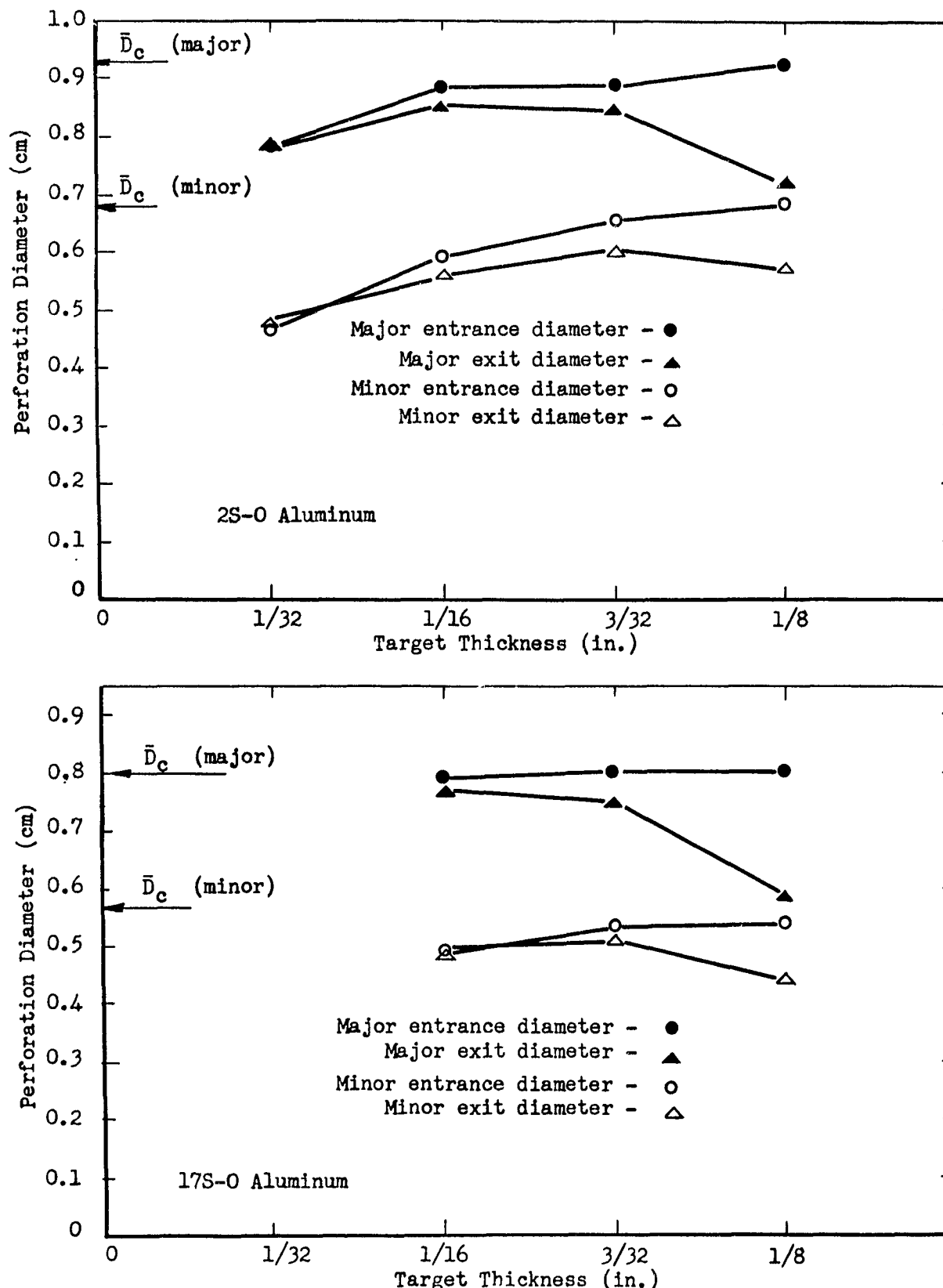


Fig. III-8 Perforation diameter versus target thickness for 2S-O and 17S-O Aluminum. The tests were carried out at  $60^\circ$  obliquity.

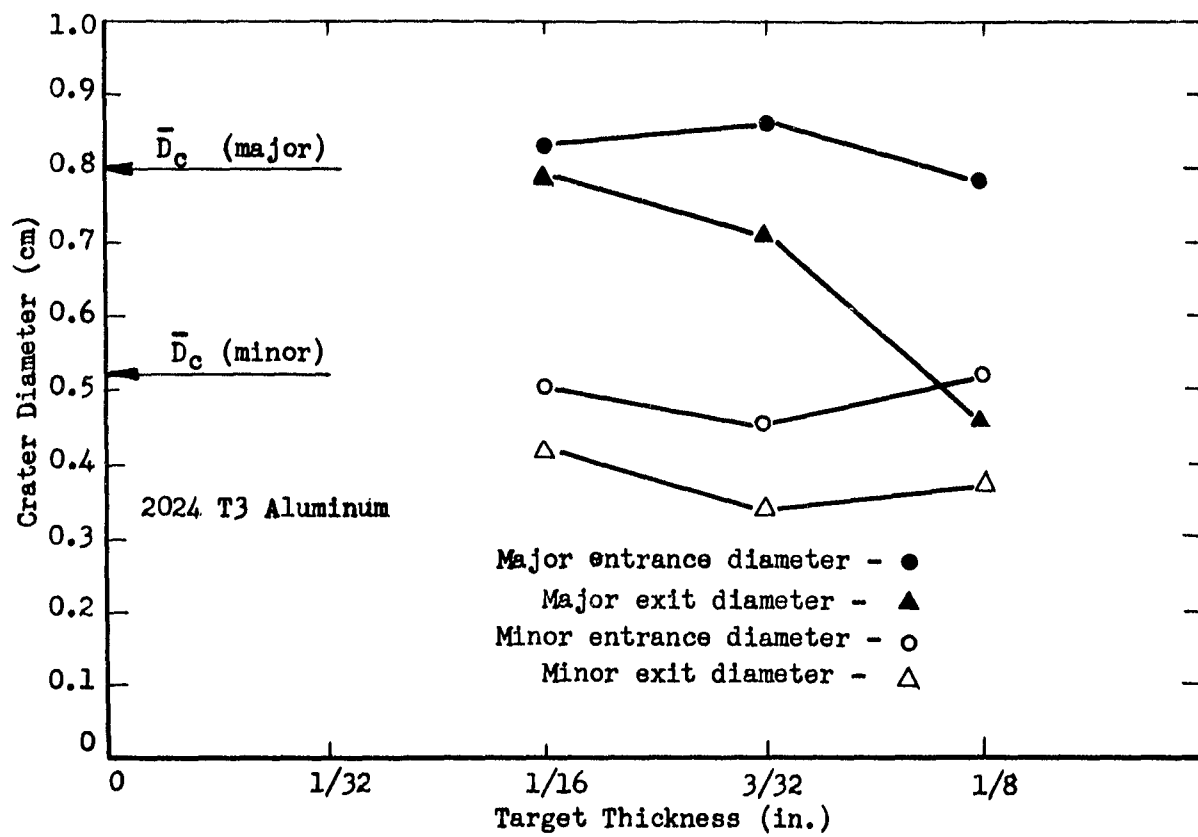


Fig. III-9 Perforation diameter versus target thickness for 2024 T3 Aluminum.  
 The tests were performed at 60° obliquity.

The perforation diameters (crater diameters in the case of semi-infinite targets) were determined by means of a traveling microscope to an accuracy of 0.01 cm. In order to eliminate the ambiguity associated with the crater lip the microscope was first fine-focused on the plane surface of the target immediately outside the deformed area. The focus mechanism was then locked and the traverse mechanism adjusted to bring into focus the two points on the interior crater wall corresponding to the internal diameter. Measurements were made for various thicknesses of three aluminum alloys and one magnesium alloy for perforations resulting from both normal and oblique impact. The diameter measurements are presented in Table III-2 and Table III-3 and plotted as a function of target thickness in Figs. III-6 through III-9. The qualitative features of the results can be summarized as follows:

- (i) For targets having a thickness less than  $\bar{P}/2$ , the perforation diameter is an increasing function of target thickness for all materials tested. This increase can be associated with increased interaction time coupled with viscous effects in the target.
- (ii) For target thicknesses slightly less than  $\bar{P}$  there appears to be a tendency for the perforation diameter to be somewhat greater than the diameter of the craters in semi-infinite targets. This may be associated with differences in the amount of elastic recovery occurring in the two situations.

Table III-2. Entry and exit diameters for various thicknesses of aluminum and magnesium targets impacted with 3170 m/sec, .0234 gm steel fragments at normal incidence. The results represent averages of at least five tests for each set of experimental conditions.

2S-0 (Aluminum)		17S-0 (Aluminum)		2024-T3 (Aluminum)		AZ51X,B90-46T (Magnesium)					
<u>1/16 in. thick targets</u>											
Entry Diameter (cm)				Exit Diameter (cm)							
$\sigma$				$\sigma$							
.48 .04				.44 .01							
Exit Diameter (cm)				Entry Diameter (cm)							
$\sigma$				$\sigma$							
.48 .05				.44 .01							
<u>1/8 in. thick targets</u>											
Entry Diameter (cm)				Exit Diameter (cm)							
$\sigma$				$\sigma$							
.63 .02				.54 .02							
Exit Diameter (cm)				Entry Diameter (cm)							
$\sigma$				$\sigma$							
.64 .04				.60 .02							
<u>3/16 in. thick targets</u>											
Entry Diameter (cm)				Exit Diameter (cm)							
$\sigma$				$\sigma$							
.69 .03				.55 .04							
Exit Diameter (cm)				Entry Diameter (cm)							
$\sigma$				$\sigma$							
.67 .07				.57 .04							

Table III-2. (Continued)

	2S-0 (Aluminum)	17S-0 (Aluminum)	2024-T3 (Aluminum)	AZ51X,B90-46T (Magnesium)
<u>1/4 in. thick targets</u>				
Entry Diameter (cm) $\sigma$	.72 .03	.55 .02	.47 .04	.50 .05
Exit Diameter (cm) $\sigma$	.53 .11	.41 .05	- -	.49 .06
<u>5/16 in. thick targets</u>				
Entry Diameter (cm) $\sigma$	.70 .02	.57 .05	- -	.51 .05
Exit Diameter (cm) $\sigma$	- -	- -	- -	.46 .08
<u>"semi-infinite" targets (<math>t \geq 0.5</math> in.)</u>				
Crater Diameter (cm) $\sigma$	.69 .04	.56 .03	.48 .05	.45 .06
Crater Depth (cm) $\sigma$	.70 .06	.58 .05	.46 .05	.71 .10

Table III-3. Major and minor entry and exit diameters for various thicknesses of aluminum targets impacted with 3170 m/sec, .0234 gm steel fragments at 60° obliquity. The results represent averages of at least five tests for each set of experimental conditions.

	2S-0 (Aluminum)	17S-0 (Aluminum)	2024-T3 (Aluminum)
<u>1/32 in. thick targets</u>			
Entry Diameter (cm)	.78, .47	- -	- -
$\sigma$	.06, .02	- -	- -
Exit Diameter (cm)	.78, .48	- -	- -
$\sigma$	.08, .01	- -	- -
<u>1/16 in. thick targets</u>			
Entry Diameter (cm)	.88, .59	.79, .49	.83, .50
$\sigma$	.08, .03	.05, .01	- -
Exit Diameter (cm)	.85, .56	.77, .49	.79, .42
$\sigma$	.03, .02	.06, .02	- -
<u>3/32 in. thick targets</u>			
Entry Diameter (cm)	.88, .65	.80, .53	.86, .45
$\sigma$	.04, .04	.09, .01	- -
Exit Diameter (cm)	.84, .60	.75, .51	.71, .34
$\sigma$	.05, .02	.05, .03	- -
<u>1/8 in. thick targets</u>			
Entry Diameter (cm)	.92, .68	.80, .54	.78, .52
$\sigma$	.04, .03	.03, .03	- -
Exit Diameter (cm)	.71, .57	.59, .44	.46, .37
$\sigma$	.08, .07	.05, .02	- -
<u>"semi-infinite" targets (<math>t &gt; 0.25</math> in.)</u>			
Crater Diameter (cm)	.93, .68	.80, .57	.80, .52
$\sigma$	.08, .01	.04, .02	.05, .03
Crater Depth (cm)	.40	.33	.22
$\sigma$	.04	.03	.03

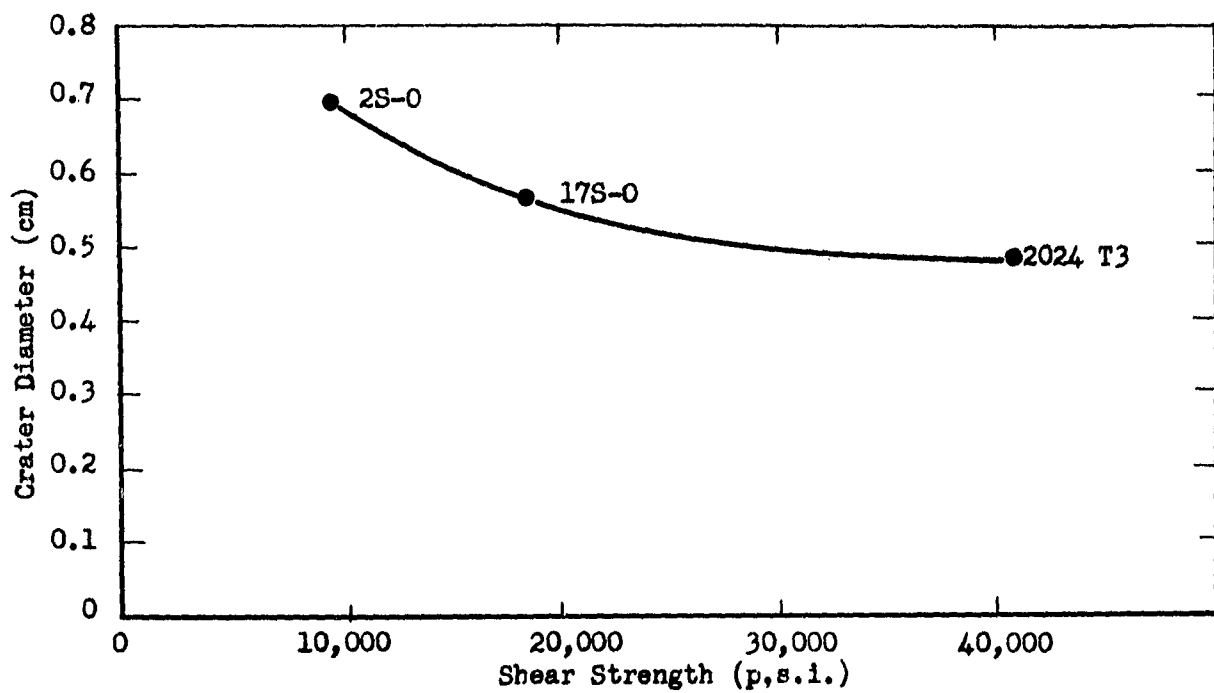


Fig. III-10 Crater diameter versus ordinary shear strength for three aluminum alloys.

(iii) There is a strong correlation between crater diameter and the shear strength of the target material. This observation is illustrated in Fig. III-10 where crater diameters for the four materials are plotted against the handbook value of shear strength for the three aluminum alloys.

Chapter IV - Oblique Impact Cratering in Lead at 3.8 km/sec.  
- G. M. Bryan

Abstract

The volume and shape of craters produced in lead by the impact of steel pellets at 3.8 km/sec have been studied as functions of the angle of incidence for angles up to  $70^{\circ}$  from the normal. It is found that crater volume is linear in the cosine of the angle of incidence and that it is directly proportional to the kinetic energy of the pellet for a given angle of incidence. It is also found that the relation between the depth and the (transverse) diameter is not entirely consistent with the concept of a spherically symmetrical afterflow superimposed on a primary penetration which obeys the density law. The density law itself appears to be satisfied, but the approximation of spherical symmetry in the afterflow is inadequate at this velocity.

Introduction

One of the important variables in the phenomenon of hyperballistic impact is the angle of incidence. Historically, this importance is associated with impact theories of lunar craters, which are all quite circular in spite of the fact that one would expect the impacting meteorites to strike the surface at various angles of incidence. Current interest involves the degree of damage to metal surfaces caused by hypervelocity projectiles as a function of incidence angle.

A study of the dependence on incidence angle of the volume and shape of craters formed on lead surfaces by a 3.2 km/sec steel pellet has been reported in detail<sup>1/</sup>. In that study the effect on volume was compared with the results of a similar experiment at 5 km/sec by Kineke<sup>2/</sup> and it was found that the volume per unit energy was the same in the two cases for all angles of incidence, and was a linear function of the cosine of the angle. It was also shown that the shape of the crater in the 3.2 km/sec case was consistent with the concept of a radial "afterflow" superimposed on a primary penetration which obeys the density law of penetration by fluid jets. (The configuration of the impinging fragment in the 5 km/sec case is not sufficiently well known to permit a similar evaluation to be made.)

The experiment has now been repeated with a velocity in the vicinity of 4 km/sec. The angle of incidence ranged from 0° to 70° from the normal. This experiment was much less extensive than the previous one, its present purpose being mainly a quick comparison of results at about 4 km/sec with those at 3.2 and 5 km/sec.

---

1/ Twenty-second Quarterly Progress Report, April 30, 1961, Contract No. DA-36-061-ORD-513.

2/ J. H. Kineke, Proc. Fourth Symposium on Hypervelocity Impact (Elgin AFB, Florida, 1960) Vol. 1.

Experimental Details

Projector system - The explosive projector system used in this study is described in Chapter I of this report.

Cratering shots - The method used to align the charge axis with the target surface at the desired angle was the same as that used for the previous experiment and has been described in detail<sup>1/</sup>. The pellet was fired through a 3/4 in. hole in a steel baffle plate placed about 30 cm from the charge. The target was approximately 50 cm from the charge, the actual distance varying a few cm with the angle setting. The targets were lead plates approximately 6 in. square and 1 in. thick, with their upper surfaces machined flat. Sufficient shots were fired to obtain two good targets (i.e. no obvious breakup) at each of the following angles (measured from the normal):  $0^\circ$ ,  $35^\circ$ ,  $50^\circ$ ,  $60^\circ$ , and  $70^\circ$ . The uncertainty in the angle is of the order of  $1^\circ$ .

Measurement of the crater characteristics - Both the volume and the shape of the craters are of interest. For normal incidence at these velocities the craters are almost perfectly hemispherical regardless of the shape of the projectile, as long as its aspect ratio is not too different from unity. This characteristic has been widely used as the criterion for distinguishing hypervelocity impact and, therefore, depth and diameter as well as the volume are commonly measured. In the case of oblique impact it is of interest to examine, in addition, the deviation from the hemispherical shape as the angle of incidence is increased. Diameters were therefore

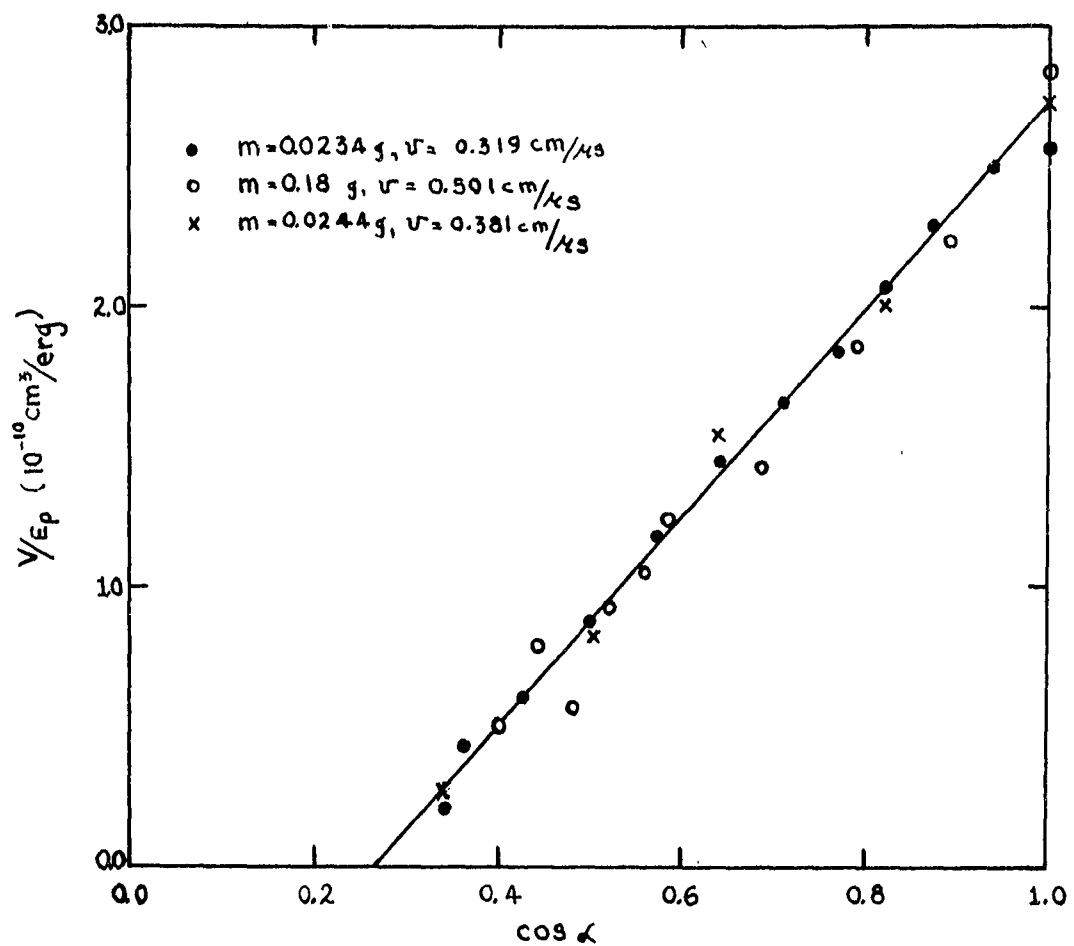


Fig. IV-1 Crater volume per unit projectile energy vs. cosine of the impact angle for three impact situations.

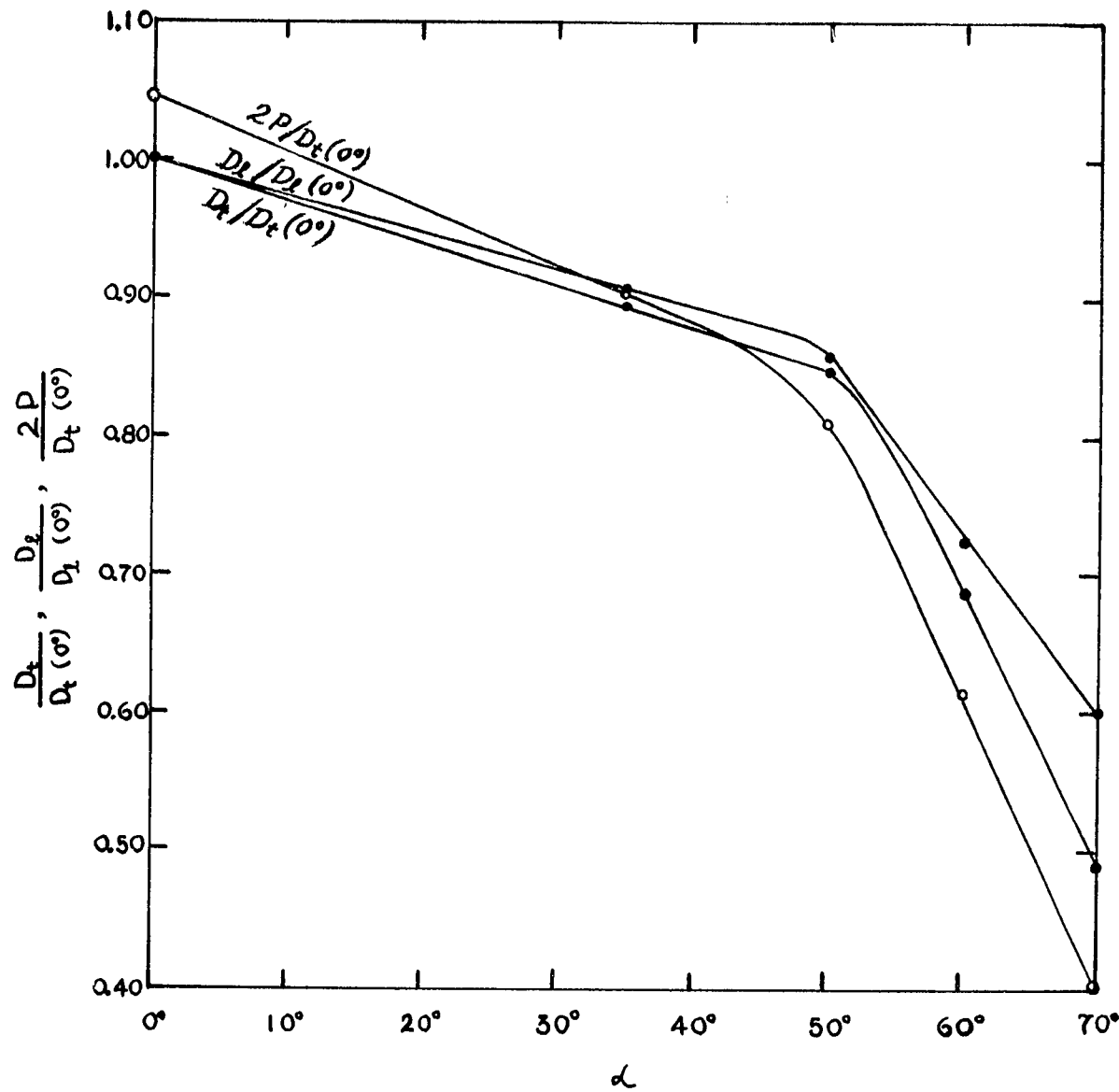


Fig. IX - 2 Crater dimensions vs. impact angle for 3.8 km/sec projectile.  $D_t(0^\circ) = 1.260 \text{ cm}$ ,  $D_p(0^\circ) = 1.231 \text{ cm}$ .

measured in both the transverse and longitudinal directions. These measurements, as well as the depth, were made with a low power traveling microscope. Diameters were measured at the level of the undisturbed surface, and depths were measured down from this surface. Crater volumes were taken to be the volumes below this surface. In order to obtain volume measurements the protruding crater rims were machined off after the diameter and depth measurements had been made. The craters were then filled with modeling clay of known density and the excess clay was carefully shaved off. Volumes were then determined from the weight of the remaining clay.

### Results

The results of the crater measurements are summarized in Table IV-1. Crater volume per unit projectile energy is plotted, together with the earlier results at 3.2 and 5.0 km/sec, in Fig. IV-1. All three sets of data are in excellent agreement and there now seems to be little doubt that over this velocity range the volume is directly proportional to the energy at all angles of incidence and the proportionality constant is a linear function of the cosine of the angle of incidence.

In Fig. IV-2 the linear dimensions, in units of the crater diameter at normal incidence, are shown as functions of the angle of incidence  $\alpha$ . The depth measurements  $P$  have been doubled to permit comparison with the transverse and longitudinal diameters  $D_t$  and  $D_\ell$ . For hemispherical craters we have  $D_t = D_\ell = 2P$ . The results show

Table IV-1. Results of crater measurements. Projectile mass = 0.0244 gm, projectile velocity = 0.381 cm/ $\sqrt{\text{sec.}}$

$\alpha$ (°)	P (cm)	P (avg) (cm)	D <sub>t</sub> (cm)	D <sub>t</sub> (avg) (cm)	D <sub>l</sub> (cm)	D <sub>l</sub> (avg) (cm)	V (cm <sup>3</sup> )	V (avg) (cm <sup>3</sup> )
0	0.655	0.654	1.265	1.260	1.254	1.231	0.496	0.477
	0.652		1.255		1.207		0.459	
35	0.600	0.570	1.142	1.127	1.125	1.114	0.368	0.353
	0.527		1.058		1.045		0.304	
	0.583		1.181		1.171		0.388	
50	0.534	0.510	1.082	1.066	1.040	1.054	0.285	0.271
	0.487		1.050		1.069		0.257	
60	0.408	0.388	0.897	0.866	0.928	0.892	0.160	0.142
	0.369		0.836		0.855		0.123	
70	0.276	0.254	0.628	0.619	0.758	0.739	0.0515	0.0491
	0.233		0.610		0.720		0.0467	

$\alpha$  = angle of incidence, measured from the normal

P = depth

D<sub>t</sub> = transverse diameter

D<sub>l</sub> = longitudinal diameter

V = volume

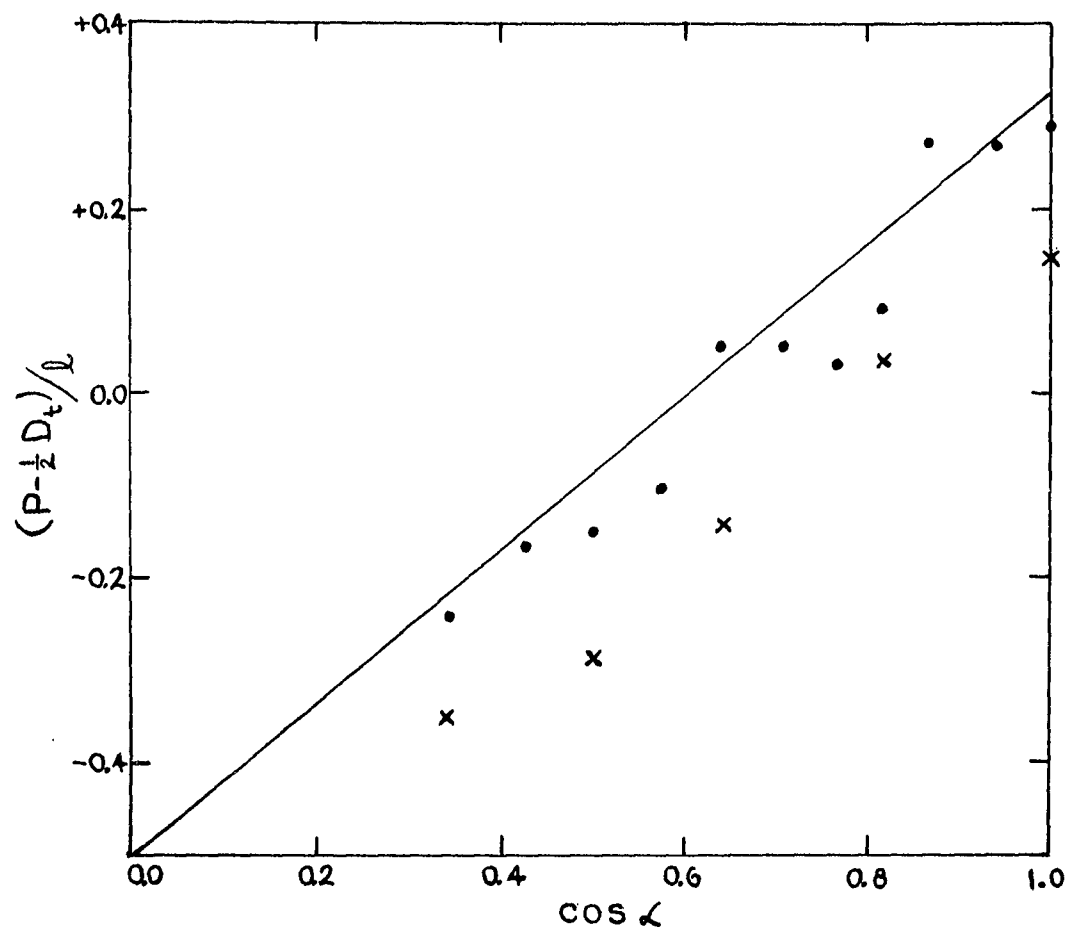


Fig. IV - 3 Vertical elongation of the crater vs. cosine of the impact angle for 3.2 and 3.8 km/sec projectiles.

that at normal incidence the crater is not quite hemispherical,  $2P$  being greater than the diameter. This result is similar to that obtained at  $3.2 \text{ km/sec}$ .<sup>1/</sup> The diameters in Table IV-I exhibit a rather disturbing feature not found in the previous work; for angles out to  $50^\circ$  the longitudinal diameter appears to be consistently less than the transverse diameter by 1-3%. Since this is apparent even at  $0^\circ$  where the distinction between  $D_t$  and  $D_l$  disappears, it would seem to be a systematic error in the aligning system. There is not enough data to rule out coincidence entirely, but the consistency of the effect in the first six individual shots of Table IV-I cannot be ignored. In Fig. IV-2 the diameter curves have been normalized to their respective  $0^\circ$  values to eliminate this discrepancy, and the  $2P$  curve has been arbitrarily normalized to the transverse diameter at  $0^\circ$ .

A relation between crater depth and transverse crater diameter was derived in the earlier report, on the assumption that the cratering process consists of a primary penetration which obeys the density law followed by a radial afterflow of the target material. For a projectile of length  $\ell$  and diameter  $d$  the expression is

$$(P - \frac{1}{2} D_t) / \ell = (\rho_p / \rho_t)^{\frac{1}{2}} \cos \alpha - \frac{1}{2} \frac{d}{\ell} .$$

In Fig. IV-3 this equation is plotted for a steel projectile of unit aspect ratio ( $d = \ell$ ) on a lead target, together with the experimental values for both  $3.2$  and  $3.8 \text{ km/sec}$ . The higher velocity points parallel the theoretical line quite well, thus indicating the correct

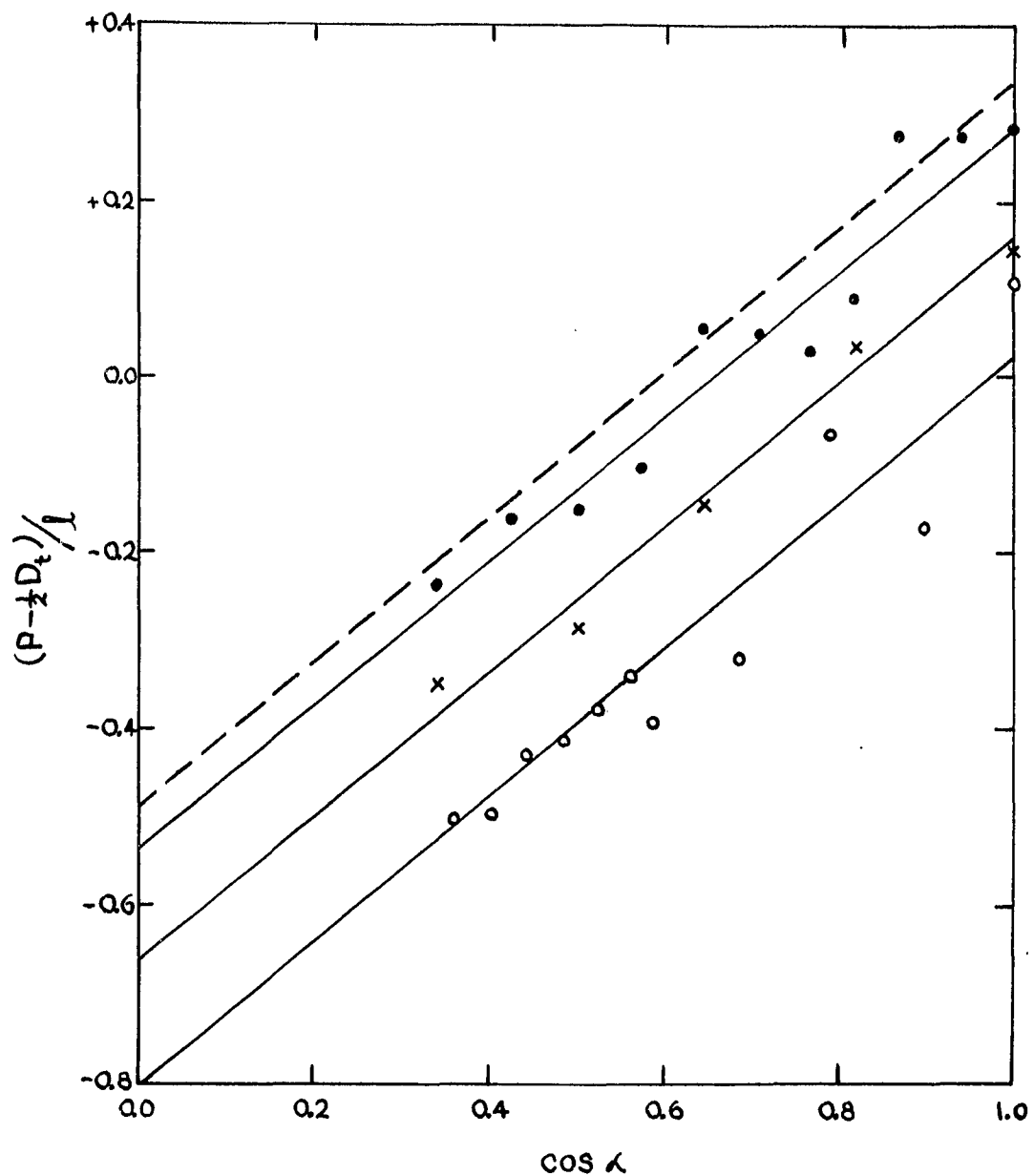


Fig. IV-4 Vertical elongation of the crater vs. cosine of the impact angle for 3.2, 3.8 and 5.0 km/sec projectiles.

density ratio, but fall below it on a line corresponding to a  $d/\ell$  ratio of about 1.3. The nominal value of  $d/\ell$  for this case is 1.04. This discrepancy may be an indication that the  $d/\ell$  ratio actually has changed that much by the time the pellet reaches the target, or it may be due to a partial failure of the simple model at this velocity. Specifically, the assumption of spherical symmetry in the afterflow must be modified in a way which takes into account the free boundary at the surface. In a qualitative way, it is apparent that this would have the effect of making the crater wider and shallower.

In view of this effect an attempt was made to treat Kineke's 2/  
5 km/sec data in the same way. Since in this case the dimensions and orientation of the fragment are not known, the fragment was taken to be a steel sphere of mass equal to the average projectile mass quoted for this charge (0.18g). Then  $\ell = d = .353$  cm. In Fig. IV-4 all three sets of data are plotted together. Each set is roughly parallel to the theoretical line but falls below it; the intercept increasing with increasing velocity. (The straight lines have been drawn through the data parallel to the density-law line and do not represent least squares calculations.)

AD Accession No. *Unclassified*

Carnegie Institute of Technology, Pittsburgh, Penna.  
FUNDAMENTALS OF SHAPED CHARGES -  
Pearson M. Pugh - Supervisor

Twenty-Fourth Quarterly Progress Report, 31 Oct. 61.  
(Contract DA-36-061-ORD-513) DA Proj 5803-OI-009  
ORD Proj TB3-013b, Unclassified Report.

Various aspects of the perforation of thin targets by high speed fragments have been investigated. A fragment projector yielding compact steel fragments having a velocity of 3.17 km/sec and a mass of .0231 gm was generally used for experimental studies. The design features of this projector along with methods of attaining higher velocities are discussed in Chapter I. The spatial distribution and total mass of the ejecta produced in the perforation of thin targets for both normal and oblique impact are discussed in Chapter II. A simple physical model useful in predicting the velocity of a fragment after having perforated a thin target is discussed in Chapter III along with the dimensional features of the perforations. In Chapter IV the volume and shape of craters produced in lead at 60° obliquity by fragments having a velocity of 4 km/sec are compared with the characteristics of craters produced at impact velocities of 3 km/sec and 5 km/sec.

*Unclassified*

AD Accession No. *Unclassified*

Carnegie Institute of Technology, Pittsburgh, Penna.  
Thin Target Perforation Studies

Twenty-Fourth Quarterly Progress Report, 31 Oct. 61.  
(Contract DA-36-061-ORD-513) DA Proj 5803-OI-009  
ORD Proj TB3-013b, Unclassified Report.

Various aspects of the perforation of thin targets by high speed fragments have been investigated. A fragment projector yielding compact steel fragments having a velocity of 3.17 km/sec and a mass of .0231 gm was generally used for experimental studies. The design features of this projector along with methods of attaining higher velocities are discussed in Chapter I. The spatial distribution and total mass of the ejecta produced in the perforation of thin targets for both normal and oblique impact are discussed in Chapter II. A simple physical model useful in predicting the velocity of a fragment after having perforated a thin target is discussed in Chapter III along with the dimensional features of the perforations. In Chapter IV the volume and shape of craters produced in lead at 60° obliquity by fragments having a velocity of 4 km/sec are compared with the characteristics of craters produced at impact velocities of 3 km/sec and 5 km/sec.

*Unclassified*

AD Accession No. *Unclassified*

Carnegie Institute of Technology, Pittsburgh, Penna.  
FUNDAMENTALS OF SHAPED CHARGES -  
Pearson M. Pugh - Supervisor

Twenty-Fourth Quarterly Progress Report, 31 Oct. 61.  
(Contract DA-36-061-ORD-513) DA Proj 5803-OI-009  
ORD Proj TB3-013b, Unclassified Report.

Various aspects of the perforation of thin targets by high speed fragments have been investigated. A fragment projector yielding compact steel fragments having a velocity of 3.17 km/sec and a mass of .0231 gm was generally used for experimental studies. The design features of this projector along with methods of attaining higher velocities are discussed in Chapter I. The spatial distribution and total mass of the ejecta produced in the perforation of thin targets for both normal and oblique impact are discussed in Chapter II. A simple physical model useful in predicting the velocity of a fragment after having perforated a thin target is discussed in Chapter III along with the dimensional features of the perforations. In Chapter IV the volume and shape of craters produced in lead at 60° obliquity by fragments having a velocity of 4 km/sec are compared with the characteristics of craters produced at impact velocities of 3 km/sec and 5 km/sec.

*Unclassified*

AD Accession No. *Unclassified*

Carnegie Institute of Technology, Pittsburgh, Penna.  
Thin Target Perforation Studies

Twenty-Fourth Quarterly Progress Report, 31 Oct. 61.  
(Contract DA-36-061-ORD-513) DA Proj 5803-OI-009  
ORD Proj TB3-013b, Unclassified Report.

Various aspects of the perforation of thin targets by high speed fragments have been investigated. A fragment projector yielding compact steel fragments having a velocity of 3.17 km/sec and a mass of .0231 gm was generally used for experimental studies. The design features of this projector along with methods of attaining higher velocities are discussed in Chapter I. The spatial distribution and total mass of the ejecta produced in the perforation of thin targets for both normal and oblique impact are discussed in Chapter II. A simple physical model useful in predicting the velocity of a fragment after having perforated a thin target is discussed in Chapter III along with the dimensional features of the perforations. In Chapter IV the volume and shape of craters produced in lead at 60° obliquity by fragments having a velocity of 4 km/sec are compared with the characteristics of craters produced at impact velocities of 3 km/sec and 5 km/sec.

*Unclassified*

*Unclassified*

AD \_\_\_\_\_ Accession No. \_\_\_\_\_ *Unclassified*  
**Carnegie Institute of Technology, Pittsburgh, Penna.**  
**FUNDAMENTALS OF SHAPED CHARGES -**  
**Emerson N. Pugh - Supervisor**

Twenty-Fourth Quarterly Progress Report, 31 Oct. 61.  
 (Contract DA-36-061-ORD-513) DA Proj 5B03-OI-009  
 ORD Proj TB3-OI3L, Unclassified Report

Various aspects of the perforation of thin targets by high speed fragments have been investigated. A fragment projector yielding compact steel fragments having a velocity of 3.17 km/sec and a mass of .0231 gm was generally used for experimental studies. The design features of this projector along with methods of attaining higher velocities are discussed in Chapter I. The spatial distribution and total mass of the ejecta produced in the perforation of thin targets for both normal and oblique impact are discussed in Chapter II. A simple physical model useful in predicting the velocity of a fragment after having perforated a thin target is discussed in Chapter III along with the dimensional features of the perforations. In Chapter IV the volume and shape of craters produced in lead at 60° obliquity by fragments having a velocity of 4 km/sec are compared with the characteristics of craters produced at impact velocities of 3 km/sec and 5 km/sec.

*Unclassified*

AD \_\_\_\_\_ Accession No. \_\_\_\_\_ *Unclassified*  
**Carnegie Institute of Technology, Pittsburgh, Penna.**  
**FUNDAMENTALS OF SHAPED CHARGES -**  
**Emerson N. Pugh - Supervisor**

Twenty-Fourth Quarterly Progress Report, 31 Oct. 61.  
 (Contract DA-36-061-ORD-513) DA Proj 5B03-OI-009  
 ORD Proj TB3-OI3L, Unclassified Report

Various aspects of the perforation of thin targets by high speed fragments have been investigated. A fragment projector yielding compact steel fragments having a velocity of 3.17 km/sec and a mass of .0231 gm was generally used for experimental studies. The design features of this projector along with methods of attaining higher velocities are discussed in Chapter I. The spatial distribution and total mass of the ejecta produced in the perforation of thin targets for both normal and oblique impact are discussed in Chapter II. A simple physical model useful in predicting the velocity of a fragment after having perforated a thin target is discussed in Chapter III along with the dimensional features of the perforations. In Chapter IV the volume and shape of craters produced in lead at 60° obliquity by fragments having a velocity of 4 km/sec are compared with the characteristics of craters produced at impact velocities of 3 km/sec and 5 km/sec.

*Unclassified*

*Unclassified*

AD \_\_\_\_\_ Accession No. \_\_\_\_\_ *Unclassified*  
**Carnegie Institute of Technology, Pittsburgh, Penna.**  
**Thin Target Perforation Studies**

Twenty-Fourth Quarterly Progress Report, 31 Oct. 61.  
 (Contract DA-36-061-ORD-513) DA Proj 5B03-OI-009  
 ORD Proj TB3-OI3L, Unclassified Report

Various aspects of the perforation of thin targets by high speed fragments have been investigated. A fragment projector yielding compact steel fragments having a velocity of 3.17 km/sec and a mass of .0231 gm was generally used for experimental studies. The design features of this projector along with methods of attaining higher velocities are discussed in Chapter I. The spatial distribution and total mass of the ejecta produced in the perforation of thin targets for both normal and oblique impact are discussed in Chapter II. A simple physical model useful in predicting the velocity of a fragment after having perforated a thin target is discussed in Chapter III along with the dimensional features of the perforations. In Chapter IV the volume and shape of craters produced in lead at 60° obliquity by fragments having a velocity of 4 km/sec are compared with the characteristics of craters produced at impact velocities of 3 km/sec and 5 km/sec.

*Unclassified*

AD \_\_\_\_\_ Accession No. \_\_\_\_\_ *Unclassified*  
**Carnegie Institute of Technology, Pittsburgh, Penna.**  
**Thin Target Perforation Studies**

Twenty-Fourth Quarterly Progress Report, 31 Oct. 61.  
 (Contract DA-36-061-ORD-513) DA Proj 5B03-OI-009  
 ORD Proj TB3-OI3L, Unclassified Report

Various aspects of the perforation of thin targets by high speed fragments have been investigated. A fragment projector yielding compact steel fragments having a velocity of 3.17 km/sec and a mass of .0231 gm was generally used for experimental studies. The design features of this projector along with methods of attaining higher velocities are discussed in Chapter I. The spatial distribution and total mass of the ejecta produced in the perforation of thin targets for both normal and oblique impact are discussed in Chapter II. A simple physical model useful in predicting the velocity of a fragment after having perforated a thin target is discussed in Chapter III along with the dimensional features of the perforations. In Chapter IV the volume and shape of craters produced in lead at 60° obliquity by fragments having a velocity of 4 km/sec are compared with the characteristics of craters produced at impact velocities of 3 km/sec and 5 km/sec.

*Unclassified*

## DISTRIBUTION

	<u>Addressee</u>	<u>Number of Copies</u>	<u>Numbers</u>
1.	Commanding General Aberdeen Proving Ground Maryland ATTN: Ballistic Research Laboratories	16	1-16 Incl.
2.	Commanding General Aberdeen Proving Ground Maryland ATTN: Development and Proof Services, Technical Information Branch	2	17-18
3.	U.S. Army Ordnance District, Phila. Pittsburgh Regional Office 200 Fourth Avenue Pittsburgh 22, Pennsylvania	1	19
4.	Chief of Ordnance Department of the Army Washington 25, D. C. ATTN: ORDTB-Ballistic Section	1	20
5.	Chief of Ordnance Department of the Army Washington 25, D. C. ATTN: ORDTU	1	21
6.	British Joint Services Mission 1800 K Street, N. W. Washington 6, D. C. ATTN: Mr. John Izzard Reports Officer	4	22-25 Incl.
7.	Canadian Army Staff 2450 Massachusetts Ave., N. W. Washington 8, D. C.	2	26-27
8.	Commanding Officer Diamond Ordnance Fuze Laboratories Washington 25, D. C. ATTN: ORDTL 06.33, Tech. Rev. Sec.	1	28

DISTRIBUTION

	<u>Addressee</u>	<u>Number of Copies</u>	<u>Numbers</u>
9.	Commanding Officer Diamond Ordnance Fuze Labs. Connecticut Ave., at Van Ness St., N. W. Washington 25, D. C. ATTN: Ordnance Development Labs.	1	29
10.	Commanding Officer Detroit Arsenal Center Line, Michigan	1	30
11.	Commanding General Frankford Arsenal Bridesburg Station Philadelphia 37, Pennsylvania	1	31
12.	Commanding Officer U.S. Army Ordnance District, Phila. 128 North Broad Street Philadelphia, Pennsylvania ATTN: OD, RandD Branch	1	32
13.	Commanding General Ordnance Ammunition Command U.S. Army Joliet, Illinois ATTN: ORDLY-AR-V ORDLY-AR-AR	1	33
14.	Commanding Officer Picatinny Arsenal Dover, New Jersey ATTN: Samuel Feltman Ammunition Laboratories	3	34-36 Incl.
15.	Commanding General Redstone Arsenal U.S. Army Redstone Arsenal, Alabama ATTN: Technical Library	1	37

## DISTRIBUTION

	<u>Addressee</u>	<u>Number of Copies</u>	<u>Numbers</u>
16.	Commanding Officer Watertown Arsenal Watertown 72, Massachusetts ATTN: W. A. Laboratory	1	38
17.	Reference Department Technical Information Division Library of Congress Washington 25, D. C. ATTN: Dr. Clement R. Brown, Head Bibliography Section	1	39
18.	Armed Services Information Agency Arlington Hall Station Arlington 12, Virginia	10	40-49 Incl.
19.	Chief of Engineers Department of the Army Washington 25, D. C. ATTN: ENGNF Mine Warfare Branch	1	50
20.	Commanding Officer Engineer Research and Development Laboratory Fort Belvoir, Virginia ATTN: Technical Intelligence Branch	1	51
21.	Chief, Bureau of Naval Weapons Department of the Navy Washington 25, D. C. ATTN: RRRE	1	52
22.	Commander Naval Ordnance Laboratory White Oak Silver Spring 19, Maryland	2	53-54
23.	Commander U.S. Naval Ordnance Test Station China Lake, California ATTN: Technical Library	2	55-56

## DISTRIBUTION

	<u>Addressee</u>	<u>Number of Copies</u>	<u>Numbers</u>
24.	Commander Naval Proving Ground Dahlgren, Virginia	1	57
25.	Director Naval Research Laboratory Washington 25, D. C. ATTN: Tech. Information Division	1	58
26.	Commanding Officer Chemical Warfare Laboratories Army Chemical Center Maryland	1	59
27.	Bureau of Mines 4800 Forbes Street Pittsburgh 13, Pennsylvania ATTN: Chief, Explosive and Physical Sciences Div.	1	60
28.	Director Applied Physics Laboratory 8621 Georgia Avenue Silver Spring, Maryland ATTN: Mr. H. S. Morton THRU: Naval Inspector of Ordnance Applied Physics Laboratory 8621 Georgia Avenue Silver Spring, Maryland	1	61
29.	Firestone Tire and Rubber Co. Akron 17, Ohio ATTN: Librarian ATTN: Mr. C. M. Cox, Defense Res. Div. THRU: Commanding Officer Cleveland Ordnance District 1367 East Sixth Street Cleveland 14, Ohio	1	62

DISTRIBUTION

	<u>Addressee</u>	<u>Number of Copies</u>	<u>Numbers</u>
30.	Director, Project RAND Department of the Air Force 1700 Main Street Santa Monica, California ATTN: Mr. M. R. Anderson Librarian Of Interest to: Dr. J. H. Huth Dr. R. D. Holbrook	1	63
31.	Director National Aeronautics and Space Administration 1520 H Street, N. W. Washington 25, D. C. ATTN: Mr. Bertram A. Mulcahy Chief, Division of Research Information	5	64-68 Incl.
32.	University of California Radiation Laboratory P. O. Box 808 Livermore, California THRU: Commanding Officer San Francisco Ordnance District 1515 Clay Street, P.O. Box 1829 Oakland 12, California	1	69
33.	Los Alamos Scientific Laboratory P. O. Box 1663 Los Alamos, New Mexico ATTN: Report Librarian	1	70
34.	Commanding Officer Office of Ordnance Research Box CM Duke Station Durham, North Carolina	1	71
35.	U.S. Atomic Energy Commission Washington 25, D. C. ATTN: Technical Reports Library	1	72

DISTRIBUTION

<u>Addressee</u>	<u>Number of Copies</u>	<u>Numbers</u>
36. Commander Air Research and Development Command Andrews Air Force Base Washington 25, D. C. ATTN: RDTWMB	1	73
37. Commander Air Proving Ground Center Eglin Air Force Base Florida ATTN: PGTRI PGW PGR PGE	4	74-77 Incl.
38. Commander Wright Air Development Center Wright-Patterson Air Force Base Ohio ATTN: WCLGR-4	1	78